Separation and Recovery of Carbon Dioxide and Underground Storage of Exhaust Gas from Coal Combustion System

(石炭燃焼排ガスに含まれる二酸化炭素の分離・回収および地中貯留に関する研究)

Kosuke Tanaka

Contents

Chapter 1

General Introduction

The 2015 United Nations climate change conference, the 21st yearly session of the conference of the parties (COP 21), was held in Paris, France in December 2015. During the conference, the participants agreed upon the "Paris agreement," which specified target CO_2 reductions as a global warming countermeasure. Today, inhibition of global warming is a priority of developed countries and a significant issue all over the world. Several targets for CO_2 reduction have been agreed upon by developed countries since the Kyoto Protocol in 1997; however, currently, the amount of CO_2 emissions continues to increase. The total amount of CO_2 emitted from all countries increased from 21 billion tons in 1990 to 35.5 billion tons in 2014 due to the increasing demand for energy in developing countries such as China and India. The International Energy Agency (IEA) expects that emissions will further increase to 42.5 billion tons in 2035 [1].

The amount of CO_2 emitted by a country is closely related to that country's pattern of energy use. Coal emits more CO_2 per unit of electric power consumption than other fossil fuels; coal accounts for 33% of global energy production, whereas it makes up more than 70% in China and India. The predicted coal usage in different areas until 2040 is shown in Fig. 1.1. The coal demand in China has been increasing dramatically since 2000 and is expected to remain stable at a high level until 2040. Moreover, in 2040, the demand for coal in India is expected to reach about six times its value in 2000. On the other hand, coal usage in Japan is expected to remain constant in the future [2].

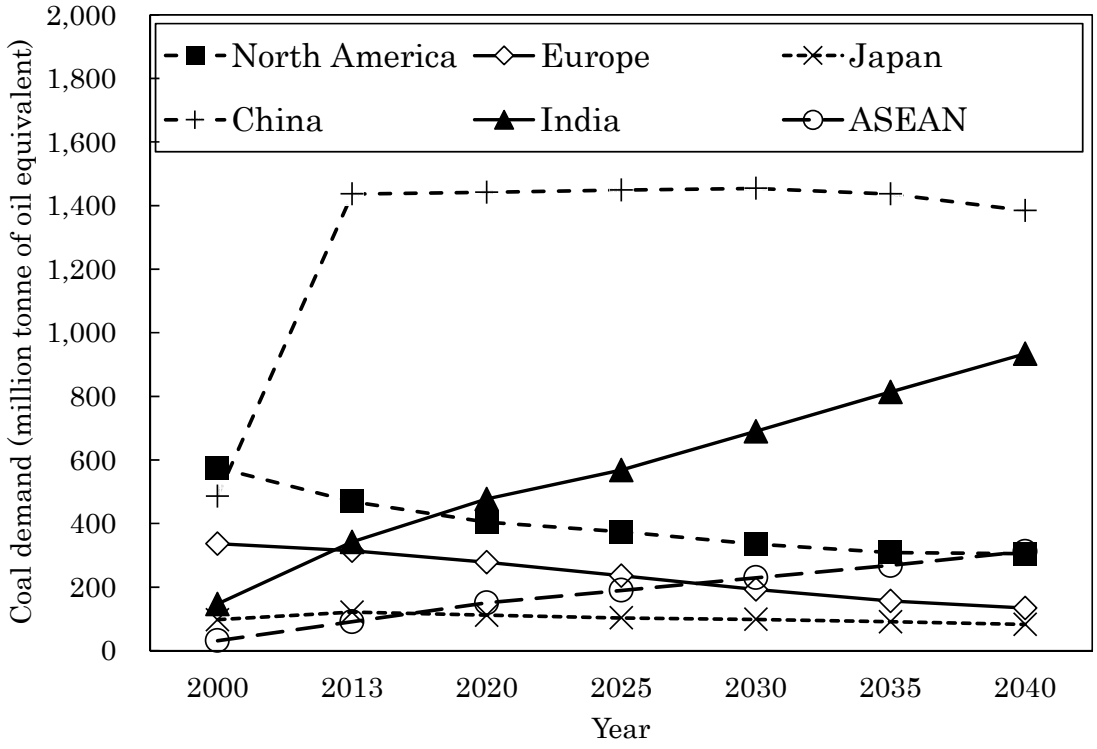

Fig. 1.1 Expected demand for coal in various areas until 2040 [1].

Japanese government aimed to establish low carbon society for reduction of CO_2 in 2030: zero-emission power sources should account for approximately 70% of all electricity production, and among the sources of energy production, nuclear energy should increase from 30% to 50%, and renewable energy should increase from 10% to 20% (compared to 2010). Unfortunately, largely in response to the Great East Japan Earthquake (March 11, 2011) and the Fukushima Daiichi nuclear disaster, the Japanese government recently reviewed its energy policy. In the strategic energy plan published by the Agency for Natural Resources and Energy in 2014, coal is currently positioned as an important base-load power supply in a portfolio of energy sources that balances reliability, low cost, and environmental suitability. Although coal emits large amounts of greenhouse gases, it is currently being re-evaluated as an important source of energy because it has the lowest geopolitical risk along with the lowest price per unit of heat energy among fossil fuels [3]. Besides the reduction of domestic emission, it is important to reduce greenhouse gas emissions on a global level, including developing countries, for an essential solution of global warming countermeasure. The Japanese government describes in the strategic energy plan that the system export of Japanese high-efficiency coal-fired power generation technology, joint crediting mechanism (JCM), and the technical development of carbon dioxide capture and storage (CCS), which is a CO_2 geological storage technique, will be promoted [4]. On the other hand, a tackle of de-coal combustion is progressing in the world and New

Emission Performance Standards (EPSs) and CCS regulations have already been enacted in America, Canada, and Britain; these countries have established strict guidelines for new coal-fired power plants. The investment of governments and private companies in diverse energy technologies will be required to reduce CO_2 emissions in developed countries. Among these technologies, CCS strategies will be important in reducing CO_2 emissions. According to modeling by IEA, to keep the increase in global temperature under 2°C until 2050, CCS should contribute 14% of CO_2 reductions (improvement of energy conservation, 38%; renewable energy, 30%; nuclear energy, 7%) compared to the 'business as usual' scenario [5]. The Institute of Energy Economics of Japan predicted that CCS will contribute to 32% of total CO_2 reduction in 2050 (Fig. 1.2) under the expectation of the IEE, that is included some anticipated policies in the future without a radical reform policy [6].

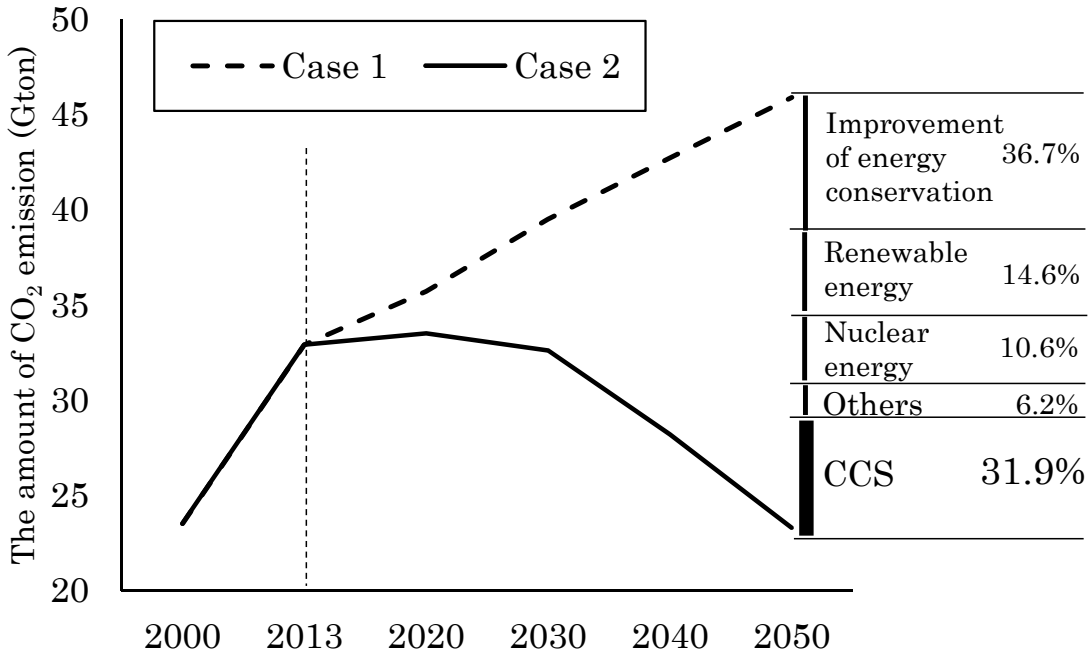

Case 1: Including some anticipated policies in the future without a radical reduction policy

Case 2: CO_2 reduction using various countermeasures

Fig. 1.2 Expected contributions of different countermeasures to total CO_2 reduction [6].

Currently, Today, the number of large-scale CCS projects in the operational or execution stage, 22, is twice than 2010 [7]. Most of the operational projects involve enhanced oil recovery (EOR), a technique used to enhance oil recovery by injecting CO_2 into low-production oil fields. In contrast, other CCS projects involve underground geologic CO_2 storage in basalt formations, unmineable coal seams, and deep saline aquifers. Examples of CCS projects utilizing CO_2 exhaust gas from natural gas plants include the following: the Val Verde Natural Gas Plant in Texas, United State (1972), the Shute Creek Gas Processing Facility in Wyoming, United State (1986), the Great Plains Synfuel Plant and Weyburn-Midale Project in Saskatchewan, Canada (2000), and the Sleipner CO_2 Storage Project (operational stage) in North Sea, Norway (1996). The following are examples of CCS projects utilizing CO_2 exhaust gas from coal power plants: the Boundary Dam Integrated Carbon Capture and Sequestration Demonstration Project in Saskatchewan, Canada (2014), the Kemper County Energy Facility in Mississippi, United State (2015), the Petra Nova Carbon Capture Project in Texas, United State (2016), the FutureGen 2.0 Project in Illinoi, United State (2017), and the White Rose CCS Project in North Yorkshire, United Kingdam (2019). The total CO_2 recovery capacity of the current CCS projects is estimated to be about 33 Mt/year; if projects currently in the define stage are included, the capacity is expected to increase to 64 Mt/year in 2020. Most CCS projects in defined or identified stage will use exhaust CO_2 gas from air and oxyfuel combustion processes.

The composition of CO_2 exhaust from coal-fired power plants differs based on the combustion system. Diagrams of the air combustion process and oxyfuel combustion process are shown in Fig. 1.2. Most current power plants use air-firing combustion systems due to their convenience and low cost; these systems have been thoroughly developed and studied. However, the oxyfuel combustion process for CCS is currently an area of focus. Oxyfuel combustion can directly recover a high proportion of CO_2 (>90%) at CO_2 storing unit because the oxyfuel combustion system runs with pure oxygen prepared by an air separation unit and recycles exhaust CO_2. Moreover, energy consumption for recovery of CO_2 in oxyfuel combustion system is less than air combustion system because the denitrification and desulfurization equipment are not required during CO_2 recovery process. This technology is available for established or new power plants and can reduce the CO_2 emitted to the atmosphere from conventional power plants by 95% [9].

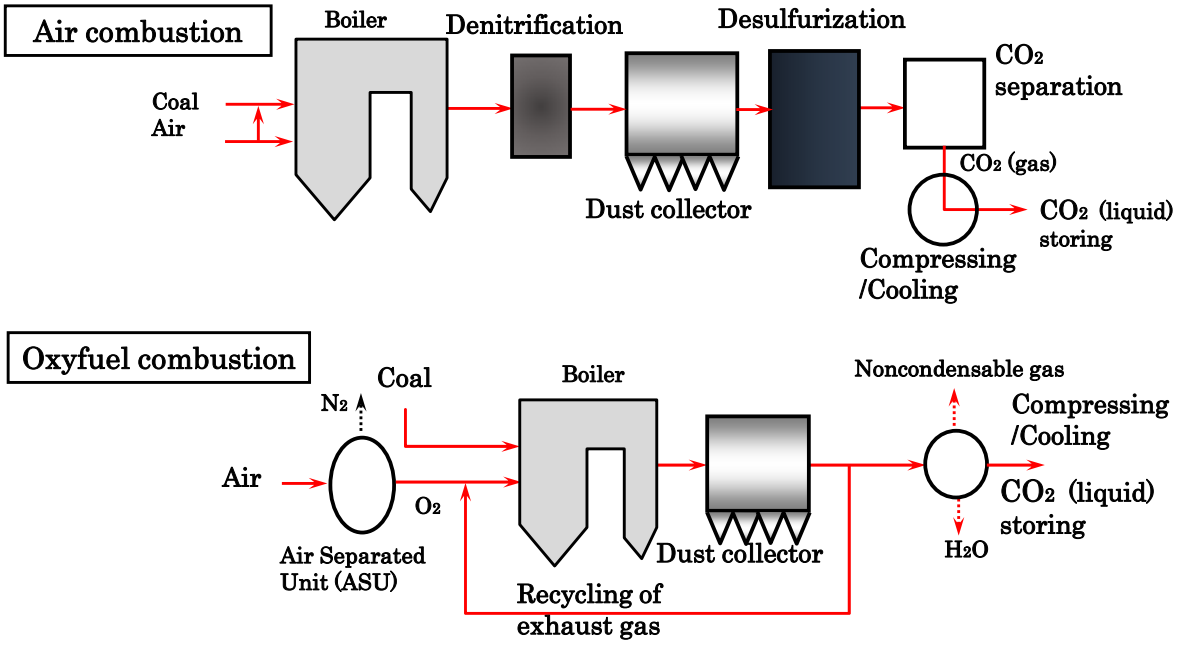

Fig. 1.3 Diagram of two coal combustion processes.

Japanese government scopes to the dissemination of high efficient combustion system toward foreign countries for the CO_2 reduction method mainly and also to promote the technical development of CCS positively. With a combination of government and private funding, the Tomakomai CCS project in Hokkaido, Japan, is slated to begin full-scale operation and monitoring in April 2016; CO_2 gas from an oil refinery will be injected into sandstone reservoirs with depths of 1,000 and 3,000 m [8]. However, the selection of sites for underground CO_2 reservoirs is difficult because of the many active faults in Japan. Thus, the Japanese government is conducting CCS projects in cooperation with foreign countries. For example, the Callide Oxyfuel Project, which is being conducted by the Japanese and Australian governments along with private companies, aims to demonstrate the reliability and operability of oxyfuel combustion systems for CCS. An oxyfuel combustion system was demonstrated in the 4th Callide A coal-fired power station located in Queensland, Australia, and CO_2 recovered from this plant was injected into a candidate reservoir site in Australia. The goal of this project was to evaluate the reliability of the plant, availability for using various coals, performance of the CO_2 compression and purification unit, and machine corrosion. In addition, the collection of basic oxyfuel combustion and CO_2 injection data, development of an evaluation tool, and evaluation of the CO_2 reservoir were carried out in a complementary study. This was the first project that succeeded in injecting the CO_2 recovered from oxyfuel combustion into an underground aquifer, and this strategy is a promising next-generation technology to counteract global warming [10].

The development and dissemination of CCS technology is required to improve the social,

economic, and technical problems. Enough explanation is required to understand the position and importance of CCS for global warming countermeasure toward a nation and industry, and should work the formation of social agreement. The government understands that large-scale CCS projects in the electricity sector are an important part of an effective energy portfolio to reduce CO_2 emissions and need to aim at establishment of a positive knowledge for CCS. The total cost of a CCS project is too high to be paid by a private company, and thus, remains a significant problem. Though projects had an incentive such as EOR can progress oil recovery with CO_2 geologic storage, high cost needs for CO_2 simple storage obviously. It is necessary to establish cost-sharing mechanisms among the private sector, government, and responsible organizations to deal with the cost burden of CCS systems, including legislative and taxation systems. In addition, CCS systems are still plagued by several technical issues, and many studies on their development are currently underway. The prevention of CO_2 leakage is the most important issue for injecting CO_2 into underground aquifers. The behavior of CO_2 in a reservoir and the effect of CO_2 on formation water and/or reservoir rock must be clarified in advance, in order to select a CO_2 reservoir site. Moreover, the safety of the cap rock overlying the reservoir must be evaluated in consideration of CO_2 leakage. Some studies have investigated the reaction behavior in the deep underground; however, the rock properties and reservoir conditions are variable, and basic data are not sufficient for geologic CO_2 storage. In addition, most previous studies investigated the storage of high-concentration CO_2; the possibility of storing CO_2 exhaust gas from power plant that contains other components is still being evaluated.

Many studies have been conducted on CO_2 recovery technology, and the CO_2 absorption efficiency has been improved. However, some problems related to CO_2 recovery still exist in oxyfuel combustion and air combustion systems. In oxyfuel combustion systems, high-concentration CO_2 gas containing low concentrations of NOx and SOx can be recovered from the exhaust gas without using denitration or desulfurization equipment because N_2 is separated from air before the firing process. Thus, it has advantage to decrease the amount of volume of exhaust gas and to contract a space of plant. However, the SO_2 concentration contained in the exhaust gas is 2–4 times greater than that for an air combustion system, and the NO_2 concentration is slightly higher (the origin of N is coal); thus, studies are being conducted to reduce the concentrations of these impurities by using alternate methods of combustion and CO_2 recovery or by evaluating various coal resources [11]. For example, the CO_2 recovered by the demonstration plant in the Callide Project contained 30 ppmv of SO_2 and NO_2 respectively [12]. On the other hand, in an air combustion system, a large-scale absorption unit and a regeneration unit are required to recover high-concentration CO_2 [13]. More than 120°C of heating method is applied in the regeneration unit to separate CO_2 from an amine solution absorbed CO_2 in the absorption unit using chemical absorption method and thus the reduction of energy for the CO_2 separation is desired.

Previous studies on the geologic storage of CO_2 have investigated the reaction process of

CO_2-rock-brine in the CO_2 reservoir, changes of water or rocks, and dissolution of metals by CO_2 in the aquifer [14, 15]. Moreover, the degradation or corrosion of CO_2-injection well materials in contact with CO_2 have been intensively investigated [16, 17]. However, geochemical studies with CO_2 gas containing impurities such as oxyfuel combustion exhaust CO_2 gas are little. In this paper, I investigated the effects of impurities (e.g., NO_2 and SO_2) in CO_2 gas from the oxyfuel combustion process on reservoir rock and CO_2 injection well materials with the goal of resolving the technical issues in CCS. Moreover, I investigated a method of CO_2 desorption from CO_2-absorbed amine solution at low temperature in a short time because the efficient separation and recovery of CO_2 from the exhaust gas in air combustion process are desired.

This paper addresses mainly two issues. Based on geochemical experiments, Chapters 2 and 3 describe the effects of NO_2 and SO_2 contained in the exhaust CO_2 gas from oxyfuel combustion on the reservoir rock and CO_2 injection well materials. Chapters 4 and 5 describe the application of degasification using ultrasound to develop a new method for effective CO_2 desorption from the exhaust gas in an air combustion system. Finally, the conclusions are described in Chapter 6.

Chapter 2

Effect of NO_2 in exhaust gas from an oxyfuel combustion system on the cap rock of a CO_2 injection site

2.1 Introduction

CO_2 is one of the gases that can cause global warming. Because of the increase of the global market cost of natural gas and the rapid increase in fossil fuel consumption in developing countries, it has been estimated that the amounts of CO_2 gas emitted from coal-fired power stations will increase in the future. Some electricity is currently generated from renewable sources of energy; however, approximately 40% of the electricity is generated using coal. More CO_2 is emitted per unit of electricity generated by coal-fired power plants than by plants using other fossil fuels [18, 19]. Therefore, several developments are currently being studied for the decrease and use of exhaust CO_2 gas. Carbon dioxide capture and storage (CCS) is a technique to separate and recover the exhaust CO_2 gas from a coal-fired power plant and to store CO_2 in basalt formations, unmineable coal seams, and deep saline aquifers underground [20]. Some actual proof and operation of CO_2 injection have been conducted at several sites such as that for Enhanced Oil Recovery, however, professional technology expansion has not yet progressed because of operation costs and environmental assessment problems.

For CO_2 injection, research on the effects of supercritical CO_2 on underground aquifers is required. Many studies on CO_2 reservoir and rock-water reactions have been conducted as part of research on CCS. For example, Curtis et al. (2012) evaluated a supercritical CO_2-rock-brine reaction using a sample that simulated the composition of the Madison Limestone, which is a sulfur-rich CO_2 aquifer, and described the dissolution and reprecipitation of minerals or mineral trapping of CO_2 [21]. Uemura et al. (2011) described the migration of supercritical CO_2 in an aquifer using X-ray CT scanning. Payan et al. (2012) studied leaching of metal oxides by experiment and model analysis using the reactions between an outcrop sample of an aquifer and ion-exchange water or brine [14, 22].

When supercritical CO_2 is injected underground, the prevention of CO_2 leakage from aquifers must be assessed. In general, when a CO_2 reservoir is selected, a low-permeability cap rock such as shale rock must be present over the reservoir. During geologic carbon storage, it is expected that there will be contact between the lower boundary of the cap rock and the CO_2-saturated water in the reservoir. Crack development and leaching of metallic ions will occur as a result of mineral dissolution reactions between the cap rock boundary and formation water because the pH is decreased by the injection of CO_2. Alemu et al. (2011) studied the geochemical reaction process between shale and water using a batch reaction experiment and numerical modeling under temperature and pressure conditions of 80–250 °C and 40–110 bar and compared the reactivity of carbonate-rich shale and shale rich in clay minerals [15].

In some clean coal technologies (CCT), oxyfuel combustion technology can increase the concentration of CO_2 in exhaust gas and recover CO_2 with high efficiency. This technology is available for established or new power plants and can reduce the CO_2 emitted to the atmosphere by 95%. Moreover, this technology can recover high-concentration CO_2 (>90%) directly and reduce the energy consumption required to recover CO_2, because this combustion system runs with pure oxygen prepared by an air separation unit and recycles exhaust CO_2. Unlike the post-combustion system on air-firing, the consumption of energy for CO_2 recovery is low because denitration equipment and CO_2 sequestration equipment are not required. The amount of NO_2 in the exhaust gas of this process is reduced to one-third of that in gas exhausted from an air combustion system [9, 23-26]. Because of these advantages, oxyfuel combustion is a promising technology for CCT.

The world's first actual a pilot project of oxyfuel combustion has been in operation since 2008 in the Callide A coal-fired power station located in Queensland, Australia, which uses a consistent system from CO_2 capture to storage into candidate CO_2 injection site. In this project, we conducted laboratory geochemical experiments to study the chemical effects of the injection of oxyfuel combustion CO_2 gas into an underground aquifer on rock.

It has been considered that many data obtained from the results of CO_2-rock-water reaction in previous studies were applicable to the oxyfuel combustion system (herein termed oxyfuel combustion CO_2). However, oxyfuel combustion CO_2 contains small amounts of NO_2 and SO_2 because denitration and desulfurization equipment are not used for CO_2 removal, unlike air-fired post-combustion systems [23-26]. Thus, it is assumed that compared to pure CO_2 these acid gases make the formation water more acidic and cause dissolution of cap rock. Some studies have evaluated the effect of SO_2 contained in CO_2 on formation water or minerals using experiments or numeral modeling. Renard et al. (2014) and Pearce et al. (2015) described the effects of SO_2 and O_2 contained in injected CO_2 gas on the reservoir minerals using a core sample obtained from a CO_2 injection site [27, 28]. Li et al. (2011) and Ellis et al. (2010) clarified the long-term behavior of CO_2 sequestration from the results of the effect of SO_2 in injection CO_2 gas on a reservoir using model analysis. The effect of SO_2 contained in CO_2 gas was described in some previous studies, and SO_2 caused dissolution of minerals and increased the porosity of the rock because of the acidity of the solution [29, 30].

However, few studies have conducted geochemical analyses using experimental drill core samples from actual candidate CO_2 injection sites. Moreover, oxyfuel combustion CO_2 from Callide may contain 0–30 ppmv NO_2 [12], considering the sequestration of CO_2 in underground aquifer. No previous studies have considered the effect of NO_2 contained in CO_2 gas on shale acting as a cap rock. NO_2 has acidic properties in solution, similarly to SO_2 gas, and thus, it might be expected to cause enhanced mineral dissolution. In this study, we conducted geochemical experiments to investigate the effect of NO_2 on mineral dissolution and metal leaching using a drill core sample of cap rock obtained from West Wandoan in the Surat basin, which is a candidate CO_2 injection site of low salinity.

2.2 Experimental apparatus and procedure

2.2.1 Core sample

A shale sample was obtained from a vertical drill-core obtained from West Wandoan 1 well in the Surat Basin, Queensland, Australia. This site is a candidate site for a CO_2 storage reservoir. The location of the drill site and the simplified lithology of the drill core are shown in Fig. 2.1. The Precipice Sandstone has been proposed as a reservoir for CO_2 injection between 1,165−1,247 m depth in the Callide Oxyfuel Project. In this study, we used a shale sample from the Evergreen Formation (1,024 m depth), which is a cap rock layer for CO_2 storage.

The shale sample was quantitatively and qualitatively analyzed using X-ray fluorescence (XRF, EDX-7000, Shimadzu) and an X-ray diffraction analyzer (XRD, Ultima IV, Rigaku). In addition, microscopic observation was conducted on thin sections of the shale to observe changes in minerals in the shale after the experiments. Table 1 lists the chemical composition of the shale sample analyzed by XRF, and Table 2 lists the minerals, general chemical formulae, and mineral abundances estimated by X-ray diffraction analysis, microscopic observations using the point-counting method, and whole-rock chemical composition analysis. Chemical compositions of minerals are based on Deer et al. (1992), which were used for the calculation of mineral abundances [31].

A photomicrograph of the shale is shown in Fig. 3. The shale comprises Fe-chlorite (chamosite), illite-smectite (nontronite) mixed-layer, kaolinite, quartz-amorphous silica, carbonaceous minerals, and prehnite. Fe-chlorite, illite-smectite mixed layer and kaolinite occur as aggregates with an average size of 150 μm and appear light green in color under the microscope. Carbonaceous materials are present as aggregates with an average size of 150 μm and are brown in color refer to Fig. 3. Quartz occurs as anhedral crystals with averaged size of 150 μm. Prehnite is present as tabular- or fan-shaped euhedral crystals with an average size of 150 μm.

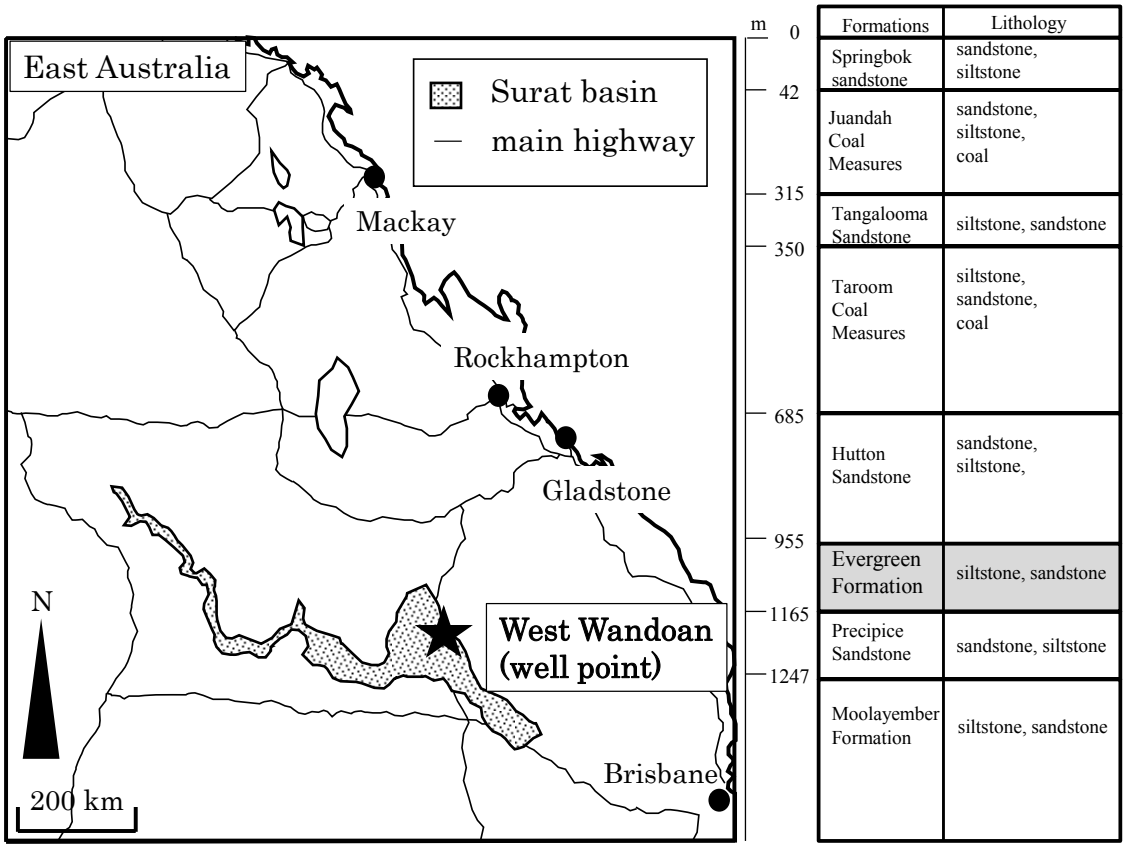

Fig. 2.1 Location of the boring well and simplified lithology of the drill core sample.

Fig. 2.2 Drill core sample of shale from the Evergreen Formation at depth of 1,024 m.

Table 2.1 Bulk chemical composition of the shale sample analyzed by XRF.

					wt.%
SiO_2	50.3	TiO_2	0.97	Al_2O_3	21.9
Cr_2O_3	0.02	Fe_2O_3	16.9	MnO	0.04
ZnO	0.02	MgO	0.44	CaO	0.62
K_2O	1.65	V_2O_5	0.10	SrO	0.05
SO_3	0.05			LOI*	6.94

*LOI = Loss on Ignition

Table 2.2 Constituent minerals of the shale sample and their abundances.

Minerals	Chemical formula	Abundance (vol.%)
Fe-chlorite (chamosite)	$(Fe, Mg)_6(Si, Al)_4O_{10}(OH)_8$	27.2
Carbonaceous minerals	C	2.0
Quartz/amorphous silica	SiO_2	18.0
Illite-smectite (nontronite) mixed layer	$K_{1\text{-}1.5}Al_4(Si_{7\text{-}6.5}Al_{1\text{-}1.5}O_{20})(OH)$ -$(K, Na, Ca_{1/2})_{0.25\text{-}0.60}(Fe, Al)_2(Si_{3.4\text{-}3.75}, Al_{0.25\text{-}0.10})O_{10}(OH)_2$	27.0
Kaolinite	$Al_4Si_4O_{10}(OH)_8$	25.0
Prehnite	$Ca_2Al_2Si_3O_{10}(OH)_2$	0.8

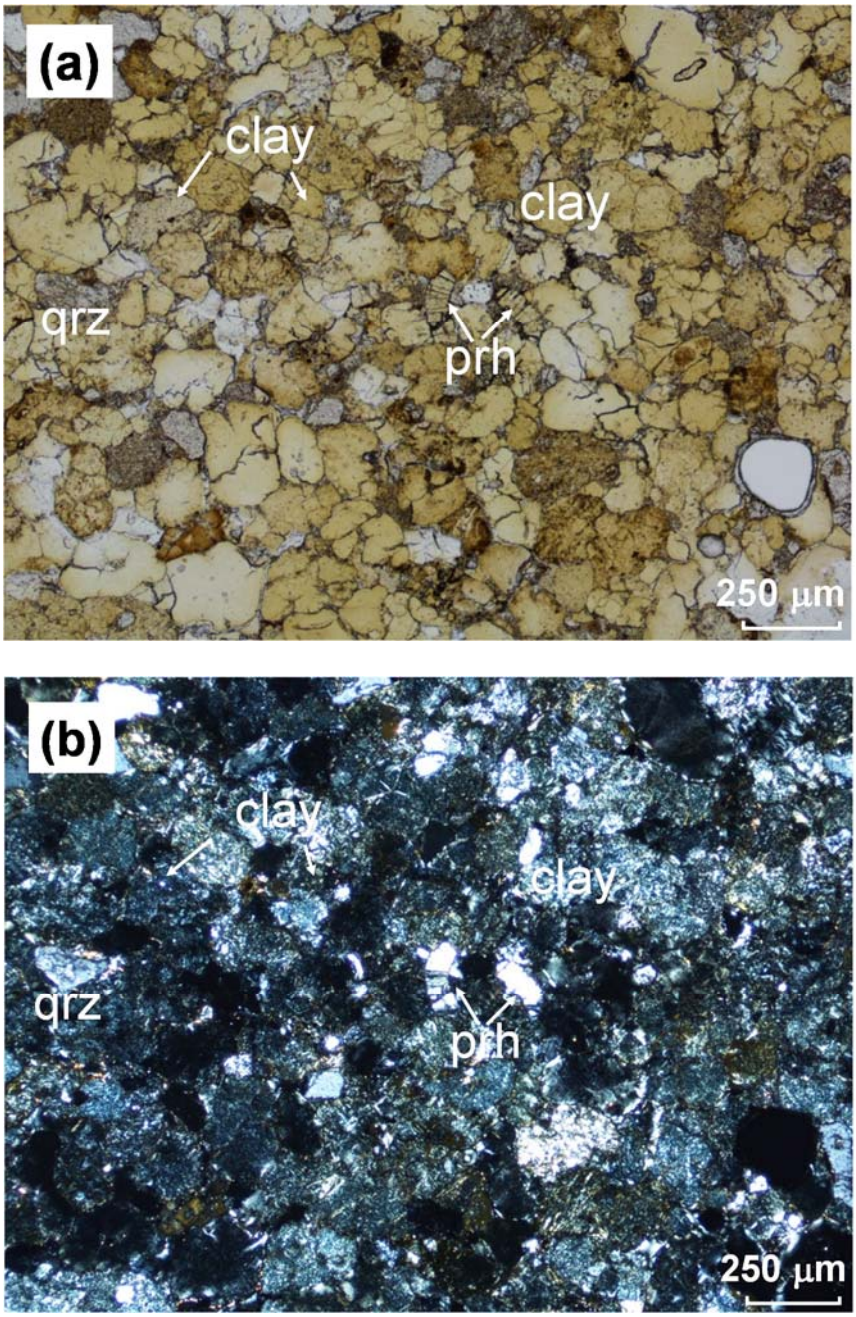

Fig. 2.3 Photomicrographs of thin sections of the shale sample. (a) plane-polarized light, and (b) crossed polars.

Abbreviations: clay: aggregation of Fe-chlorite, illite-smectite mixed-layer, and kaolinite, qrz: quartz, prh: prehnite, carb: carbonaceous minerals.

2.2.2 Experimental conditions

The experimental gases used in this geochemical study are listed in Table 3. We prepared four mixtures of gases (SG1, SG2, SG3, and SG4, Sumitomo Seika), which simulate oxyfuel combustion CO_2, and high-concentration CO_2 gas (purity > 99.99%, Nihon Ekitan). SG1 and SG3 were prepared to simulate the gaseous concentrations and species contained in actual oxyfuel combustion CO_2 according to Callide oxyfuel specifications in order to allow comparison of the effects of impurities (SO_2 and NO_2). SG2 and SG4 were prepared with ten times the actual reported amounts of SO_2 and NO_2, respectively, to facilitate study of the effects of impurities in oxyfuel combustion CO_2. As other researchers have reported higher concentrations of impurities are also possible if a plant was not operating correctly, or from other capture sources e.g. cement.

We prepared 90 mmol/l NaCl solution to simulate the formation water using NaCl (Wako Co. JAPAN) and ion-exchange water, which was used to simulate formation the water of the general injection aquifer. The experimental apparatus is shown in Fig. 2.4. In this study, the reaction apparatus was constructed from stainless steel (SUS316) to correspond to high pressure and temperature (8.5 MPa and 60 °C). The reactor vessel that has a volume of 500 ml was constructed and the experiment was conducted with a shale sample (about 30 g) and solution (about 300 ml) in the vessel. The solution was vacuum-deaerated for 30 min before the experiment to remove O_2 (< 2 ppmv). The reactor was joined to a syringe-type pump for the injection of high-pressure gas to maintain constant pressure for the duration of the experiment. The solution was constantly stirred at 420 rpm with stirring blade and the inner pressure and temperature (measured by sensors) were recorded every 5 min by a data logger during the experiment.

The experiment was continued for 21 days. During the experimental time, water sampling was conducted at certain points: 0 (immediately after the start of the experiment), 0.25, 1, 2, 3, 5, 7, 14, and 21 day. Quantitative analysis of leached K, Mg, Ca, Al, Si, Fe, and NO_3^- concentrations and pH measurement were conducted. Water samples (6 ml) for analysis were directly collected. Mg, Ca, Al, Si, and Fe were measured using an inductively coupled plasma-optocal emission spectromet (ICP-OES, Seiko Instruments), and K and NO_3^- were measured using an ion analyzer (IA-300, TOA-DKK). The pH was measured immediately after water sampling with a pH meter (F-72, Horiba). A propotion pf the solution (2 ml) was recovered with 11 ml monoethanolamine (5 mol/l) so that CO_2 would not be released by the decreasing pressure, and the amount of CO_2 in the solution (total inorganic carbon; TIC) was determined using a total organic carbon analyzer (TOC-V_{CSH}, Shimadzu).

Table 2.3 Gas compositions

	CO_2	N_2 (%)	SO_2 (ppmv)	NO_2 (ppmv)
SG1	Balance	2.0	35	
SG2	Balance	2.0	356	
SG3	Balance	2.0		36
SG4	Balance	2.0		318
CO_2	>99.99%			

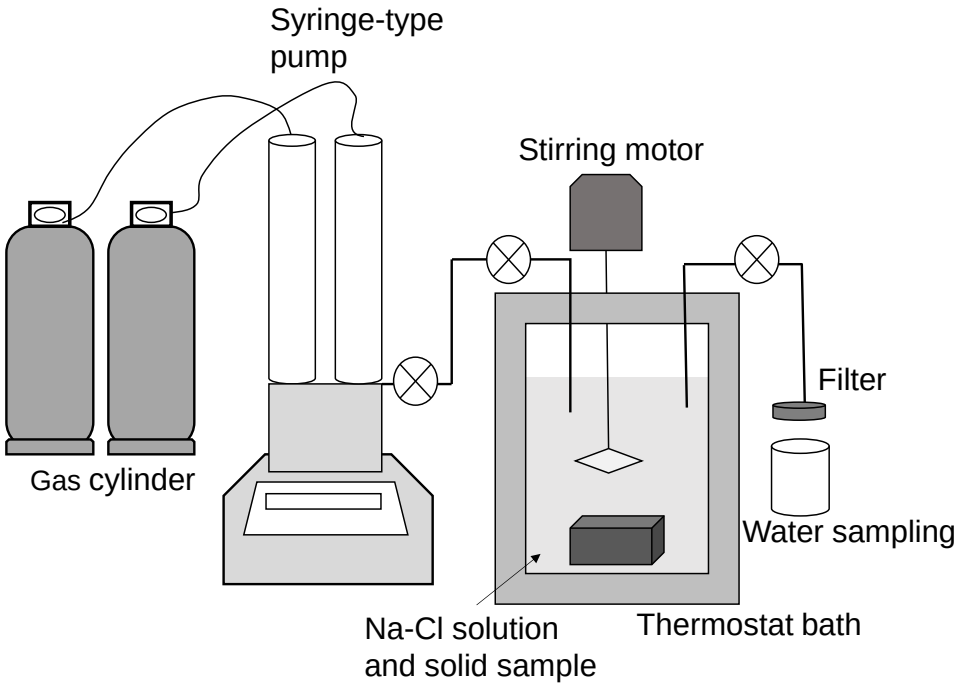

Fig. 2.4 Experimental apparatus

2.3 Results and Discussion

The measurements of pH, TIC, and ion concentrations obtained for each gas conditions before the experiment and after 21 days are listed in Table 2.4. Approximately 930 mmol/l of CO_2 gas was dissolved into 90 mmol/l NaCl solution under conditions of 8.5 MPa and 60°C with reference to the previous study of Duan and Sun (2003) [32]. It was considered that the injected CO_2 gas was dissolved sufficiently in the solution because the results of measured TIC for each gas condition at 21 day were similar to the theoretical values refer to Table 2.4.

The changes of ion (Ca, Fe, Mg, and K) concentrations in sampling water are shown in Fig. 2.5. The changes in the concentration of each ion were stable after the 7th day. The Ca concentration increased gently from immediately after the start of the experiment to the 3rd day and was then stable under the condition of pure CO_2. The same behavior was observed for conditions SG1 and SG3. In contrast, the Ca concentration increased until the 3rd day in condition SG2, which contained a high concentration of SO_2 (356 ppmv): the Ca value was three times higher than that of pure CO_2. Under condition SG4 with high concentration of NO_2 (318 ppmv), the Ca concentration exhibited the same behavior as for SG2 until the 2nd day and then decreased to a value similar to that of pure CO_2. The Fe concentration increased gently from immediately after the start of the experiment to the 7th day under the condition of pure CO_2. The results for condition SG1 were similar to those for pure CO_2. The amount of Fe leached for condition SG3 was lower than that for pure CO_2. Under condition SG4, the Fe concentration increased until the 2nd day and the value was 1.4 times that of pure CO_2. Furthermore, the concentration was stable after the 3rd day and reached a similar value to that of pure CO_2 on the 7th day. Under condition SG2, the Fe concentration increased from immediately after the start of the experiment to the 7th day and reached a higher value compared with that of the other experiments. The Mg concentration increased gently during the experiments. The results for SG1 and SG3 were similar to that of pure CO_2 and those of SG2 and SG4 were about 1.7 times that of pure CO_2. The K concentrations for conditions SG1 to SG4 were similar to the results for pure CO_2.

The changes in pH during the experimental time for each gas conditions are illustrated in Fig. 2.6. The pH decreased immediately after the start of the experiment by the dissolution of CO_2 and then showed a tendency to increase. The increase in pH during the reaction was considered to occur by mineral buffering [33]. Furthermore, the results for pH under SG1 and SG3 were similar to the results for pure CO_2, indicating that ~35 ppmv SO_2 or NO_2 did not affect the change of pH. The pH decreased immediately after the start of the experiment to 4.74 under condition SG2, which contained 356 ppmv SO_2. In contrast, under condition SG4, which contained 318 ppmv NO_2, the pH fell immediately after the beginning of the experiment but increased to 5.79 immediately and then to 6.32 during the experiment; these were the highest values of all of the experimental gas conditions.

We compared the results of this study with those of previous studies that had conducted similar experiments using CO_2. Table 2.5 shows a comparison of the mineral compositions and ion

concentrations in the solution after 21 days in this study and previous studies. Alemu et al. (2011) using CO_2 and clay-rich shale described how the pH was decreased by the dissolution of CO_2 and the concentrations of leached K, Ca, Fe, and Mg were comparatively stable. The pH decreased after CO_2 injection and subsequently increased from initial value (about 7) to 8.1 after 21 days. Fe, Mg, and K were leached from chlorite, illite, and siderite in the shale and the pH increased as a result of mineral buffering [15]. The results of this study were compared with those of CO_2 injection experiments using a core sample by Lu et al. (2012) [34]. However, differences in the amount of ion leaching that occurred because the pressure, temperature, and experimental time were different; K, Ca, and Mg were leached and their concentrations were stable after leaching. Considering the results of these previous studies, the pH decrease in this study resulted from the dissolution of CO_2 while Fe and Mg were leached from Fe-chlorite. Additionally, Ca and K were leached from prehnite, and illite-smectite mixed-layer in the shale, respectively. In addition, the pH fell immediately after commencement of the experiment and then increased as a result of mineral buffering.

Only a few studies have conducted experiments using CO_2 containing impurities such as gas mixtures SO_2 and CO_2 or O_2 and CO_2 of this study. Pearce et al. (2015) described water-rock reactions using Evergreen Formation shale core sections from the Surat Basin, Australia with water and CO_2 containing 1,600 ppmv SO_2 [28]. That study described that the initial pH value of 5.7 decreased to 2.2 after 48 h and increased slightly to 2.7 after 384 h. Si and Al were leached from quartz and kaolinite and Fe was leached from chlorite or siderite because the pH was greatly decreased by the inclusion of 1,600 ppmv SO_2. In contrast, the pH increase was small because a higher concentration of sulphuric acid was generated.

In this study, the pH for SG2 (356 ppmv SO_2) showed a larger decrease than that of pure CO_2, and the amounts of K or Ca leached were larger than those in Pearce et al. (2015). Therefore, we conclude that the pH increase was large because SG2 has less SO_2 so would generate less sulphuric acid to lower the pH.

Table 2.4 Values of pH, TIC, and cations of the solution obtained at the initial conditions and after 21 days of experiment for all gas conditions.

Gas conditions	Time	pH	TIC (mmol/l)	Ion concentrations (mmol/l)					
				K	Mg	Ca	Al	Si	Fe (II, III)
SG1	Initial	5.90		-	-	-	-	-	-
	21 day	6.02	958	2.47	0.48	2.06	0.00	0.79	1.82
SG2	Initial	5.62		-	-	-	-	-	-
	21 day	5.91	939	2.71	1.03	3.79	0.00	0.81	2.97
SG3	Initial	5.09		-	-	-	-	-	-
	21 day	6.03	936	1.93	0.44	1.78	0.00	0.86	0.81
SG4	Initial	5.26		-	-	-	-	-	-
	21 day	6.32	891	2.58	0.88	2.51	0.00	0.79	1.48
CO_2	Initial	5.90		-	-	-	-	-	-
	21 day	6.09	955	2.47	0.41	2.21	0.00	0.80	1.57

SG1: SO_2 (35 ppmv), SG2: SO_2 (356 ppmv), SG3: NO_2 (36 ppmv), SG4: NO_2 (318 ppmv)

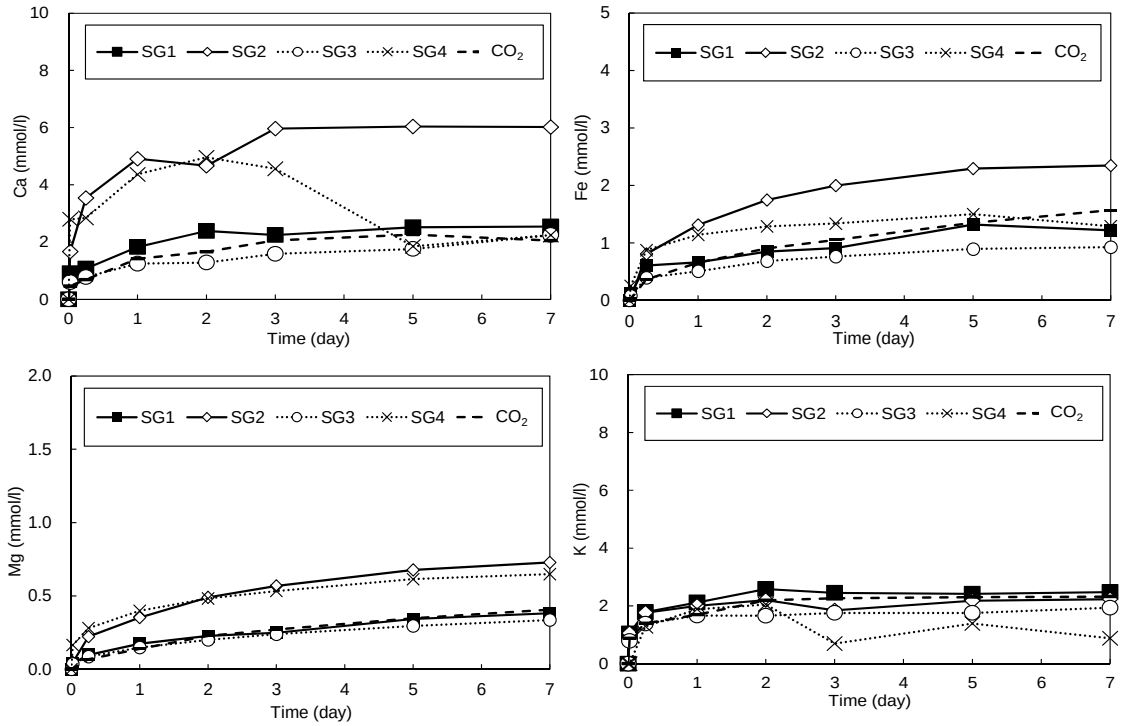

Fig. 2.5 The concentrations of leached ions (Ca, Fe, Mg, and K) in the solution for each gas conditions during gas-water-rock reactions. (SG1: SO_2 (35 ppmv), SG2: SO_2 (356 ppmv), SG3: NO_2 (36 ppmv), SG4: NO_2 (318 ppmv))

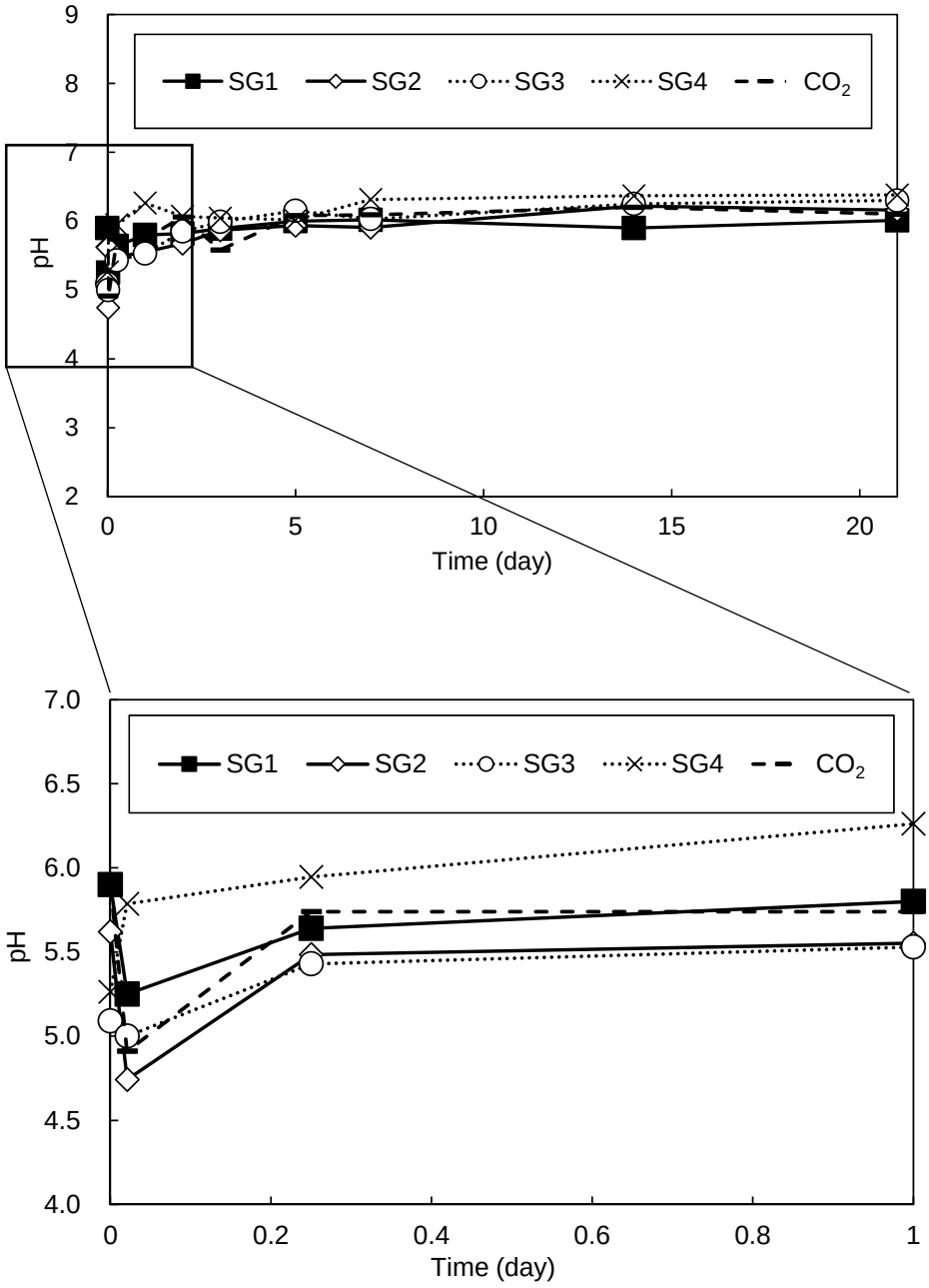

Fig. 2.6 Change of pH in the solution for each gas conditions during gas-water-rock reactions.

Table 2.5 Modal compositions of minerals in shale cap-rocks and the amounts of cations leached in this study and previous studies.

	Mineral (vol. %)								
	Fe-Chlorite	Quartz	Illite-smectite	Kaolinite	Prehnite	Carbonacous			**This study**
	27.2	18.0	27.0	25.0	0.8	2.0			
Gas	**Amount of leaching cations after experiment (mmol/l)**								8.5 MPa, 60 °C
condition	K	Mg	Ca	Al	Si	Fe		**pH**	21 day
CO_2	2.47	0.41	2.21	0.00	0.80	1.57		6.10	
SG2	2.71	1.03	3.79	0.00	0.81	2.97		6.16	
SG4	2.58	0.88	2.51	0.00	0.79	1.48		6.38	
	Mineral (vol. %)								
	Chlorite	Quartz	Illite	Plagioclase/albite	Siderite	Pyrite			**Alemu et al. (2011)**
	38.0	26.0	22.0	8.00	5.00	1.00			
Gas	**Amount of leaching cations after experiment (mmol/l)**								11 MPa, 80 °C
condition	K	Mg	Ca	Al	Si	Fe		**pH**	21 day
CO_2	2.36	1.95	2.46	0.09	3.31	3.52		8.1	
	Mineral (vol. %)								
	Quartz	Chlorite	Kaolinite	Illite	Anatase				**Lu et al. (2012)**
	80.7	14.1	1.7	0.8	2.6				
Gas	**Amount of leaching cations after experiment (mmol/l)**								32.4 MPa, 120 °C
condition	K	Mg	Ca	Al	Si	Fe	Sr	Ba	**pH** 75 day
CO_2	43.9	58.0	423	0.371	0.360	3.04	12.6	0.510	5.00–5.20
	Mineral (vol. %)								
	Quartz	Kaolinite	K-feldsper	Ankerite	Siderite	Chlorite	Fe oxides		**Pearce et al. (2015)**
	43.0	18.0	10.0	10.0	4.00	4.00	4.00		
Gas	**Amount of leaching cations after experiment (mmol/l)**							**pH**	12 MPa, 60 °C
condition	K	Mg	Ca	Al	Si	Fe	Sr	Mn	2.7 6.4 day
$CO_2 + SO_2$ (0.16%)	0.266	0.934	0.938	0.954	2.43	7.73	0.0388	0.209	

In discussing the leaching of Ca, Fe Mg, and K from cap-rock minerals for each gas conditions, we assumed that Fe and Mg were leached from Fe-chlorite, Ca was leached from prehnite, and K was leached from the illite-smectite mixed-layer, with reference to previous studies [35-40]. Photomicrographs of shale before and after the experiment under condition SG4 are reproduced in Fig. 2.7. The colors of the aggregations of chlorite, illite-smectite mixed-layer, and kaolinite in the shale had changed from pale green to light brown, and the prehnite had altered from almost colorless or pale yellow/green to greenish-tinted yellow. This change was also observed for CO_2, SG1, SG2, and SG3. The color changes of chlorite and prehnite under the microscope and the water-rock reaction experimental results suggest that Fe, Mg, and Ca were leached by the alteration of chlorite and prehnite in the shale. It was determined that the chlorite was Fe-Mg chlorite from the results of XRD, whole-rock analyses, and microscopic observations. Thus, the amount of leached Mg was lower than that of Fe, as shown in Fig. 2.5, because the initial amount of Mg was much lower than that of Fe (Table 2.1).

A comparison of the chemical compositions of shale samples after the experiment for SG1 to SG4 measured using XRF is provided in Table 2.6. For the composition of the massive sample after experiments under each gas conditions, we measured surfaces showing both small and large amounts of discoloration. These areas of the shale sample after experiment for condition SG4 are illustrated in Fig. 2.8. The amount of Fe was markedly higher than the amounts of other ions on surfaces showing significant discoloration. In addition, the amount of Ca in $SG4^b$ was higher than that in other conditions. For condition SG4, the concentration of Ca increased until the 3rd day and then decreased (Fig. 2.5). Compared with the result for SG2, the Fe concentration for SG4 showed a similar value until the 1st day but was different after the 2nd day. Therefore, it is presumed that some of the Fe and Ca that had leached into the solution had become precipitated as compounds on the rock surface.

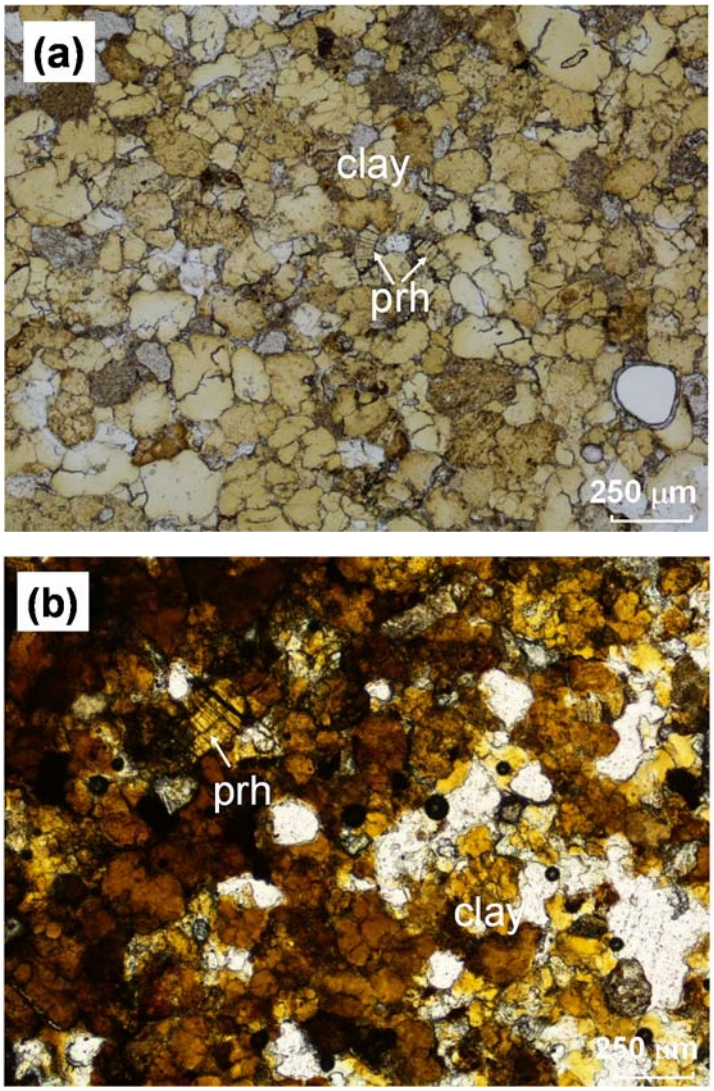

Fig. 2.7 Photomicrographs of shale in plane-polarized light (a) before the experiment and (b) after the experiment for condition SG4.

Table 2.6 Chemical composition of shale samples after the experiment for conditions SG1 to SG4.

Oxides (wt%)	Initial	SG1[a]	SG1[b]	SG2[a]	SG2[b]	SG3[a]	SG3[b]	SG4[a]	SG4[b]
SiO_2	54.0	57.4	46.3	52.6	52.8	62.0	43.3	52.7	35.7
Al_2O_3	23.5	25.7	22.3	24.3	23.4	25.1	20.6	24.8	13.1
Fe_2O_3	18.2	13.3	26.9	18.8	19.6	7.14	32.0	18.2	41.0
K_2O	1.78	2.08	1.56	1.60	1.59	2.10	1.65	1.59	2.20
TiO_2	1.05	1.01	1.16	1.07	1.18	1.95	1.01	1.13	1.72
MgO	0.47	0.60	0.41	0.66	-	0.41	0.33	0.70	-
CaO	0.67	0.45	0.40	0.48	0.48	0.35	0.41	0.49	0.78
others	0.31	0.46	0.93	0.50	1.00	0.99	0.73	0.34	5.45

SG1: SO_2 (35 ppmv), SG2: SO_2 (356 ppmv), SG3: NO_2 (36 ppmv), SG4: NO_2 (318 ppmv)

[a] Point with a small amount of discoloration (measurement diameter is 10 mm)

[b] Point with a large amount of discoloration (measurement diameter is 3 mm)

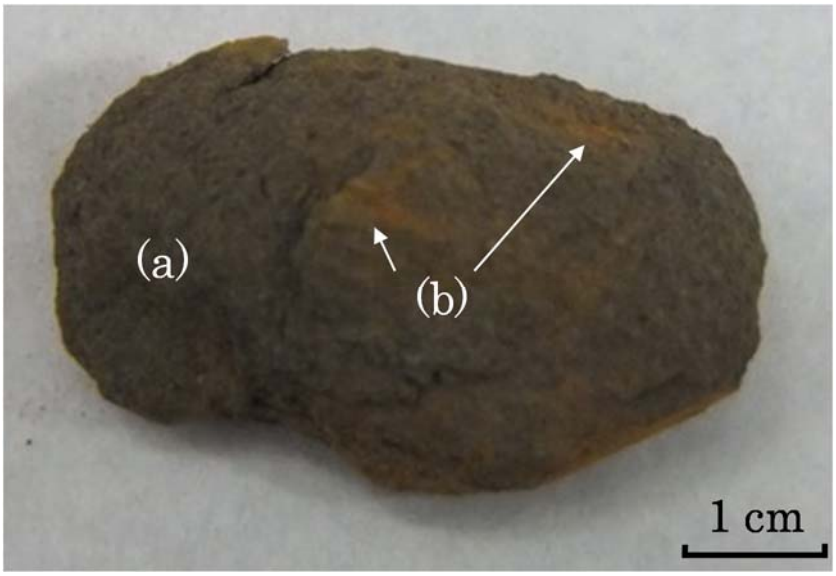

Fig. 2.8 Picture of the shale sample after the experiment with condition SG4.

(a) Area with a small amount of discoloration (b) Areas with large amounts of discoloration

When CO_2 containing SO_2 or NO_2 is injected into an underground aquifer, the reactions described below are expected to occur in addition to the reaction of CO_2 dissolution in formation water. The pH is decreased markedly when the concentration of SO_2 in the injected CO_2 is high, such as in condition SG2 in this study, because some of the SO_2 forms sulfuric acid and creates hydrogen ions in the formation water, as described by equations 1 and 2 [30, 41]. NO_2 reacts with water easily and acts to decrease the pH, as in equations 3 and 4. However, Fe^{2+} and NO_3^- in the solution release or receive electrons, as described in equations 5 and 6 [42]. Thus, we postulate that when Fe is present in shale such as in this experimental sample, leached Fe^{2+} works as a reducing agent for NO_3^-. Because hydrogen ions are consumed in the solution, as in equation 6, the pH fall is buffered. This is the reason for the pH decrease being less reduce in condition SG4 compared with that in condition SG2.

$$SO_2 + H_2O \rightarrow H_2SO_3 \quad (1)$$

$$H_2SO_3 \rightarrow H^+ + HSO_3^- \quad (2)$$

$$3NO_2 + H_2O \rightarrow 2HNO_3 + NO \quad (3)$$

$$HNO_3 \rightarrow H^+ + NO_3^- \quad (4)$$

$$Fe^{2+} \rightarrow Fe^{3+} + e^- \ (0.770\ V\ vs.\ SHE) \quad (5)$$

$$NO_3^- + 4H^+ + 3e^- \rightarrow NO + 2H_2O \ (0.960\ V\ vs.\ SHE) \quad (6)$$

A comparison of the concentration of NO_3^- and the pH value over a 3-day period under condition SG4 with and without a core sample is illustrated in Fig. 2.9. NO_3^- was not detected until the 3rd day with a core sample but increased from immediately after the start to the 3rd day without a core sample.

The pH increased immediately after the start with a core sample but declined to 2.9 and was stable at a low value until the 3rd day without the core sample. From these results, NO_3^- and H^+ were consumed because oxidation-reduction reactions occurred between leached Fe^{2+} and NO_3^- when the core sample was present in the solution. Therefore, it is presumed that the solution became reducing immediately after gas injection as a result of oxidation-reduction reactions between Fe^{2+} and NO_3^-, unlike conditions SG2 (356 ppmv SO_2) and pure CO_2.

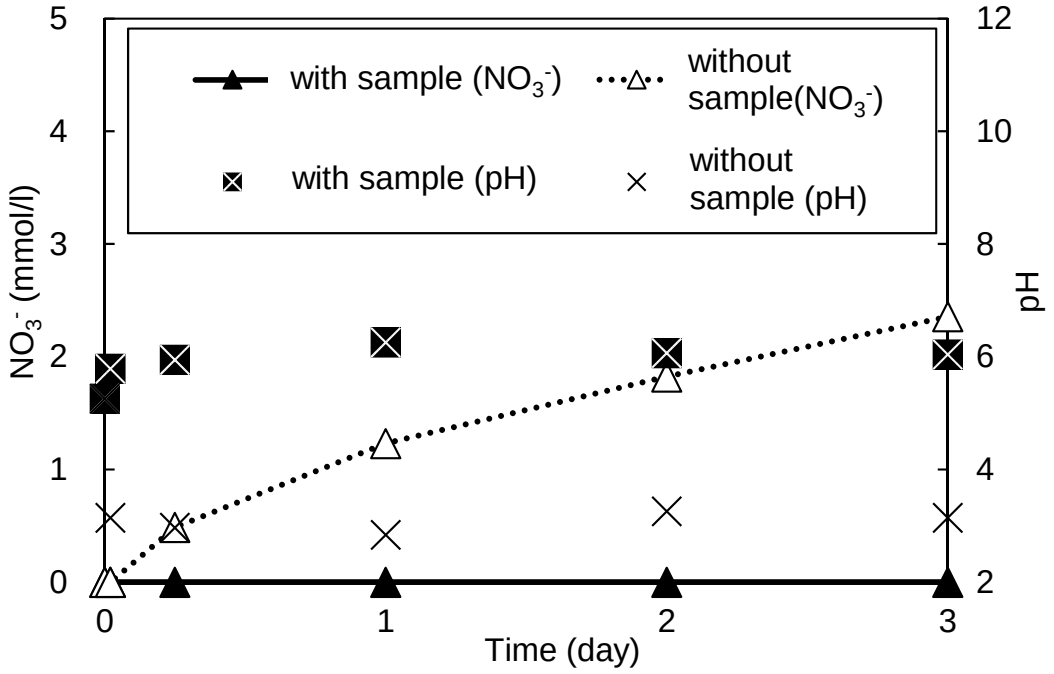

Fig. 2.9 Comparison of NO_3^- concentration and pH under condition SG4 both with and without a core sample.

The oxidation-reduction potential (ORP) of the solution changed from 0.638 V (vs. standard hydrogen electrode; SHE) to 0.305 V (vs. SHE) under condition SG4 immediately after the start and the end of the experiment, respectively. This is considered to have been caused by ion-exchange reactions of minerals and oxidation-reduction reactions between Fe^{2+} and NO_3^- in the solution. In general, leached Fe is precipitated as Fe hydroxide and Fe oxide easily under increasing pH from acidic to neutral or alkali, and lowering of the absolute value of ORP at atmospheric pressure. Referring to the Eh-pH diagram for the typical forms of iron described in the report of Environmental Protection Agency (2003), it is presumed that some of the leached Fe is precipitated as Fe hydroxide on the rock surface because of the decrease in the ORP (0.638 –> 0.305 V (vs. SHE)) and the increase in the pH (5.26 –> 6.32) [43]. In a previous study, Zerai et al. (2006) suggested that siderite ($FeCO_3$) is formed with increasing solution pH, and hence, we considered that siderite was also deposited on a rock surface as one of the Fe compound in this study [44]. Considering the behavior of Ca in this study (Fig. 2.5), the concentration of Ca decreased with increasing pH in condition SG4; thus, it was suspected that calcite or aragonite ($CaCO_3$) was formed [45, 46].

The effect on shale as a cap rock will differ depending on the impurities in exhaust CO_2 from oxyfuel combustion system for injection into an underground aquifer. The effect of NO_2 in oxyfuel combustion CO_2 was investigated by comparing with SO_2 and CO_2 in this study. There was no difference in the changes of pH and mineral dissolution between the results for condition SG3 (36 ppmv NO_2) and those for pure CO_2 in this study; thus, approximately 30 ppmv NO_2 will not affect the dissolution of this cap rock when the CO_2 gas produced by the oxyfuel combustion process is injected into an underground aquifer with this shale as a cap rock.

In contrast, in condition SG4 (318 ppmv NO_2), the pH decreased immediately after the start of the experiment but subsequently increased because Fe^{2+} was leached to work as a reducing agent and undergo oxidation-reduction reactions with NO_3^-. Some of the leached Fe is precipitated on rock surface. Subsequent increases in the pH were not observed, and the amounts of leached ions were similar to those for pure CO_2. Therefore, even if the concentration of NO_2 in oxyfuel combustion CO_2 becomes high, it is expected that dissolution of mineral from rock will be inhibited as a result of the immediate pH rise.

2.4 Conclusions

We prepared impure CO_2 gas to simulate the exhaust gas produced from the oxyfuel combustion process from the Callide pilot plant, which was established to consider the sequestration of CO_2 in underground aquifer, and investigated the effect of NO_2 and SO_2 against cap rock of West Wandoan 1 well Evergreen Formation, which was a candidate site for CO_2 injection in Australia. We used a drill core sample of shale obtained from this site for geochemical experiment and studied the effect of co-injected NO_2 by comparing with the results for pure CO_2 and co-injected SO_2. For CO_2

containing 36 ppmv NO_2, there were no significant differences in ion concentrations and pH changes compared with those of pure CO_2.

For pure CO_2 and CO_2 containing 356 ppmv SO_2, there were differences in the ion concentrations and the pH changes between these experiments and those for CO_2 containing 318 ppmv NO_2. Compared with the results for pure CO_2, the amounts of leached Ca and Fe were higher for the CO_2 containing 318 ppmv NO_2 immediately after the start of the experiment but showed similar values at the end of the experiment. The pH decreased immediately after the start of the experiment but the pH value was higher than that of pure CO_2 or SO_2 (356 ppmv) conditions. Furthermore, the pH increased to 6.32 until the completion of the experiment and the value was the highest observed in all the experiments. We concluded that the pH increase was due to oxidation-reduction reactions between Fe^{2+} and NO_3^-. In addition, we suggested that some of the Fe that had leached into the solution was deposited as Fe-hydroxide or siderite on the surface of shale rock as a result of this pH increase.

Therefore, we conclude that the inclusion of ~30 ppmv NO_2 does not affect the dissolution of the Evergreen Formation shale at 1,026 m of Australian candidate CO_2 reservoir site when exhaust CO_2 produced from the Callide oxyfuel combustion process is injected into an underground aquifer. However, because the pH is increased immediately by oxidation-reduction reactions between Fe^{2+} and NO_3^-, we also concluded that NO_2 does not cause a serious effect on the dissolution of this cap rock depth section due to a pH decrease if the NO_2 concentration in oxyfuel combustion CO_2 temporarily increases. Therefore, for continuous CO_2 injection, we conclude that NO_2 contained in oxyfuel combustion CO_2 will not have a serious effect on this cap rock even if the NO_2 concentration in oxyfuel combustion CO_2 increases for a short period.

Chapter 3

Effect of SO_2 in exhaust gas from an oxyfuel combustion process on materials of CO_2 injection well

3.1 Introduction

CO_2 emission is one of the main causes of global warming. Because of the increase in the global market cost of natural gas and the rapid increase in fossil fuel consumption in developing countries, it has been predicted that the amount of CO_2 gas emitted from coal-fired power stations will increase in the future [18, 19]. Carbon dioxide capture and storage (CCS) is a technique to separate and recover the exhaust CO2 gas from coal-fired power plants and to inject the CO_2 into basalt formations, unmineable coal seams, and deep saline aquifers underground [20]. Some proof-of-concept and actual operation of CO_2 injections have been conducted at several sites such as at the Enhanced Oil Recovery (EOR); however, commercial technology expansion has not made significant progress due to operational costs and environmental assessment problems.

In some clean coal technologies (CCT), oxyfuel combustion technology can increase the concentration of CO_2 in exhaust gas and recover CO_2 with high efficiency. This technology is available for established or new power plants and can reduce the amount of emitted CO_2 by 95% compared with that emitted from a conventional plant. The Callide oxyfuel project in Australia was implemented for demonstration of an oxyfuel combustion system under the cooperation of the Japanese and Australian governments and private funding. By applying the oxyfuel combustion system to existing equipment, a consistent process with recovery and injection of CO_2 was demonstrated. This technology can recover high-concentration CO_2 (>90%) directly with reduced energy consumption because this combustion system runs with pure oxygen prepared by an air separation unit and recycles exhaust CO_2. Unlike the post-combustion systems with air-firing, the consumption of energy for CO_2 recovery is low because desulfurization equipment and CO_2 sequestration equipment are not required [9].

It is known that most of the SO_2 contained in the oxyfuel combustion CO_2 is removed through the CO_2 recovery process, but a small amount of SO_2 is still presented in recovered CO_2 [24, 25]. Moreover, oxyfuel combustion CO_2 may contain 0–30 ppmv SO_2, considering the sequestration of CO_2 in underground aquifers [12]. In light of current development experiences in oil and natural gas, to ensure safety of a boring well for CCS, it is necessary to investigate blowout prevention, cementing for leakage of CO_2, well completion, and explosion protection. Moreover, the prevention of CO_2 leakage is an important issue when supercritical CO_2 is injected into underground aquifers. CO_2 leakage from the neighborhood of an injection well is caused by the deterioration or transformation of cementing seals and by casing steel coming in contact with CO_2 dissolution water [47, 48]. The main cause is neutralization by carbonation of cement by its reaction with calcium hydroxide. Other causes include the dissolution of calcium silicate and the diffusion enrichment of

sulfate and chloride ions due to the dissolution of ettringite or Friedel salt. In general, cement is used to fill in the space between the casing pipe and the side wall of an injection well for preventing CO_2 leakage. Moreover, cement having high durability against CO_2 is used throughout the contact area with CO_2 dissolution water. Similarly, a CO_2-resistant casing pipe is used in contact areas with CO_2 dissolution water for ensuring long-term safety. Neat cement (G grade in API), J55, and K55 are generally used as the well materials [16].

Many experiments and numerical modelings of CO_2 injection well completion have been conducted at an actual injection site and in the laboratory. Kunieda et al. studied the long-term reaction between supercritical CO_2 and G-class cement under conditions of an underground reservoir and discovered that the sealing ability of cement decreased in a month due to an increase in porosity and the dissolution of the cement contacting CO_2 dissolution water. Azuma et al. studied the long-term corrosion behavior of casing steel under a CO_2 reservoir and described that the precipitation of $FeCO_3$ due to the reaction between Fe^{2+} dissolved from casing steel and CO_2 gas protected the steel and reduced long-term corrosion [11, 49].

However, to the best of our knowledge, there have been no studies that investigated the safety of CO_2 injection well materials using CO_2 gas containing impurities such as SO_2. The pH in the formation water decreases by CO_2 injection as shown in Eq. 7. SO_2 could cause higher acidification than CO_2 gas because it is dissolved in the formation water and form hydrogen sulfite ions easily. Moreover, there is concern SO_2 can cause more corrosion of the cement than pure CO_2 gas because it can enter pores and promote neutralization of the cement material. Additionally, the promotion of the corrosion of casing steel is worrisome because Fe is dissolved by the decreased pH in the formation water.

$$CO_2 + H_2O \rightarrow H^+ + HCO_3^- \quad (pK_a = 6.35) \tag{7}$$

$$SO_2 + H_2O \rightarrow H^+ + HSO_3^- \quad (pK_a = 1.85) \tag{8}$$

In this study, geochemical experiments and microscopic observations were conducted to clarify the effect of SO_2 contained in CO_2 on the injection well materials. Specifically, we studied the effect of ~30ppmv SO_2 on CO_2-resistant cement that has low reactivity with CO_2 and J55 casing steel that is used for the oil well material for EOR technology. In addition, the behavior tendency near the CO_2 injection well in a reservoir was examined.

3.2 Experimental apparatus and procedure

3.2.1 Materials

A CO_2-resistant cement (CorrosaCem NP, Halliburton) and J55 casing steel were used in this study. The CO_2-resistant cement was developed as a special cement for use as oil well cement that

has high durability against CO_2. In addition, general Portland cement was prepared for comparison to the results of CO_2-resistant cement. Chemical components of CorrosaCem NP cement, Portland cement and J55 measured by fluorescent X-ray analysis are shown in Table 3.1. The CO_2-resistant cement has less calcium content than Portland cement, thus reducing the carbonation of calcium that causes cement corrosion. XRD patterns measured by X-ray diffractometry (XRD-6000, Shimadzu) and microphotographs of the CO_2-resistant cement are shown in Figs. 3.1 and 3.2, respectively. The CO_2-resistant cement has gibbsite, nordstrandite, mayenite and katoite, while Portland cement has mainly alite, blite and portlandite and small amounts of ettringite, tobermorite gel and monosulfate hydrate, as seen in Figs. 3.3 and 3.4.

Na-HCO_3-Cl solution was used to simulate formation water in Surat basin, Australia, which was a candidate site for a CO_2 injection reservoir in the Callide oxyfuel project [17]. This solution was prepared by mixing 60 mmol/L $NaHCO_3$ solution and 30 mmol/L NaCl solution. The initial pH of the solution was 8.8 and the initial concentrations were 90 mmol/L Na^+, 60 mmol/L HCO_3^-, and 30 mmol/L Cl^- respectively. A mixed gas that simulated oxyfuel combustion CO_2 (simulated gas), high-concentration CO_2 gas (pure CO_2), and N_2 gas were prepared to facilitate studying the effects of impurities in oxyfuel combustion CO_2 (Table 3.2).

Table 3.1 Chemical components and water-cement ratio of samples.

Weight %	SiO_2	Al_2O_3	*Fe_2O_3	MgO	CaO	Na_2O	P_2O_5	Others	*LOI
CO_2 resistant cement	19.0	32.9	8.40	0.41	11.7	1.72	2.63	3.29	20.0
Portland cement	17.2	4.66	2.61	0.85	48.0	0.18	0.18	4.82	21.5

Casing steel (J55)	Fe	Si	Mn	P	S
	< 98.5%	0.39%	1.36%	> 0.008%	0.002%

*Fe_2O_3: Total Fe *LOI: Loss on ignition

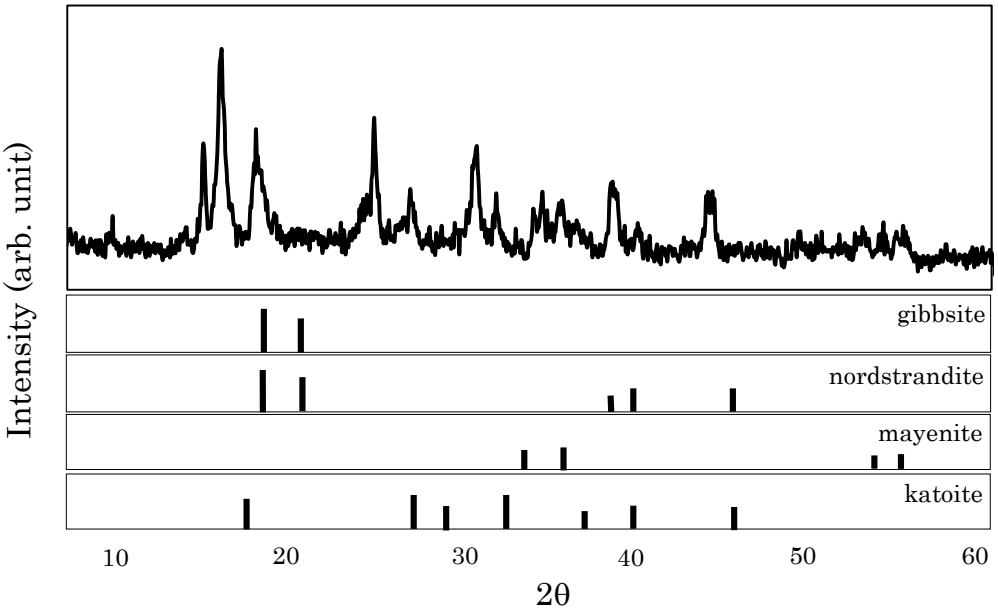

Fig. 3.1 XRD pattern of the CO_2-resistant cement.

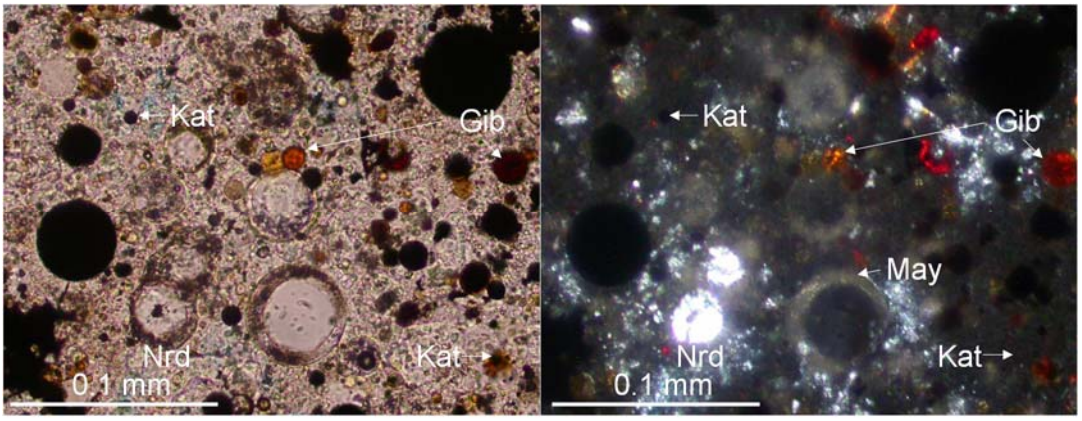

Fig. 3.2 Microphotographs of the CO_2-resistant cement.

(left: plane-polarized light, right: crossed polars), Abbreviations: Gib: Gibbsite; Nrd: Nordstrandite; May: mayenite; and Kat: Katoite

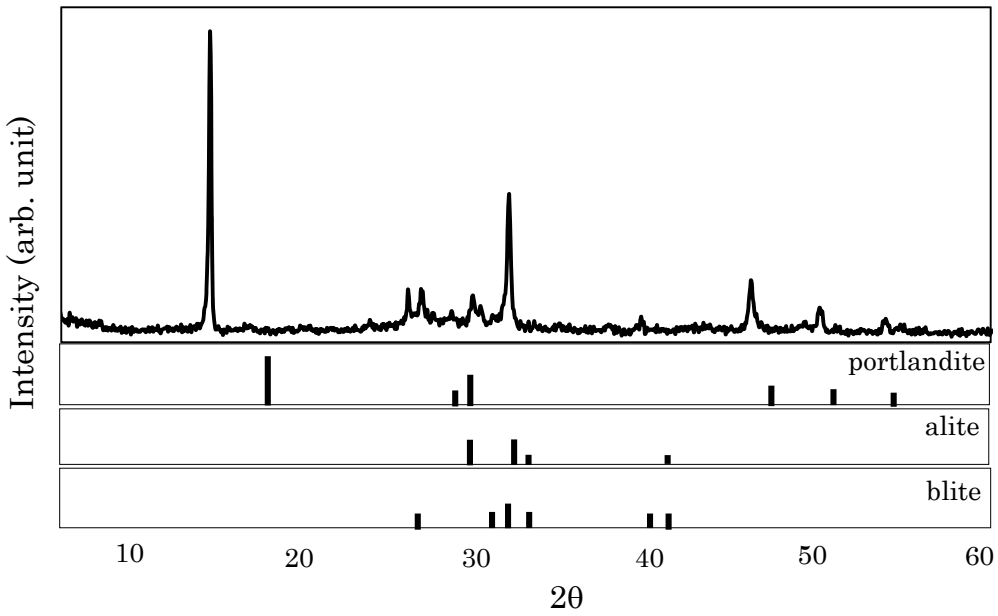

Fig. 3.3 XRD patterns of the Portland cement.

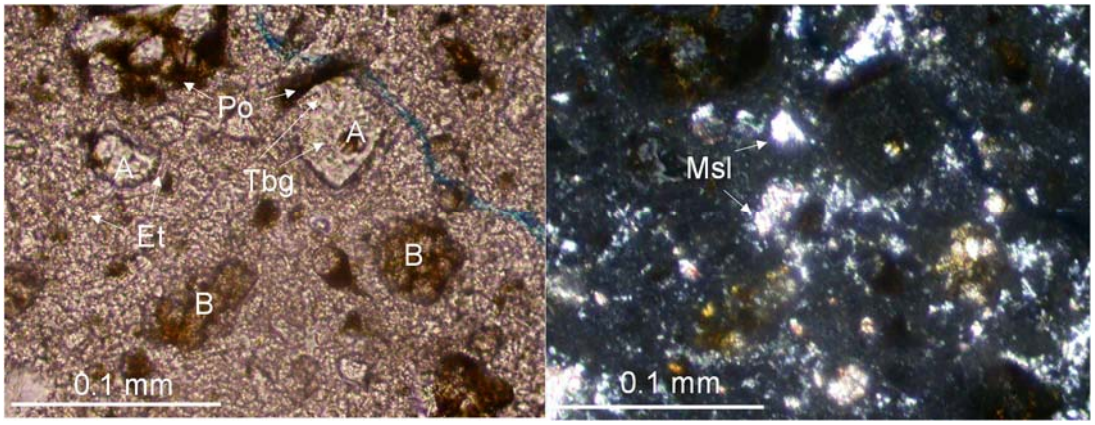

Fig. 3.4 Microphotographs of the Portland cement.

(left: plane-polarized light; right: crossed polars), Abbreviations: A: Alite; B: Blite; Po: Portlandite; Et: Ettringite; Tbg: Tobermorite gel; and Msl: Monosulfate hydrate

Table 3.2 Experimental gas compositions

	Simulated gas	CO_2 gas	N_2 gas
CO_2	Balance	>99.995%	
N_2	2.20%		>99.999%
SO_2	33.8 ppmv		

3.2.2 Experimental methods

3.2.2.1 Cement

In this study, a reaction apparatus was prepared to correspond to high pressure and temperature. The reactor was attached to a syringe-type pump for the injection of high-pressure gas to maintain constant pressure for the duration of the experiment as shown in Fig. 3.5 (a). The experiment using cement samples was conducted with a square cement sample (about 30 g) and solution (about 300 mL) in the vessel for 14 days. The solution was constantly stirred at 420 rpm and the inner pressure and temperature (measured by sensors) were recorded by a data logger during the experiment. The solution was sampled 9 times through a 0.2 μm filter. The condition in the vessel was maintained at 60 °C and 8.5 MPa to simulate the depth of a 1,000 m reservoir. Chemical compositions of the solution were analyzed with ion chromatography and inductively coupled plasma emission spectrophotometry (ICP-AES). Cement samples were observed by macroscopy, polarization microscopy and SEM before and after the experiment. In addition, identification and elemental analysis of the precipitated crystals were analyzed by X-ray diffraction and energy dispersive X-ray spectrometry (SEM-EDS).

3.2.2.2 J55 casing steel

J55 was cut into a shape of 3.4 × 3.4 × 1 mm and half of the area was coated with Au (45 μm) to prepare a reference area (no reaction area). The J55 sample was set in another small reaction cell (20 cm square) and the reaction was conducted by sending the gas dissolved solution over it as shown in Fig. 3.5 (b). The condition of this reaction cell was maintained at 60 °C and 8.5 MPa and the experiment time was about 17 hours. The change in weight of the J55 sample was measured and analyzed by macroscopy and vertical scanning interference microscopy (VSI, MM5500, Ryoka Systems, Inc.) after the experiment.

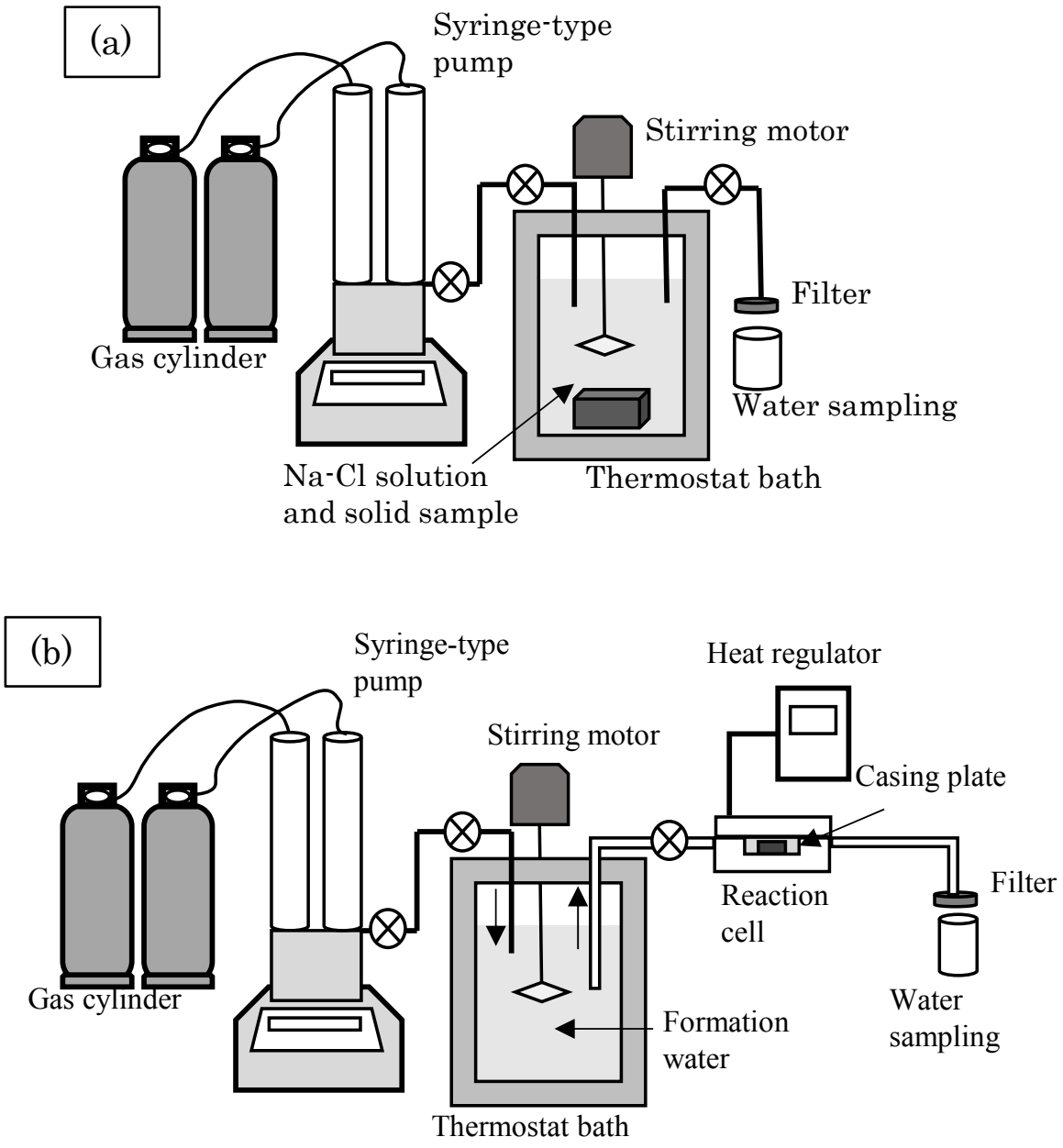

Fig. 3.5 Experimental apparatus. (a) Cements, (b) J55 casing steel

3.3 Results and Discussion

3.3.1 Cements

The change of pH under each gas condition in the CO_2-resistant cement is shown in Fig. 3.6. The pH decreased to about 6.7 after the start of the experiment and then maintained a constant value under simulated gas and pure CO_2 gas conditions. On the other hand, pH increased after the start of the experiment and reached 11.8 after 14 days under N_2 gas. The decrease of pH under simulated gas and pure CO_2 gas conditions was due to neutralization by the dissolution of CO_2 in the solution, but the effect of a small amount of SO_2 was not confirmed. The CO_2-resistant cement contained gibbsite, nordstrandite and katoite [$Ca_3Al_{12}(OH)_{12}$]. Gibbsite and nordstrandite [$Al(OH)_3$] had poor solubility (K_{sp} = 2.00 × 10^{-33}) [50]. Ca^{2+} and $Al(OH)_4^-$ were dissolved from katoite after the start of the experiment as shown in Eq. 9. Under simulated gas and pure CO_2 gas conditions, the solution became weak neutral because CO_2 or SO_2 was dissolved and the reaction between CO_2 and H_2O occurred to give constant HCO_3^- in the weak alkaline range after the start of the experiment as shown in Eqs. 7, 8, and 10. Thus, the reaction shown in Eq. occurred under the pH range of 5-7 because aluminum ion formed $Al(OH)_3$ stably in the solution [51]. Similarly, under the N_2 gas condition, the reaction shown in Eq. 9 occurred continuously throughout the experiment. The concentration of Al was not measurable under simulated gas and pure CO_2 gas conditions but increased throughout the experiment under N_2 gas based on the change in Al concentration as shown in Fig. 3.7. Thus, the increase in pH was due to the increase in concentration of OH^- in the solution as shown in Eq. 9.

$$Ca_3Al_2(OH)_{12} \rightarrow 3Ca^{2+} + 2Al(OH)_4^- + 4OH^- \quad (9)$$

$$CO_2 + OH^- \rightarrow HCO_3^- \quad (10)$$

$$Al(OH)_4^- + H^+ \rightarrow Al(OH)_3 + H_2O \quad (11)$$

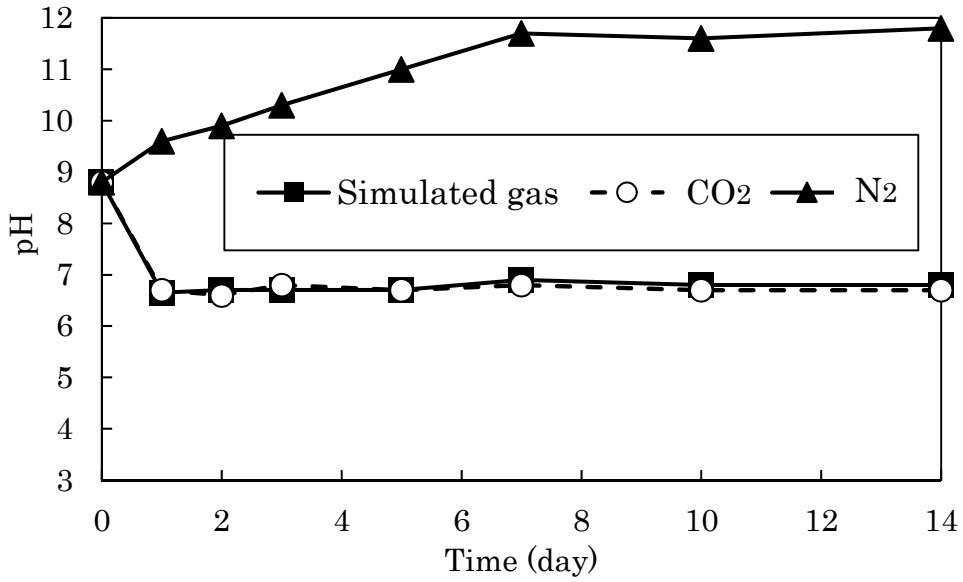

Fig. 3.6 Change of pH in the solution with the CO_2-resistant cement.

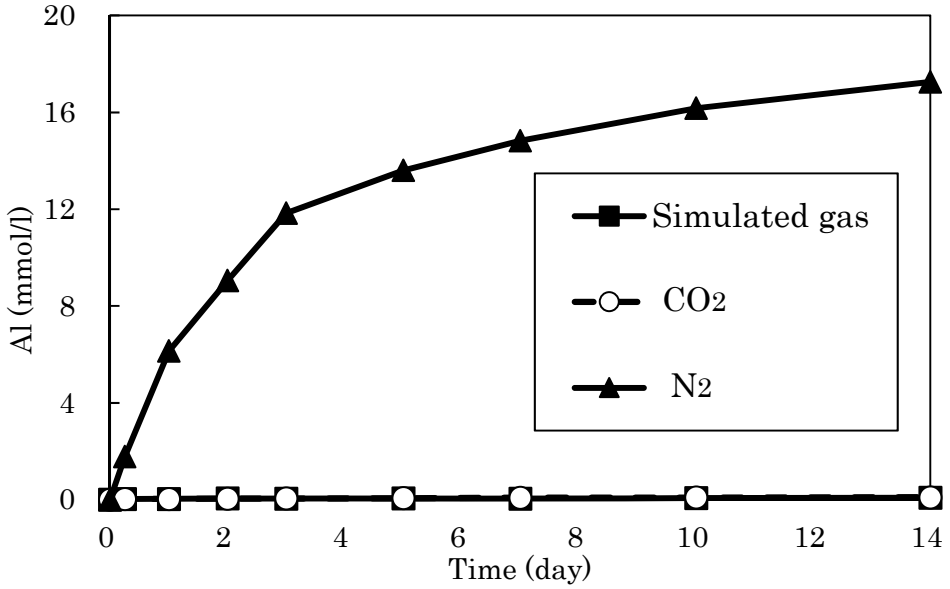

Fig. 3.7 Change of Al concentration in the solution with the CO_2-resistant cement.

The observation and analysis results of CO_2-resistant cement after the experiment are shown below. The microphotographs of the thin samples using a polarizing microscope (one nicol) are focused on the alteration area under simulated gas and N_2 gas conditions and are shown in Fig. 3.8. Moving to the right in the figure is the direction toward the center of sample and the observation range is 5 mm from the surface. Under simulated gas and pure CO_2 gas conditions, an area subjected to carbonation (I) and an undegraded area (II) were confirmed. Under the N_2 gas condition, it was found that the range of area (I) was a little larger than those in the simulated gas and pure CO_2 gas conditions. In addition to the (I) and (II) areas, a degraded area with no precipitation of carbonate (III) was confirmed under the N_2 gas condition.

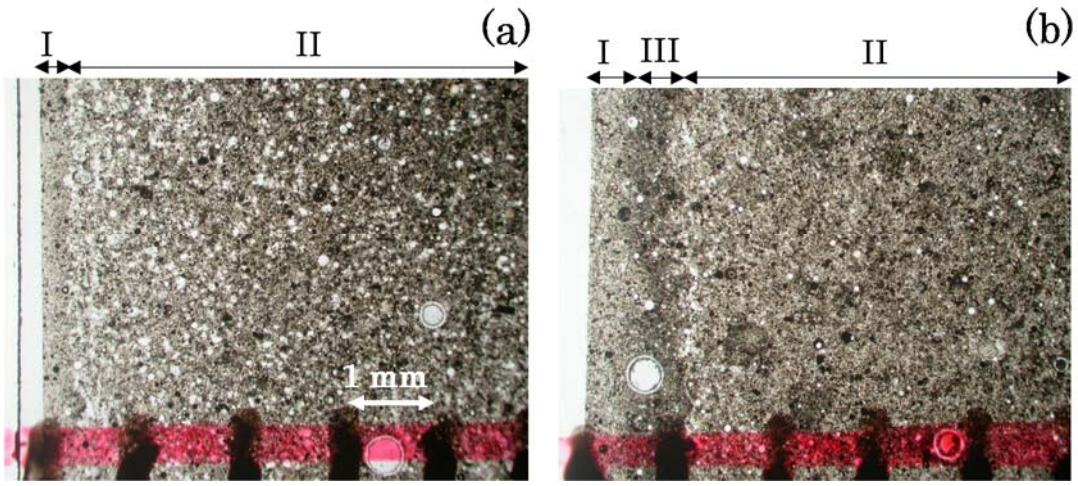

Fig. 3.8 Alteration area of thin sample of CO_2-resistant cement under simulated gas (a) and N_2 gas (b) conditions.

Fig. 3.9 shows that katoite disappeared and calcite was generated after the experiment under each gas condition by analyzing an area 2 mm from the surface of the sample with XRD. The amount of calcite generated under the N_2 gas condition was the most compared to the other gases. Generation of calcite under simulated gas and CO_2 gas conditions was due to the reaction between Ca^{2+} that was dissolved from katoite (Eq. 9) and HCO_3^- after the start of the experiment as shown in Eq. 12. However, it was assumed that some of the generated calcite was dissolved when there was an excess of CO_2 in the solution compared with the amount of calcite as shown in Eq. 13. Moreover, the concentration of Ca under simulated gas condition was a little lower than that of pure CO_2 gas condition. This cause was assumed due to the precipitation of $CaSO_3$ with the reaction between SO_2 and $CaCO_3$ as shown in Eq. 14. Under the N_2 gas condition, calcite was generated by the reaction of Eq. 12 after the start of the experiment and was also generated by the reaction of Eq. 15 because CO_2 was stable as a form of CO_3^{2-} in the solution at pH > 10. Almost all of the Ca dissolved from katoite was precipitated as calcite as shown in Fig. 3.10. Therefore, it was considered that the carbonation reaction of CO_2-resistant cement under simulated gas and pure CO_2 gas conditions was lower than that under the N_2 gas condition.

$$Ca^{2+} + HCO_3^- + OH^- \rightarrow CaCO_3 + H_2O \quad (12)$$

$$CaCO_3 + CO_2 + H_2O \rightarrow Ca^{2+} + 2HCO_3^- \quad (13)$$

$$CaCO_3 + SO_2 \rightarrow CaSO_3 + CO_2 \quad (14)$$

$$Ca^{2+} + CO_3^{2-} \rightarrow CaCO_3 \quad (15)$$

There was not a remarkable difference in the change of pH and the degree of carbonation between the results under simulated gas and pure CO_2 gas conditions and that under the N_2 gas condition. Therefore, it was concluded that 33.8 ppmv SO_2 does not have serious impacts on the CO_2-resistant cement.

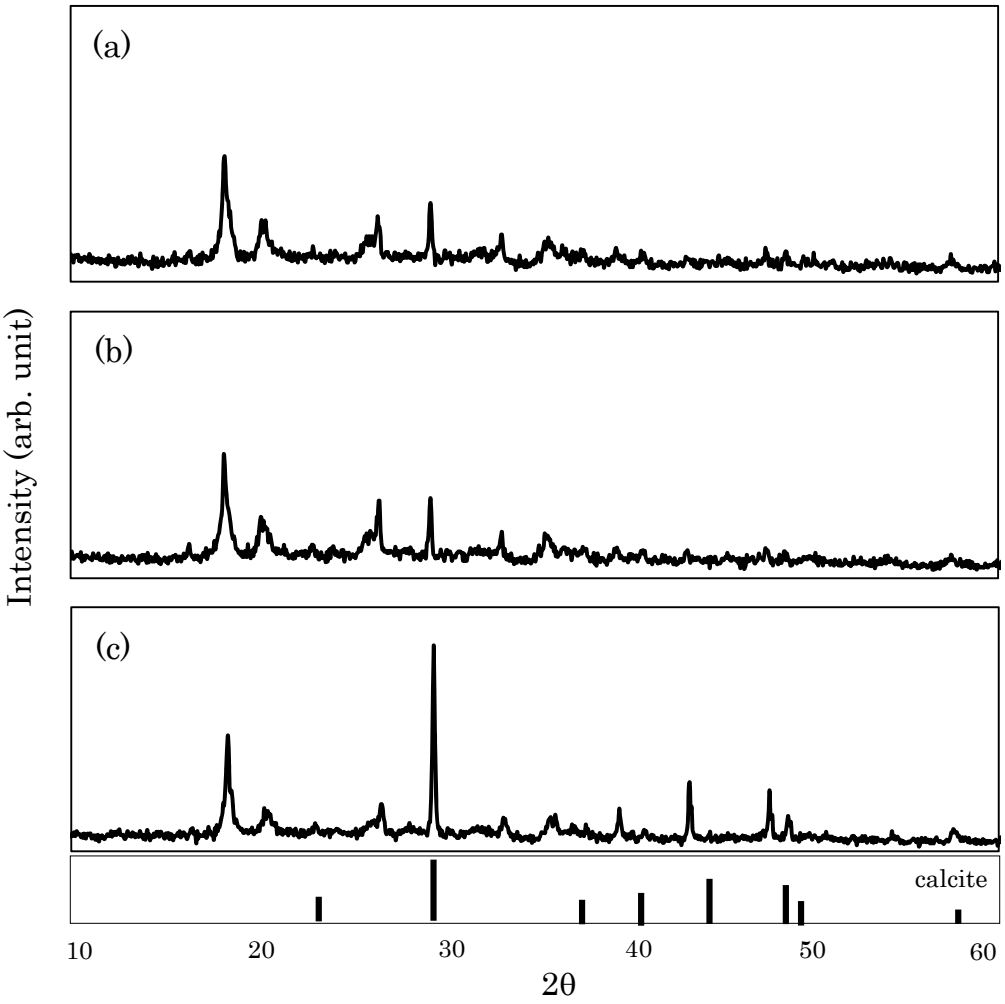

Fig. 3.9 XRD patterns of the alteration area of the CO_2-resistant cement.
(a: simulated gas; b: pure CO_2 gas; c: N_2 gas)

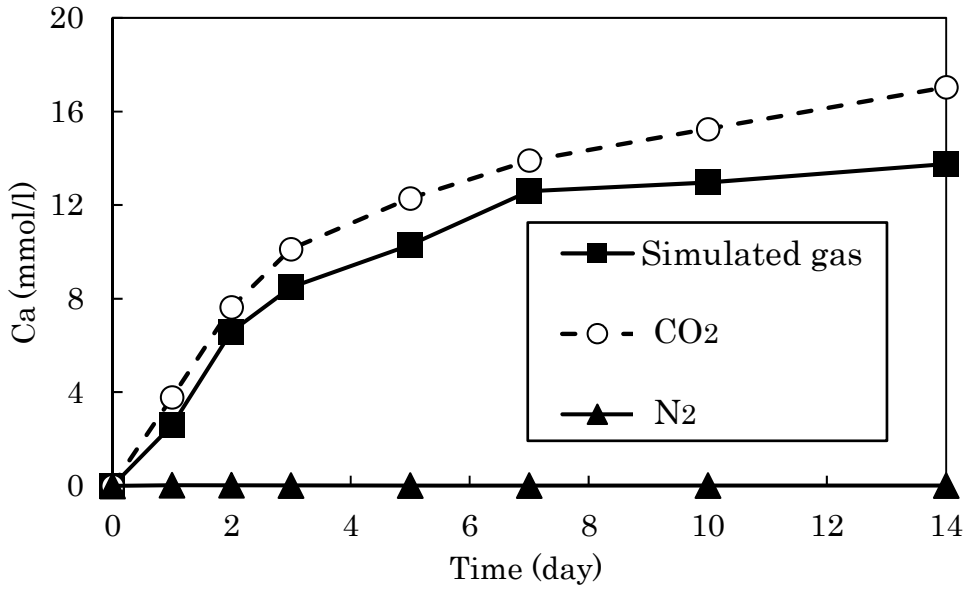

Fig. 3.10 Change of Ca concentration in the solution with the CO_2-resistant cement.

The results of Portland cement are shown below in order to compare the reaction behavior to the CO_2-resistant cement. The change of pH under each gas condition is shown in Fig. 3.11. Under simulated gas and pure CO_2 gas conditions, the pH was a similar value, which indicated the effect of SO_2 to be very low. Under the N_2 gas condition, the pH also did not change from the initial value; thus, it was considered that the dissolution of katoite caused the increase in pH in the experiment of the CO_2-resistant cement.

The observation and analysis results of the Portland cement sample after the experiment are shown below. The microphotographs of the thin samples using a polarizing microscope (one nicol) are focused on the alteration area under simulated gas and N_2 gas conditions and are shown in Fig. 3.12. Under simulated gas and pure CO_2 gas conditions, an area subjected to carbonation (I), an undegraded area (II), and an area with disappearance of monosulfate hydrate (III) were confirmed. In addition to observing the surface area in detail, an area with adhesion of fine calcite (< 0.01 mm) with column crystal (IV) and an area with permutations to the fine calcite (V) were confirmed. Under the N_2 gas condition, almost all of the thin sample was undegraded, but precipitation of fine calcite was confirmed on the surface. Fig. 3.13 shows the XRD patterns of the alteration area under each gas condition. Under simulated gas and pure CO_2 gas conditions, mainly alite, blite, and portlandite were contained in the Portland cement, and calcite and a small amount of vaterite were generated. Under the N_2 gas condition, a small amount of calcite was generated.

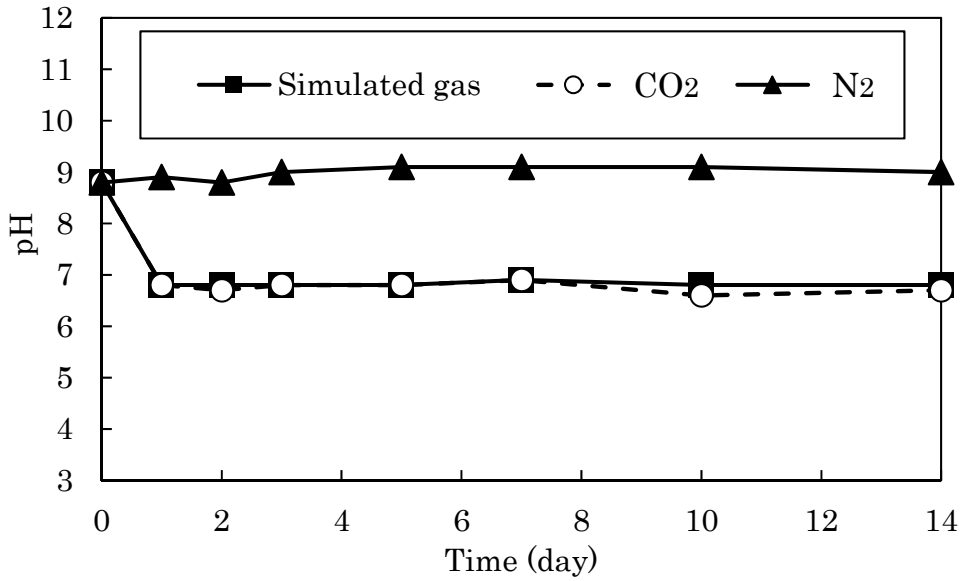

Fig. 3.11 Change of pH in the solution with the Portland cement.

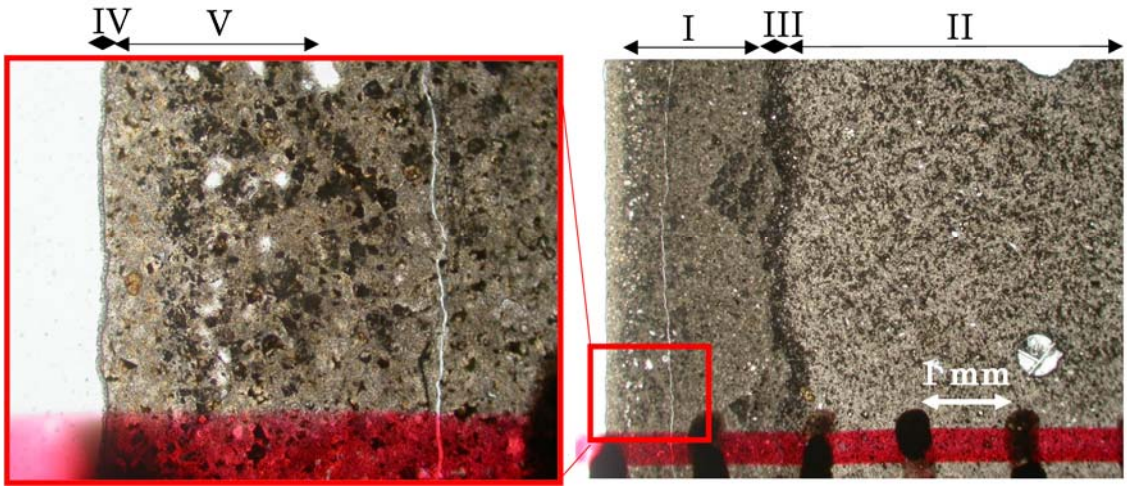

Fig. 3.12 Alteration area of thin sample of the Portland cement under simulated gas.

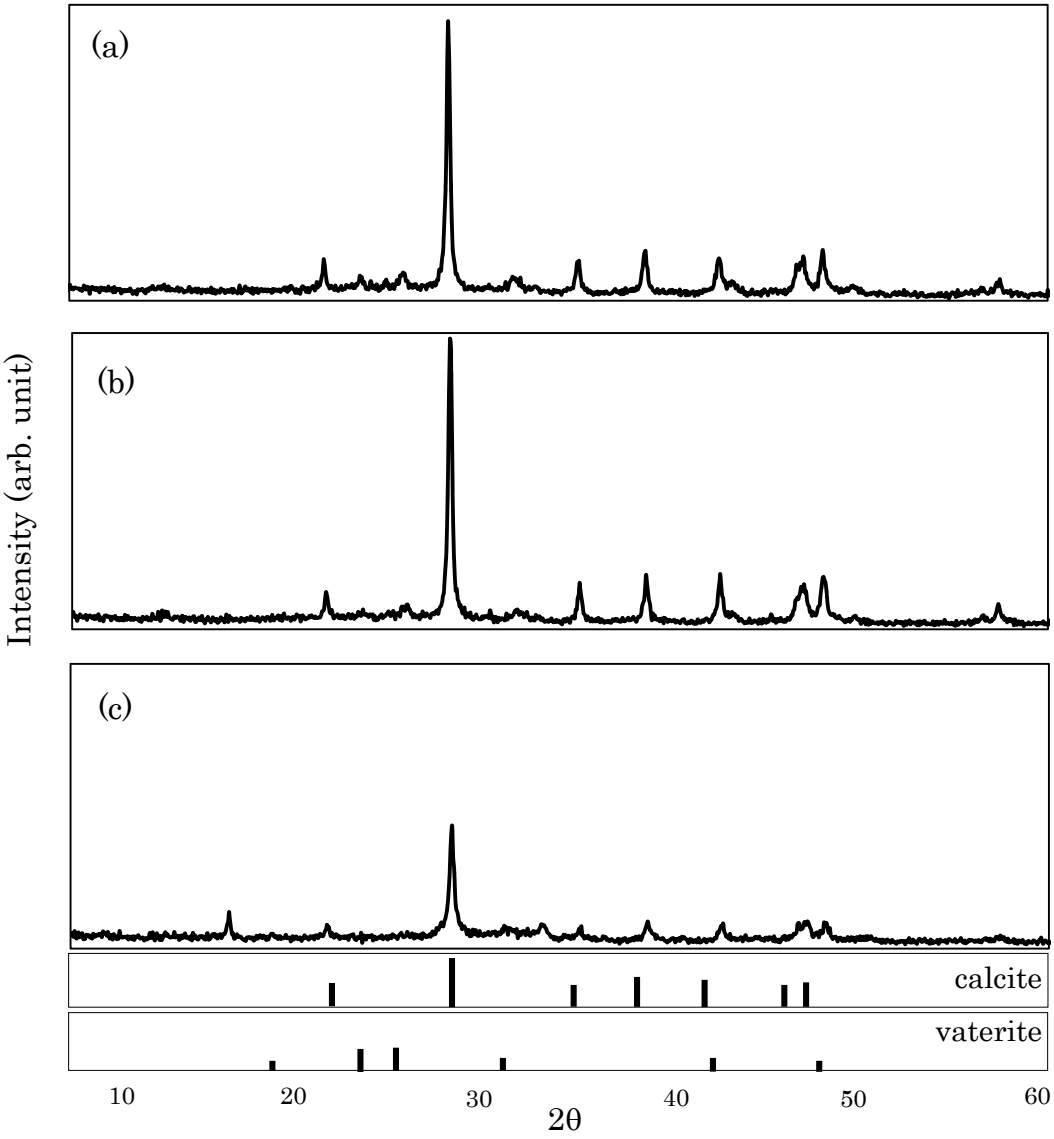

Fig. 3.13 XRD patterns of alteration area on the Portland cement.

(a: Simulated gas; b: CO_2 gas; c: N_2 gas)

The reaction process between Portland cement and CO_2 dissolution water has been described in a previous study. The degradation of Portland cement with CO_2 occurs by carbonation and leaching reactions. Calcium carbonate ($CaCO_3$) is generated by the reaction between calcium hydroxide [$Ca(OH)_2$] generated in the Portland cement and CO_2 as shown in Eq. 16. The dissolution of $CaCO_3$ occurs due to a leaching reaction as shown in Eq. 17 when there is an excess of CO_2 in the solution compared with the amount of $CaCO_3$ and then reprecipitation of $CaCO_3$ occurs by the reaction between $Ca(HCO_3)_2$ and $Ca(OH)_2$ as shown in Eq. 18. In addition, $CaCO_3$ is also generated by the reaction between Ca^{2+} dissolved from the portlandite that was present or was produced by the hydration reaction of alite or blite and HCO_3^- in the solution [52, 53]. Under simulated gas and pure CO_2 gas conditions, it was assumed that $CaCO_3$ was generated continuously because protons were supplied by the dissolution of the acid gases under simulated gas and pure CO_2 gas conditions. Under the N_2 gas condition, $CaCO_3$ was generated by the reaction between Ca^{2+} released from the portlandite and CO_3^{2-} in the solution after the start of the experiment as shown in Eq. 15, but it was considered that the amount of $CaCO_3$ was less than that under simulated gas and pure CO_2 gas conditions because calcium hydroxide was more stable in the alkaline environment. Therefore, it was clarified that the alteration was due to the carbonation under simulated gas and pure CO_2 gas conditions. Moreover, there was no remarkable difference in the degree of carbonation between simulated gas and pure CO_2 gas conditions, and thus the effect of SO_2 contained in simulated gas was not confirmed.

$$Ca(OH)_2 + H^+ + HCO_3^- \rightarrow CaCO_3 + 2H_2O \quad (16)$$

$$CaCO_3 + H^+ + HCO_3^- \rightarrow Ca(HCO_3)_2 \quad (17)$$

$$Ca(HCO_3)_2 + Ca(OH)_2 \rightarrow 2CaCO_3 + 2H_2O \quad (18)$$

It is known from previous studies that some of the reaction zones were formed by the reaction between the cement materials and CO_2 dissolution formation water. [54, 55]. This reaction is separated roughly into four zones. Area 1 is where diffusion of Ca^{2+} due to the dissolution of portlandite and dissolution of generated calcite occurs. In Area 2, the precipitation of calcite due to the reaction between Ca^{2+} released from the portlandite and HCO_3^- or CO_3^{2-} in formation water occurs. A similar reaction as in Area 2 occurs in Area 3, but the porosity decreases. Finally, in Area 4, the initial dissolution of the portlandite occurs. Area 1 was not confirmed in the microscopic observation of the CO_2-resistant cement and the Portland cement. It was considered that the reaction of Area 2 occurred on the contact surface between the solution and cement because HCO_3^- was initially contained in the solution. Portland cement was covered with carbonation areas such as I, IV, and V in Fig. 3.11. On the other hand, the carbonation area did not form layers in the CO_2-resistant cement. It was considered that the amount of Ca^{2+} released from katoite in the CO_2-resistant cement was lower

than that from portlandite in the Portland cement and the carbonation reaction was reduced under simulated gas and pure CO_2 gas conditions.

There was no remarkable difference in the change of pH and the degree of carbonation in the CO_2-resistant cement, compared to the results under oxyfuel combustion CO_2 containing about 30 ppmv SO_2 with pure CO_2 gas. Therefore, it was concluded that CO_2 containing SO_2 that is exhausted from the oxyfuel combustion process could be injected using the injection well design generally used for the injection of supercritical CO_2.

3.3.2 J55 casing steel

Characterization of the deposited mineral on the surface was conducted by macroscopy, SEM observation, and X-ray diffraction after the experiments under each gas condition. The photographs of J55 samples under simulated gas and pure CO_2 gas conditions are shown in Fig. 3.14. SEM images and XRD patterns of two areas, (I) with Au coating and (II) without Au coating, after simulated gas and pure CO_2 gas conditions are shown in Figs. 3.15 and 3.16, respectively. Some white deposits were confirmed on both the (I) and (II) areas under the simulated gas condition and this deposit was found to be siderite. Similarly, siderite was deposited on the surface under the CO_2 gas condition.

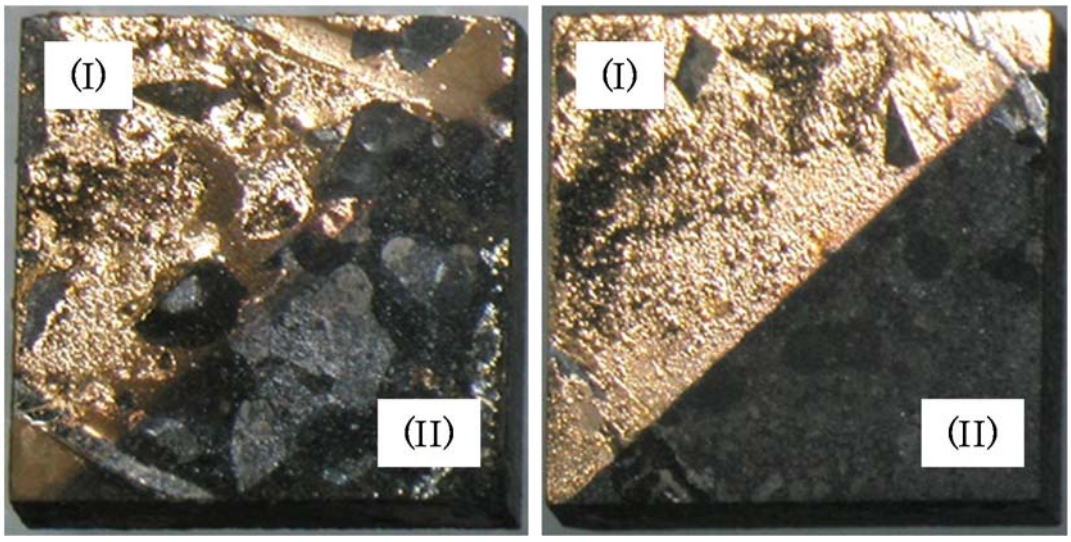

Fig. 3.14 Photographs of J55 samples. (left: simulated gas; right: CO_2 gas)
(I) with Au coating, (II) without Au coating

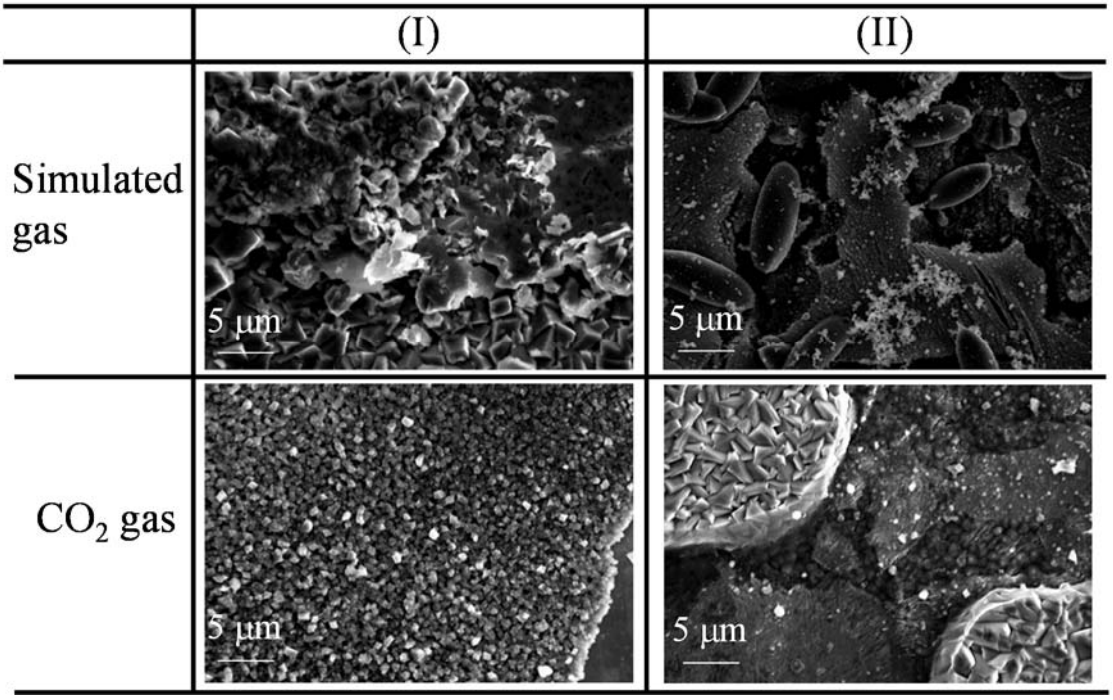

Fig. 3.15 SEM images of two areas on the surface.

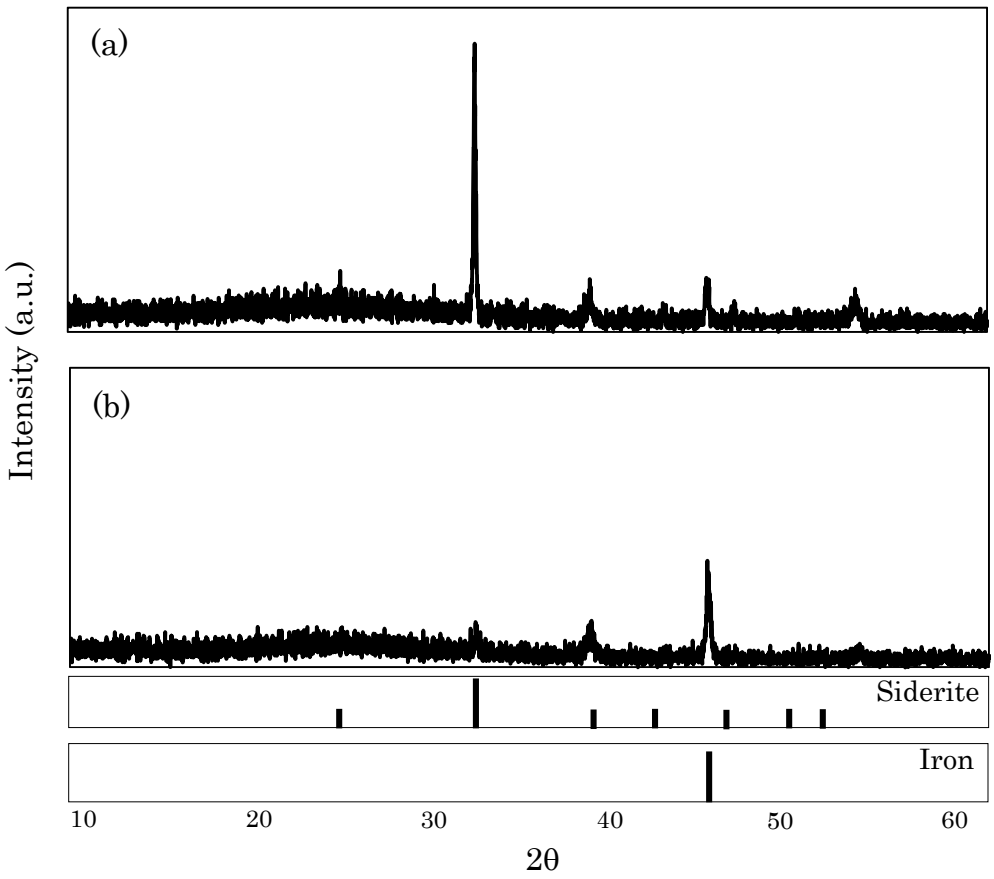

Fig. 3.16 XRD patterns of the deposit on the surface. (a: simulated gas; b: CO_2 gas)

In a previous study with conditions similar to those of this experiment, it was found that siderite was precipitated by the reaction between Fe^{2+} due to the dissolution of J55 and HCO_3^- in the solution under high-concentration CO_2 gas [11]. Siderite could be precipitated in this experiment because it was stable in neutral or alkaline anaerobic conditions [56]. The XRD peaks of siderite under the simulated gas condition were higher than those under pure CO_2 gas and it was presumed that this was due to the effect of SO_2. Compared with the results under pure CO_2 gas, SO_2 supplies more protons to the solution as shown in Eq. 8 and the dissolution of iron was promoted under anaerobic conditions as shown in Eq. 19 [57]. Thus, it was presumed that the amount of precipitation of siderite as shown in Eq. 20 under the simulated gas condition was more than that under the pure CO_2 gas condition.

$$Fe + 2H^+ \rightarrow Fe^{2+} + H_2 \quad (19)$$

$$Fe^{2+} + HCO_3^- \rightarrow FeCO_3 + H^+ \quad (20)$$

The volume and area higher and lower than the reference surface (with Au coating) were measured by three-dimensional data using VSI analysis and the average height was calculated by the volume divided by the area (Table 3.3). The corrosion depth was equal to the average height lower than the reference surface and the deposition height was calculated by adding the average height higher than the reference area and the corrosion depth, assuming the deposition occurred after the corrosion of the sample. Both corrosion and deposition reactions occurred under simulated gas and pure CO_2 gas conditions. Moreover, the corrosion depth and deposition height under simulated gas were higher than that under the pure CO_2 gas condition after 18 h. Thus, it was found that Fe dissolved more but then more deposition of siderite occurred under the simulated gas condition. Therefore, it was suggested that the corrosion of casing steel was promoted after the start of the injection but then it was reduced when the corrosion film of siderite was deposited on the surface near the contact area between the injection well and formation water when CO_2 containing SO_2 from the oxyfuel combustion process was injected into underground aquifers.

Table 3.3 Measurement data using VSI analysis and pH of the solution.

Gas	Time (h)	Corrosion depth (10^{-3} mm)	Deposition height (10^{-3} mm)	pH
Simulated gas	17.9	1.28	5.25	6.6
CO_2	18.3	0.40	2.15	6.7

3.4 Conclusion

We investigated the effect of SO_2 contained in CO_2 on the dissolution and corrosion of well materials that are used for supercritical CO_2 injection when CO_2 recovered from the oxyfuel combustion process is injected into an underground aquifer. CO_2-resistant cement and J55 casing steel were used as experimental samples and a mixed gas that simulated oxyfuel combustion CO_2, high-concentration CO_2 gas, and N_2 gas were used as experimental gases. This study was conducted at 8.5 MPa and 60 °C to simulate underground reservoir conditions, and the analyses of the solution and the samples were compared under each gas condition.

Carbonation occurred on the surface of the CO_2-resistant cement under each gas condition and it was suggested that calcite was deposited by the dissolution of katoite by the change of pH under the N_2 gas condition. There was no remarkable difference in the change of pH and the degree of carbonation in the samples with CO_2 containing SO_2 gas and with pure CO_2 gas and thus it was determined that the effect of a small amount of SO_2 contained in CO_2 could be ignored for the most part. Therefore, we concluded that CO_2 recovered from the oxyfuel combustion process could be injected using the injection well design for pure supercritical CO_2.

The corrosion of casing steel occurred under CO_2 containing SO_2 and pure CO_2 gas, but more corrosion occurred under CO_2 containing SO_2 gas. However, dissolved Fe^{2+} deposited more siderite on the surface under the CO_2 containing SO_2 gas condition. Therefore, we suggest that the corrosion of casing steel will be reduced because it is promoted after the start of injection, but siderite will be deposited on the surface when oxyfuel combustion CO_2 is injected into an underground aquifer. In the future, we hope that long-term investigations of siderite as a corrosion film and the effect of SO_2 concentration will be conducted.

Chapter 4

Ultrasound irradiation for desorption of carbon dioxide gas from aqueous solutions of monoethanolamine

4.1 Introduction

In recent years, global warming has become a major problem, and reduction of greenhouse gas emissions has become an important issue. Of all greenhouse gases released to the atmosphere, approximately 95% is carbon dioxide (CO_2). Accordingly, thermal power plants are attempting to attain zero CO_2 emissions. Carbon capture and storage (CCS) involves the following processes: capturing CO_2 from flue gases, transporting it to a storage site and depositing it into an aquifer. Thus, CCS is expected to be a useful technology for reducing CO_2 emissions [14, 20, 58-62].

To capture CO_2 from flue gas, many different methods are used: chemical absorption with absorbents such as amines, physical absorption with absorbents such as polyethylene glycol, and membrane absorption [63-67]. Chemical absorption using an alkanolamine is a popular technology for capturing CO_2. Several studies using aqueous alkanolamine as a chemical absorber, which include model simulations of the absorption process, have been conducted for CO_2 absorption; the general reaction produces carbamate ion ($RNHCO_2^-$) [68, 69].

Aqueous monoethanolamine (MEA) has also been used as an absorbent in CO_2 removal processes because MEA offers several advantages over other alkanolamines; those advantages include higher reactivity, lower cost of solvent, lower molecular weight and higher absorption capacity on a weight basis. The absorption capacity of MEA depends on ambient temperature, pressure and solvent concentration [70-76].

However, there are some issues in using MEA for capturing CO_2. Capturing and separating costs are 60%–70% of the total cost; thus, reducing these costs is important [77]. Furthermore, heating (regeneration process) MEA to release CO_2 consumes large amounts of energy. Thus, we seek a method for removing CO_2 from MEA with low energy consumption. In this study, we focused on a degasifying process that can separate CO_2 from MEA at low temperatures.

Degasification is one of the methods used to release dissolved gases from a solution [78]. In particular, degasification using ultrasound irradiation is a well-known approach [79]. Thus, we focus on degasification using ultrasound irradiation to remove CO_2 from an MEA solution. The flue gases comprise 12.5%–12.8% CO_2, 6.2% H_2O, 4.4% O_2 and 76%–77% N_2 [80]. Nitrogen is also separated from the gases; therefore, we considered the effective utilization of N_2 for CO_2 desorption [81]. Use of ultrasound irradiation for CO_2 desorption from an MEA solution has not yet been reported. In this study, we investigated the combination of ultrasound irradiation and N_2 gas flow for desorption of CO_2 from MEA solution.

4.2 Experimental Method

The experimental apparatus is shown in Fig. 4.1. Ultrasound irradiation was conducted in a cycloid-type thermostat bath (Thermo, ELECTRON) to control the solution temperature during the CO_2 absorption and desorption experiments. MEA solutions were irradiated from the bottom of a flat-bottom flask. To compare the effects of ultrasound irradiation with those of stirring, selected solutions were stirred at speeds of 500, 1000 and 1500 rpm. Ultrasound irradiation was performed using an ultrasound generator (TA-4021, Kaijo) and submersible transducers (28 kHz) [82-85]. The output of this device was adjusted to 200 W. The ultrasound power that reached the flask was calculated using a calorimetric method, and the value was 11.5 J/s [86-88].

Solutions (50 ml) containing 0.2, 1.0 and 4.9 mol/l of MEA were prepared from MEA (Wako) and water that was purified by ion exchange. CO_2 was injected into the solutions at 100 ml/min, and the solution temperature was maintained at 25°C during stirring. Injection was continued until the concentration of CO_2 was stable. The amount of absorbed CO_2 was estimated from the increase in the amount of solution. Values of pH were measured using a pH meter (TOA-DKK).

Experiments on CO_2 desorption were conducted by applying either stirring or ultrasound irradiation to MEA solutions that had absorbed CO_2. The experiments were performed under a nitrogen (N_2) gas flow (100 ml/min) at constant temperatures (25°C) for 5 min [89]. The amount of desorbed CO_2 was evaluated from the weight loss of the solutions.

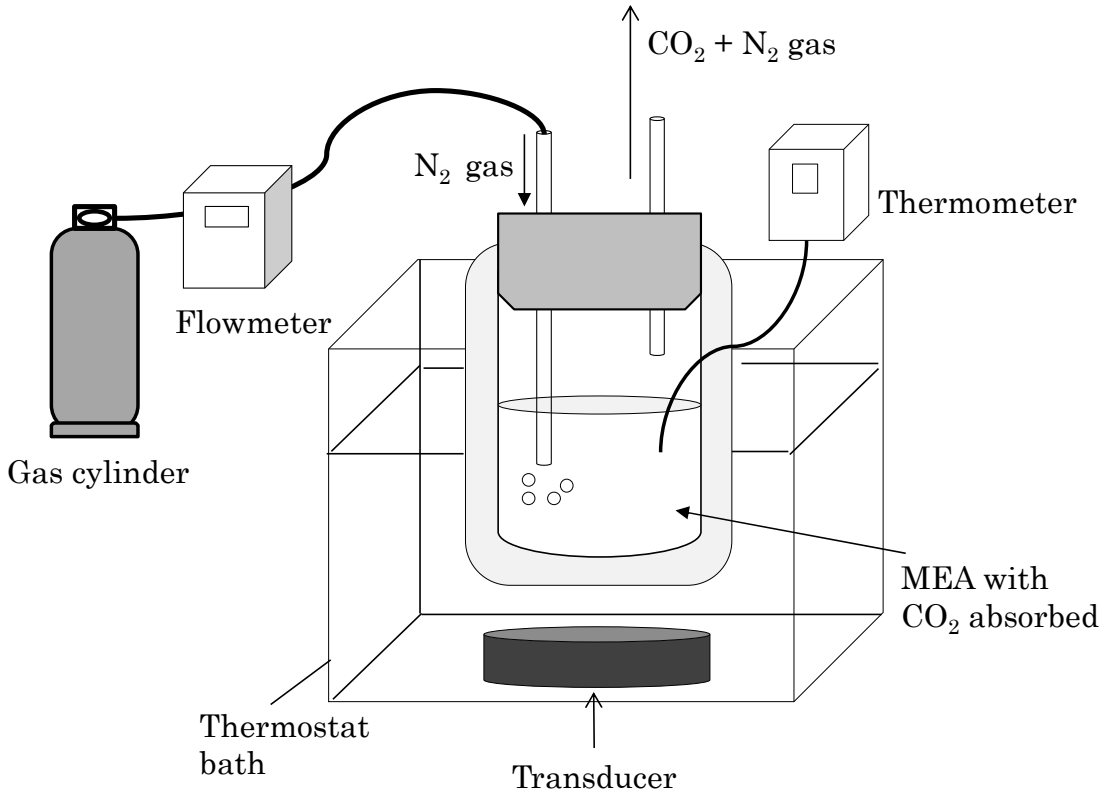

Fig. 4.1 Schematic of the apparatus for CO_2 desorption using ultrasound irradiation.

4.3 Results and Discussion

4.3.1 Preparation of MEA Solution

Figure 4.2 shows the relationship between the amount of CO_2 absorbed and the pH of the MEA solution (0.2 mol/l) during CO_2 gas flow (100 ml/min) under stirring at 1000 rpm. After 1 h, the absorption amount of CO_2 reached about 0.468 g and the pH of the solution decreased from 11.5 to 7.01. The absorption process can be described as follows [90, 91]. MEA solution shows alkaline as MEA reacts with water,

$$RNH_2+H_2O \rightarrow RNH_3^+ + OH^-. \quad (21)$$

Subsequently, RNH_3^+ reacts with OH^- and injected CO_2,

$$RNH_3^+ + 2OH^- + CO_2 \rightarrow RNHCO_2^- + 2H_2O. \quad (22)$$

HCO_3^- ions are generated as injected CO_2 reacts with alkaline water, resulting in a decrease in pH.

$$CO_2 + OH^- \rightarrow HCO_3^-. \quad (23)$$

where R is CH_2CH_2OH. Figure 4.3 shows the viscosities of the MEA solutions at each of the three MEA concentrations. Viscosities were measured using a viscosity meter (DV-III Ultra, BROOKFIELD). It is presumed that the viscosities of the MEA solutions are approximately proportional to the MEA concentration.

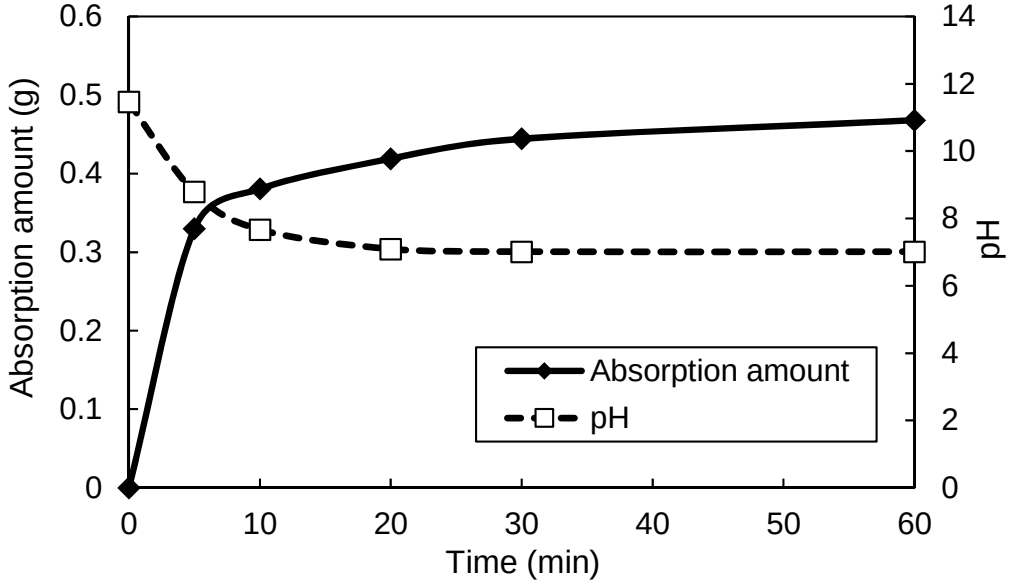

Fig. 4.2 Amounts of CO_2 absorbed and pH of an MEA solution (0.2 mol/l) while stirring at 1000 rpm.

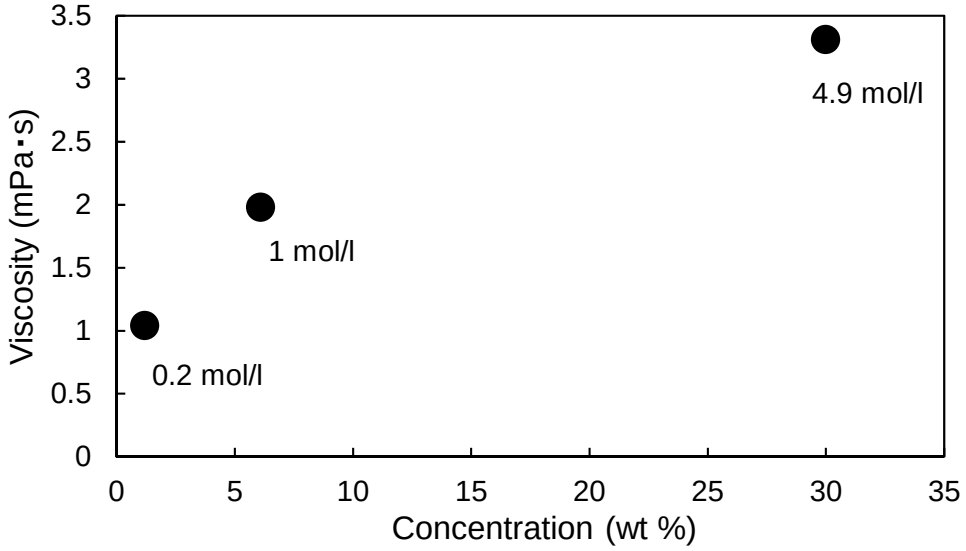

Fig. 4.3 Viscosities of MEA solutions at concentrations of 0.2, 1.0 and 4.9 mol/l.

4.3.2 Desorption Experiment with Stirrer

Figure 4.4 shows the effects of stirrer speed on the rate of CO_2 desorption from the MEA solution (0.2 mol/l) and the pH values of the solutions after treatment at 25°C. The CO_2 desorption rate (%) was calculated by,

$$CO_2 \text{ desorption rate (\%)} = \frac{CO_2 \text{ desorption amount (g)}}{CO_2 \text{ absorption amount (g)}} \times 100 \ , \quad (24)$$

where the amount of absorbed CO_2 was calculated from the weight increase of the solution after CO_2 was injected. The figure shows that both the CO_2 desorption rate and pH increase as the stirrer speed was increased. It is commonly known that CO_2 can be chemically desorbed from MEA solutions by heating [92].

$$RNHCO_2^- + RNH_3^+ \rightarrow 2RNH_2 + CO_2. \quad (25)$$

However, in this study, CO_2 was physically desorbed, and higher speeds of stirring caused higher rates of CO_2 desorption. Thus, it is presumed that HCO_3^- in the solution was degasified as CO_2 by stirring according to,

$$HCO_3^- \rightarrow CO_2\uparrow + OH^-. \quad (26)$$

We also investigated the effect of temperature on CO_2 desorption from the MEA solutions (0.2 mol/l). Desorption experiments were conducted with stirring (1500 rpm) and a N_2 gas flow (100 ml/min) for 5 min at these temperatures: 25, 40, 60, 80 and 95°C. The results are shown in Fig. 4.5; both the amount of CO_2 desorption and the rate of desorption increased with increasing temperature.

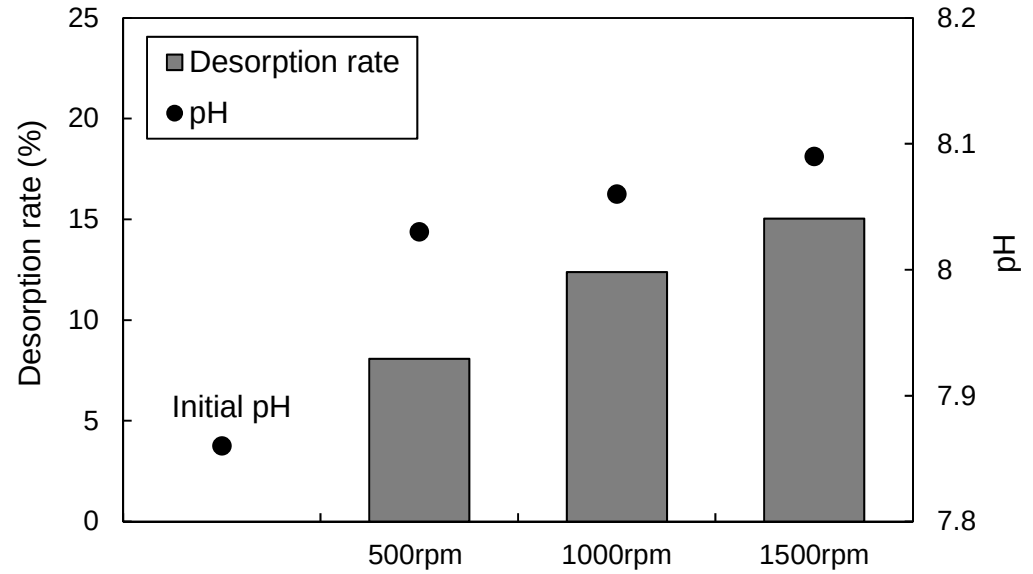

Fig. 4.4 Effect of stirrer speed on rate of CO_2 desorption from absorbed MEA solution (0.2 mol/l) and pH of the solutions (treatment time is 5 min at 25 °C with N_2 flow at 100 ml/min).

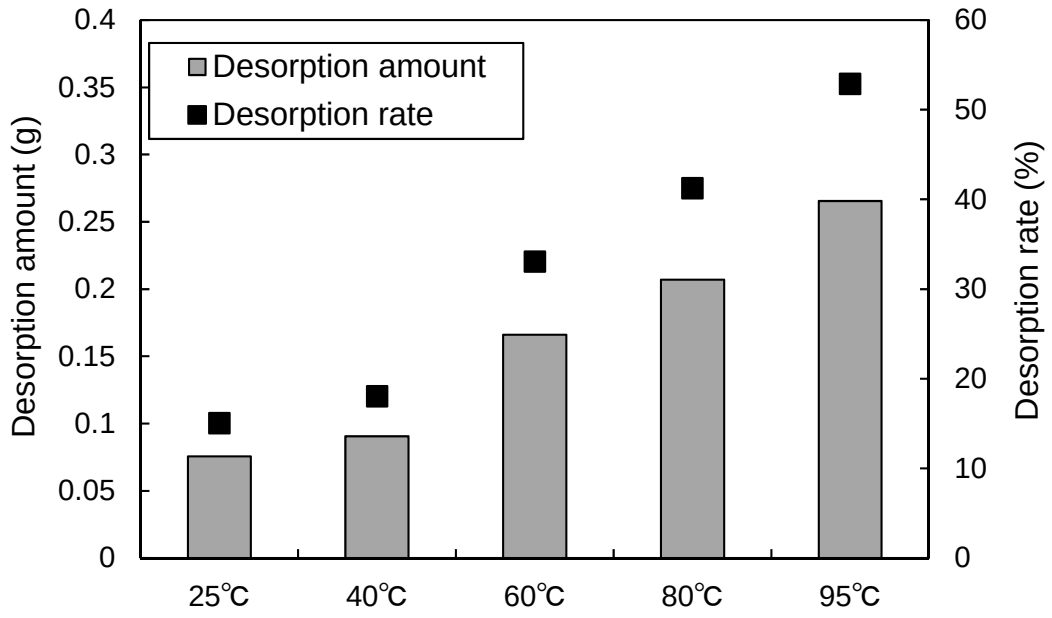

Fig. 4.5 Effects of temperature on amount and rate of CO_2 desorption from absorbed MEA solution (0.2 mol/l) treated by stirring at 1500 rpm (treatment time is 5 min with N_2 flow at 100 ml/min).

4.3.3 Desorption Experiments with Ultrasound Irradiation

The process of degasifying solutions using ultrasound irradiation is well known. Initially, we used our experimental apparatus with ultrasound irradiation and under a N_2 gas flow (100 ml/min) to remove CO_2 (0.0655 g) that had been injected into ion-exchanged water (50 ml). The measured desorption rate induced by ultrasound irradiation for 5 min at 25°C was 51.9% (Fig. 4.6). Subsequently, we used this method to study CO_2 desorption from the MEA solutions. In addition, we tested the ability of N_2 gas to remove CO_2 from the solutions. Figure 4.7 compares the rates of CO_2 desorption induced by ultrasound irradiation with those induced by stirring, both with and without passing N_2 gas through the solutions (0.2 mol/l). We also investigated the rate of CO_2 desorption induced by N_2 gas without the use of ultrasound irradiation and stirring. The obtained results showed that, N_2 gas has the ability to degasify CO_2 from the solution [93], moreover, the use of both ultrasound irradiation and N_2 gas significantly enhanced the CO_2 desorption rate. This result may be attributable to the increased amount of bubbles generated by N_2 gas under ultrasound irradiation. Thus, we investigated the effects of bubble generation on the desorption rates in different MEA solutions. The effects of bubble generation using ultrasound irradiation in a high-viscosity solution such as MEA are known to be small. Therefore, we changed the viscosity of the solution by changing its concentration, as shown in Fig. 4.3. Figure 4.8 compares the rate of CO_2 desorption induced by ultrasound irradiation with that induced by stirring (5 min) for MEA solutions at 25°C and at three MEA concentrations (4.9, 1.0, and 0.2 mol/l). The figure shows that the CO_2 desorption rate induced by ultrasound irradiation at 0.2 mol/l of MEA was the largest among the CO_2 desorption rates induced under all of the investigated conditions. Compared to the results for solutions treated by ultrasound, the desorption rate decreased as the concentration of the MEA solution increased. On the basis of these results, we presumed that the effective bubble generation conditions in <0.2 mol/l MEA solution may be related to the effective degasification of CO_2. However, the results for solutions treated by stirring showed a similar relationship between the MEA concentration and the CO_2 desorption rate. On the basis of the results obtained using either ultrasound irradiation or stirring, we presumed that CO_2 desorption becomes easier with physical action when the concentration of the MEA solution is low. Therefore, we considered the process of CO_2 desorption from low-concentration MEA solutions using ultrasound irradiation. In low-concentration MEA solutions, CO_2 gas is also dissolved as HCO_3^- ions. During ultrasound irradiation, CO_2 is released from HCO_3^-, and the concentration of HCO_3^- decreases. The decreased HCO_3^- is compensated by the reaction of H_2O with CO_2 that is released from carbamate while ultrasound irradiation continues to degasify CO_2 from HCO_3^-.

$$RNHCO_2^- + 2H_2O \xrightarrow{US} RNH_3^+ + HCO_3^- + OH^- \xrightarrow{US} RNH_3^+ + CO_2\uparrow + 2OH^-. \quad (27)$$

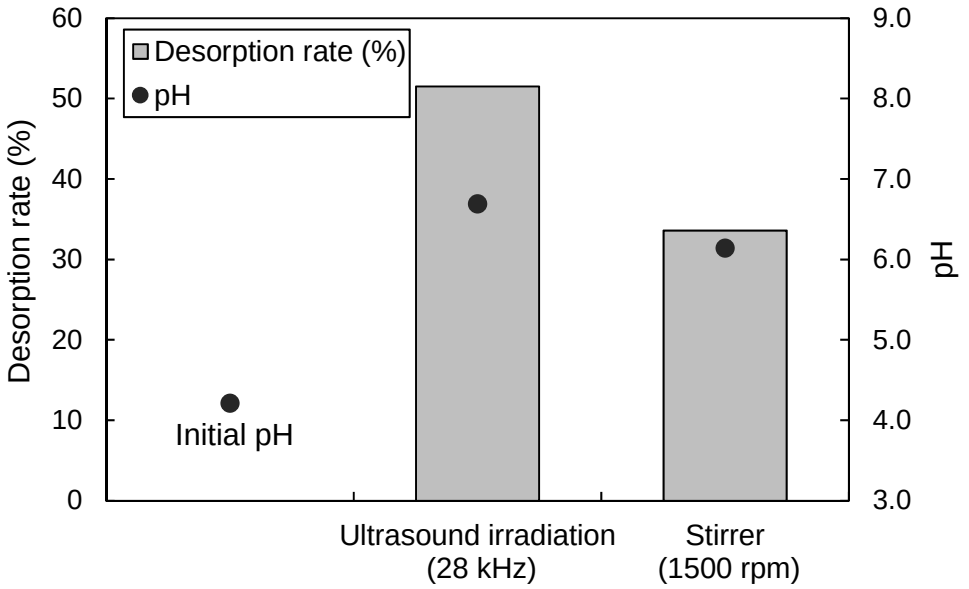

Fig. 4.6 Comparison of rates of CO_2 desorption induced by stirring with those induced by ultrasound irradiation for water injected with CO_2 (treatment time is 5 min at 25 °C with N_2 flow at 100 ml/min).

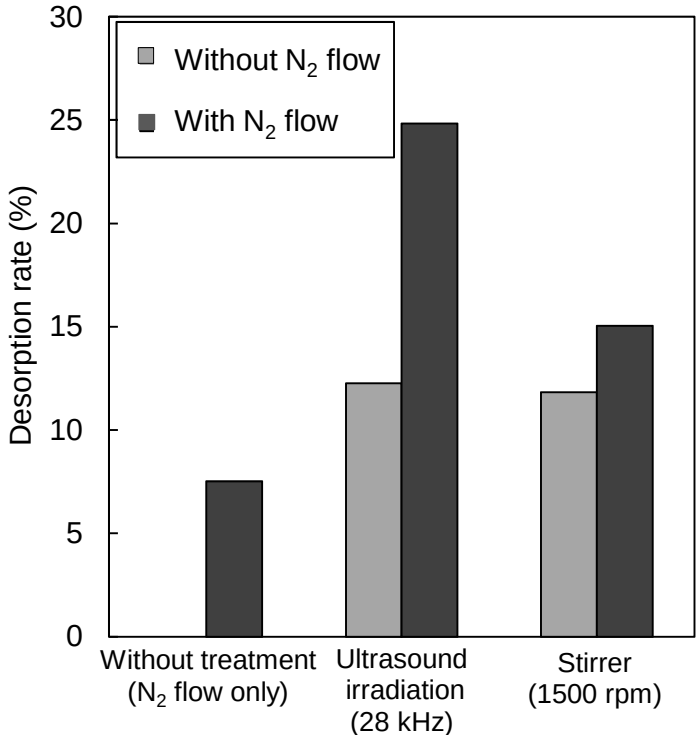

Fig. 4.7 Comparison of rates of CO_2 desorption induced by stirring with those induced by ultrasound irradiation for MEA solutions with and without N_2 flow at 100 ml/min (treatment time is 5 min).

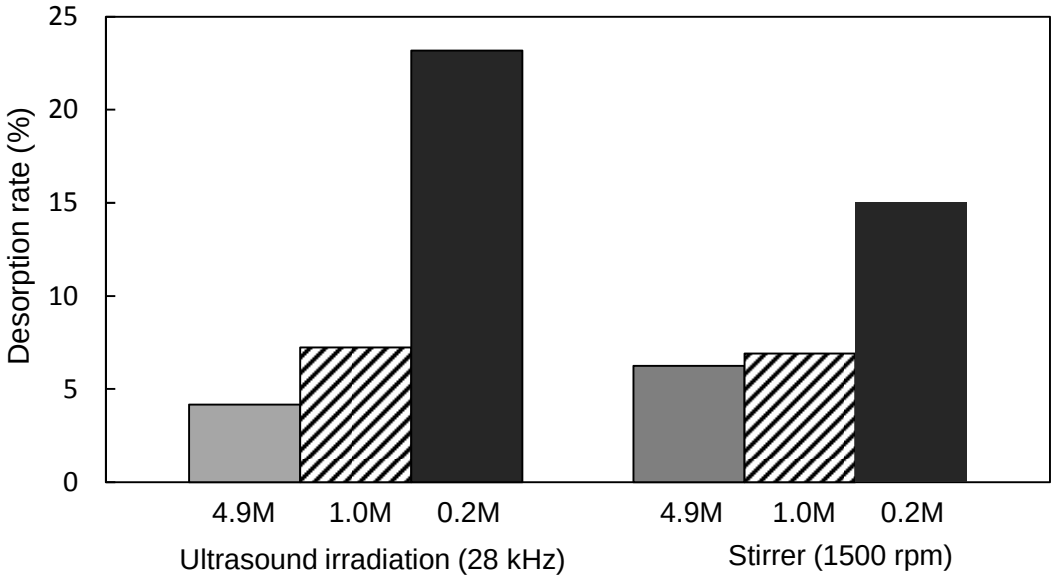

Fig. 4.8 Comparison of rates of CO_2 desorption induced by stirring with those induced by ultrasound irradiation for MEA solutions at three concentrations (each treatment time is 5 min with N_2 flow at 100 ml/min).

Thus, an experiment was conducted wherein CO_2 was injected into a desorbed MEA solution to investigate the regeneration of MEA. Figure 4.9 shows the regeneration desorption－absorption cycle performance of MEA (i.e., the changes in the weight and pH of the MEA solution). The amounts of CO_2 absorbed into and desorbed from the MEA solution were found to be stable; i.e., the amount of CO_2 desorbed was again absorbed into the MEA solution.

Finally, we compared the energy consumed during CO_2 desorption by ultrasound irradiation at 25°C and by stirring (1500 rpm) at 50°C from an MEA solution (0.2 mol/l). As shown in Figs. 4.5 and 4.7, these CO_2 desorption rates from MEA solutions with N_2 gas flow were similar. Therefore we compared amounts of energy consumed under these two sets of conditions. The ultrasound power was considered 11.5 J/s from the results of using a calorimetric method. In this experiment, the ultrasound irradiation time was 5min (300 s). Thus, we calculated the energy consumption according to following formula:

$$11.5\ \text{J/s} \times 300\ \text{s} = 3{,}450\ \text{J}. \quad (28)$$

However, under the stirring condition, energy was primarily consumed by the process of heating the MEA solution from 25 to 50°C. Therefore, energy consumption was calculated according to the following formula using the specific heats of MEA and water [94].

$$2.72\ \text{J/(g} \cdot \text{K)} \times 0.61\ \text{g} \times 25\ \text{K} + 4.18\ \text{J/(g} \cdot \text{K)} \times 49.4\ \text{g} \times 25\ \text{K} = 5{,}203.78\ \text{J}. \quad (29)$$

Hence, these energy consumption values indicated that it is possible to reduce the energy required for traditional approaches by utilizing ultrasound irradiation.

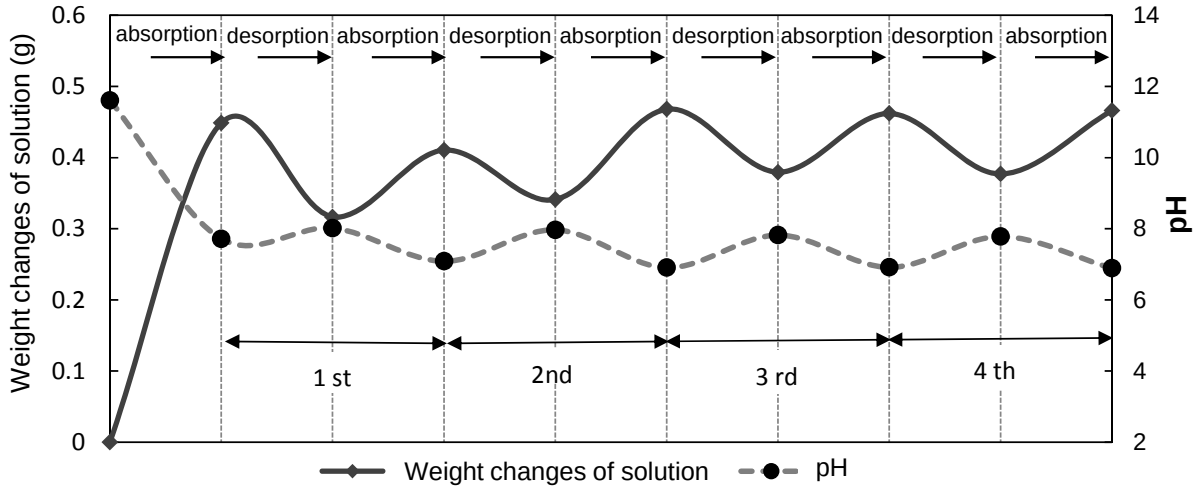

Fig. 4.9 Desorption－absorption cycle performance for MEA regeneration (changes in weight and pH of 0.2 mol/l MEA solution).

4.4 Conclusions

In this study, we conducted experiments to investigate the utilization of ultrasound irradiation for CO_2 desorption from MEA solutions at low temperature. We also considered removing CO_2 by passing N_2 gas through MEA solutions.

We found that ultrasound irradiation of low-concentration MEA solutions was effective for removing CO_2 from the solutions. We considered this occurs because N_2 gas has the ability to degasify CO_2 from the solution and the increased amount of bubble generated by N_2 gas under ultrasound irradiation.

We presumed the process of CO_2 desorption from low-concentration MEA solutions from results of several experiments. The results suggested the process is as follows. During absorption of CO_2, carbamate bonds form via reactions between MEA and CO_2. Moreover, CO_2 gas is dissolved as HCO_3^- ions in the MEA solution. When the solution is exposed to ultrasound irradiation, CO_2 is removed from the HCO_3^- ions in the solution. At this time, carbamate bonds supply more CO_2 to release the missing HCO_3^- ions. This process continues until CO_2 is largely removed from the solution.

Finally, we compared the energy consumed during CO_2 desorption by ultrasound irradiation (25°C) and by stirring (50°C) from an MEA solution (0.2 mol/l), we found ultrasound irradiation has the possibility to reduce the energy of traditional approach for CO_2 desorption from low-concentration MEA solution.

Chapter 5

Desorption of CO_2 from low concentration monoethanolamine solutions using calcium chloride and ultrasound irradiation

5.1 Introduction

Carbon dioxide (CO_2) is one of the gases that can cause global warming. The emission of CO_2 from power production plants is one of the most serious global environmental problems because these plants emit approximately 30×10^9 t of CO_2 each year [18]. Therefore, it is necessary to develop technologies that can lead to less CO_2 being emitted. Some electricity is currently generated from renewable sources of energy, but approximately 40% of electricity is generated using coal [19]. More CO_2 is emitted per unit of electricity generated by coal-fired power plants than by plants using other fossil fuels. However, it is likely that coal will continue to be used as a major source of power in the future because it offers several advantages over other fossil fuels, including the existence of large coal reserves, low geopolitical risks, and its relatively low price. A carbon capture and storage (CCS) technique is being developed to decrease CO_2 emissions from coal-fired plants because of the expected continued use of coal to generate electricity. It is desirable to develop a CCS technique for transporting CO_2 captured from power plants and storing it in underground aquifers as a matter of urgency [14, 21, 22, 29, 33, 58, 95].

The capture of CO_2 from exhaust gases from thermal power plants can be achieved using several methods, including the chemical absorption of CO_2 by an absorbent such as an amine, the physical absorption of CO_2 by an absorbent such as methanol at a high pressure and a low temperature, and the absorption of CO_2 by a membrane [66, 96-99]. Many studies aimed at increasing the effectiveness with which CO_2 can be desorbed from the absorbents used in absorber units in coal-fired power plants. In particular, the properties of alkanolamines have been studied through laboratory experiments and model simulations because alkanolamines are often used as chemical absorbents [100, 101].

Aqueous monoethanolamine (MEA) has been used as an absorbent for removing CO_2 because MEA offers several advantages over other alkanolamines. These advantages include its relatively high degree of reactivity and the low cost of the solvent. The CO_2 absorption capacity of MEA depends on the ambient temperature, pressure, and MEA concentration [71, 74 93]. The carbamate ion is generated when CO_2 is absorbed by an MEA solution through the following reaction [102-104]

$$2RNH_2 + CO_2 \rightarrow RNHCOO^- + RNH_3^+ \qquad (R = C_2H_5O). \tag{30}$$

Zwitterion is formed from the MEA and CO_2 reaction.

$$RNH_2 + CO_2 \rightarrow RNH_2^+COO^-. \tag{31}$$

The carbamate ion can also react with CO_2 through the following reaction:

$$RNHCOO^- + 2H_2O + CO_2 \rightarrow 2HCO_3^- + RNH_3^+. \quad (32)$$

However, significant corrosion problems are caused by the degradation of MEA in carbon sequestration facilities, so the MEA concentration must be kept low to protect the equipment [105]. Decreasing the MEA concentration means that more energy is required to recover CO_2. In general, CO_2 is desorbed from the absorbent within the thermal power plant in which the CO_2 was produced by heating the absorbent to perform a regeneration process [106]. The amount of energy required to heat the absorbent per mole of CO_2 desorbed will increase as the MEA concentration decreases because the specific heat capacity of water [4.18 J/(g·K)] is higher than the specific heat capacity of MEA [2.72 J/(g·K)]. Almost all the commercial applications of MEA that have been reported have used high MEA concentrations, but the use of low MEA concentrations described in studies has not been widely published [107-109].

We previously performed a study in which we aimed to determine whether using ultrasound irradiation and a flow of N_2 gas could facilitate the desorption of CO_2 from an MEA solution at a low temperature. We found that less energy was required to desorb CO_2 from a solution with a low MEA concentration (0.2 mol/l) when the solution was kept at 25 °C and ultrasound irradiation was applied than when the solution was kept at 49 °C and stirred at 1,500 rpm. Degasification using ultrasound irradiation is a well-known method for releasing dissolved gases from a solution. It is difficult to directly desorb CO_2 from MEA but easy to desorb CO_2 from HCO_3^- by applying ultrasound irradiation. Therefore, we found that increasing the amount of HCO_3^- that was present in the MEA solution by degasifying the solution and applying ultrasound irradiation increased the amount of CO_2 that was desorbed. However, only 24.8% of the CO_2 absorbed by the MEA solution was desorbed using that method [110]. Therefore, we need to improve the proportion of CO_2 that can be desorbed from an MEA solution.

In a previous study, it was found that adding calcium chloride ($CaCl_2$) to an MEA solution (1 mol/l) caused CO_2 to be desorbed from MEA very efficiently (> 90%) because the CO_2 desorbed from the MEA formed $CaCO_3$ in the solution. The presence of Ca^{2+} in the MEA solution increased the amount of HCO_3^- that formed in the solution [111]. $CaCO_3$ formed through the reaction between CO_2 and Ca^{2+} can be used in desulfurization units in pulverized coal combustion plants [112]. To the best of our knowledge, it has not yet been determined whether CO_2 can be desorbed efficiently from a solution containing a low MEA concentration using $CaCl_2$ when the solution is stirred or when ultrasound irradiation is applied. In the study described here, we determined the CO_2 desorption efficiency achieved when a solution containing a low MEA concentration is treated with $CaCl_2$ and the solution is stirred or ultrasound irradiation is applied, and we also characterized the $CaCO_3$ particles that were generated during the degasification processes.

5.2 Experimental methods

The desorption of CO_2 from an MEA solution was investigated using an ultrasound generator (Kaijo, TA-4021) and a submersible transducer (28 kHz) [80, 83]. The output of the ultrasound generation device was set at 200 W. An experiment was also conducted using the same conditions using a stirrer (at a stirring speed of 1,500 rpm) instead of the ultrasound generator, and the results of this experiment were compared with these obtained using ultrasound. A schematic of the apparatus used for the CO_2 desorption experiment using ultrasound is shown in Fig. 5.1. The ultrasound treatment was conducted in a cycloid-type thermostat-controlled bath (Thermo Electron) so that the solution temperature could be kept at 25 °C during the experiment. Each MEA solution was placed in a flat-bottomed flask that was irradiated from the bottom. The ultrasound power that reached the flask was found to be 11.8 W using a calorimetric calculation method [113]. A 30 ml solution containing MEA at a low concentration (0.2 mol/l) was prepared from MEA (Wako Pure Chemicals Industries) and ion-free water (prepared by passing water through an ion exchange column). A mixture of 10% CO_2 and 90% N_2 (called inlet gas) was injected into the MEA solution at 200 ml/min for 30 min while the solution was stirred (at 750 rpm) and kept at 25 °C [114]. The composition of the inlet gas was chosen because the main components of flue gases are generally N_2 (76–77%), CO_2 (12.5–12.8%), H_2O (6.2%), and O_2 (4.4%) [79]. A 30 ml test solution was then prepared by adding a $CaCl_2$ (Wako Pure Chemicals) solution to the solution containing MEA and the absorbed CO_2. Desorption experiments were conducted for 5 min at several temperatures either with ultrasound irradiation (at 28 kHz) or with stirring (at 1,500 rpm). The mass of $CaCO_3$ generated by the reaction between HCO_3^- and Ca^{2+} in the solution was determined at the end of each experiment by filtering and drying the solution. The amount of carbon in the solution was analyzed using a total carbon (TC) measurement system (TOC-V_{CSH}; Shimadzu) and the mass of $CaCO_3$ produced was determined using an electronic balance. The pH was determined using a pH meter (TOA-DKK).

The amount of CO_2 desorbed from the MEA solution was determined from the total amount of CO_2 in the $CaCO_3$ that was generated and the amount of CO_2 that was degassed from the solution. The total desorption ratio (D_{total}) was calculated as

$$D_{total}\,(\%) = D_{CaCO_3}\,(\%) + D_{CO_2}\,(\%), \tag{33}$$

where D_{CaCO_3} (%) is the percentage of the CO_2 that was desorbed as $CaCO_3$ and D_{CO_2} (%) is the percentage of the CO_2 that was desorbed as a gas from the solution. D_{CaCO3} and D_{CO_2} were calculated using Eqs. (34) and (35), respectively.

$$D_{CaCO_3}(\%) = \frac{M_{CaCO_3}}{M_{abs}} \times 100, \tag{34}$$

$$D_{CO_2}(\%) = \frac{M_{abs} - M_{CaCO_3} - M_{residual}}{M_{abs}} \times 100, \quad (35)$$

where M_{abs} (mol/l) is the CO_2 concentration absorbed by the MEA solution during the preparation phase of the experiment and M_{CaCO_3} (mol/l) is the concentration calculated from the mass of $CaCO_3$ that was generated by the end of the desorption experiment. $M_{residual}$ (mol/l) is the residual CO_2 concentration in the MEA solution, calculated from the TC concentration at the end of the desorption experiment.

The $CaCO_3$ produced was subjected to structural analysis using X-ray diffraction (XRD; Rigaku, RINT2200) and the shapes of the $CaCO_3$ particles were determined using scanning electron microscopy (SEM; Hitachi, TM-1000). The $CaCO_3$ particle diameters were determined using a grain size distribution analyzer (Nikkiso, Microtrac MT3300).

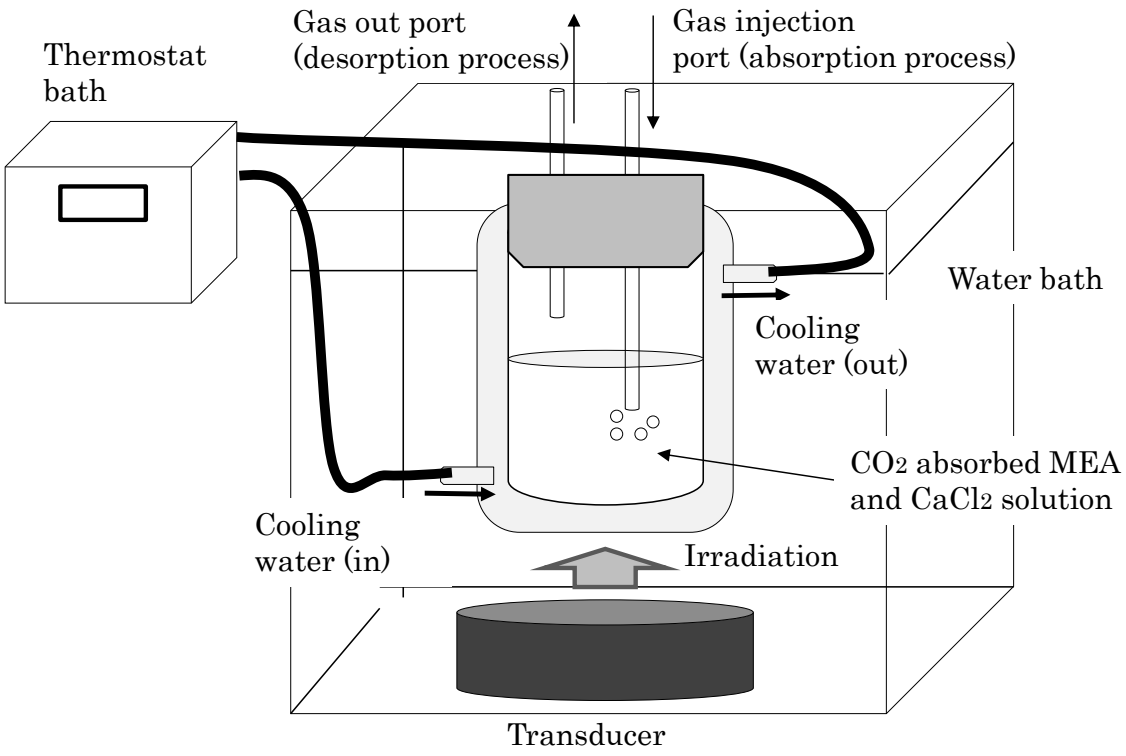

Fig. 5.1 Schematic of the apparatus used for the CO_2 desorption experiments using ultrasound irradiation.

5.3 Results and discussion

We first investigated the ability of a solution containing a low MEA concentration (0.2 mol/l) to absorb CO_2. MEA addition makes the solution alkaline, as shown by the reaction in Eq. (36). The changes in the amount of CO_2 absorbed by the MEA solution and the pH of the solution as the inlet gas was bubbled into the solution at 200 ml/min and the solution was stirred (750 rpm) for 30 min at 25 °C are shown in Fig. 5.2. The absorbed CO_2 concentration reached 0.159 mol/l after 15 min and 0.155 mol/l after 30 min. We found that the maximum possible amount of CO_2 had been absorbed after 15 min because the amount of CO_2 absorbed did not change after that time. The pH of the solution decreased from 11.3 at the beginning of the test to 7.25 after 15 min. This was caused by the occurrence of the reactions shown in Eqs. (37)-(39) [115]. The amount of absorbed CO_2 did not change after 15 min; however, the pH changed from 7.25 after 15 min to 6.97 after 30 min. This may come from the ionization of H_2CO_3 in the near-neutral region, as shown by Eqs. (40) and (41) [116, 117].

$$RNH_2 + H_2O \rightarrow RNH_3^+ + OH^-. \quad (36)$$

$$RNH_3^+ + OH^- + CO_2 \rightarrow RNH_2^+COO^- + H_2O. \quad (37)$$

$$RNH_2^+COO^- + OH^- \rightarrow RNHCOO^- + H_2O. \quad (38)$$

$$CO_2 + OH^- \rightarrow HCO_3^-. \quad (39)$$

$$CO_2 + H_2O \rightarrow H_2CO_3. \quad (40)$$

$$H_2CO_3 \rightarrow HCO_3^- + H^+ \qquad (pKa = 6.3). \quad (41)$$

The decrease in the pH over time during the CO_2 absorption test indicated that CO_2 was absorbed by the MEA solution. The desorption of CO_2 from the MEA solution in later experiments could therefore be confirmed by monitoring the changes in the pH values of the solutions during the desorption experiments.

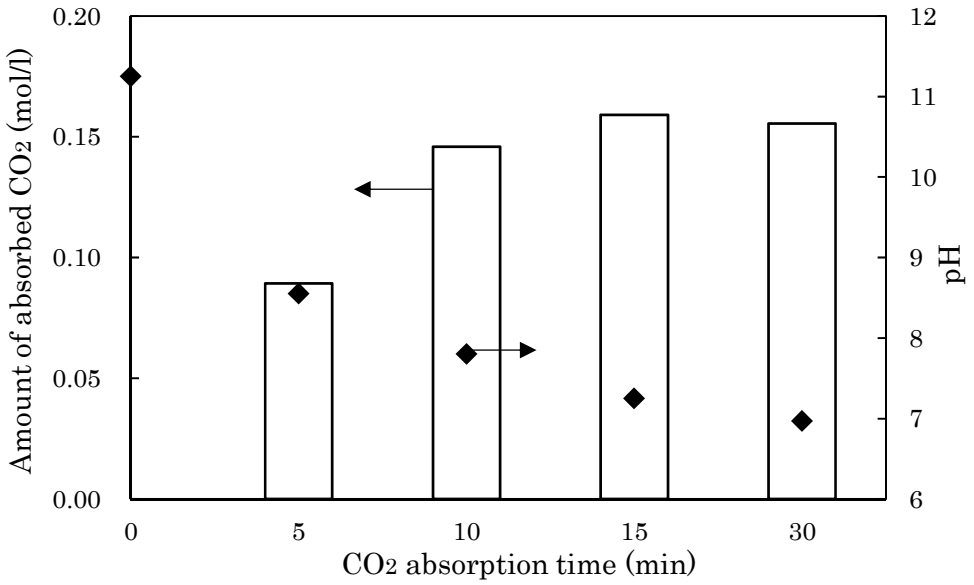

Fig. 5.2 Changes in the amount of absorbed CO_2 and the pH of the MEA solution (0.2 mol/l) during the application of inlet gas (at a rate of 200 ml/min) with stirring (at 750 rpm) for 30 min at 25 °C.

The CO_2 desorption ratios and the pH values for the MEA solution without $CaCl_2$ added when it was treated at different temperatures (25, 40, 60, and 80 °C) with either ultrasound irradiation or stirring for 5 min are shown in Fig. 5.3. As can be seen, the CO_2 desorption ratio at 25 °C was higher when ultrasound irradiation was used than when the solution was stirred. We concluded that the efficiency with which ultrasound irradiation causes degasification enhanced the release of CO_2 from HCO_3^- in the MEA solution. The pH increased, because OH^- was generated, more at a low temperature when the solution was treated with ultrasound irradiation than when it was stirred. The OH^- ion was produced because of the reaction.

$$HCO_3^- \rightarrow CO_2\uparrow + OH^-. \quad (42)$$

However, at temperatures higher than 60 °C, the CO_2 desorption ratio was higher when the solution was stirred than when it was treated with ultrasound irradiation. This was because more CO_2 was released through desorption caused by heat being applied than degasification caused by ultrasound irradiation at higher temperatures.

The D_{total} values obtained at four temperatures (25, 40, 60, and 80 °C) for MEA solutions

containing $CaCl_2$ treated with ultrasound irradiation (at 28 kHz) for 5 min are shown in Fig. 5.4. The addition of $CaCl_2$ (to give a concentration of 0.1 mol/l) to the solution containing MEA with absorbed CO_2 caused the reactions shown in Eqs. (42) and (43) to occur.

$$(R\text{-})\ HCO_3^- + Ca^{2+} \rightarrow CaCO_3 + H^+. \quad (43)$$

The D_{total} for the MEA solution in this case included the amount of CO_2 degasified by ultrasound irradiation and the amount of CO_2 present as $CaCO_3$ produced by the addition of the $CaCl_2$ solution. We confirmed that the D_{total} increased as the temperature of the solution increased, and this was concluded to be predominantly caused by the increased degasification of CO_2 at higher temperatures because the D_{CaCO_3} changed slightly as the temperature increased. We concluded that the degasification of CO_2 was dependent on the temperature, but that the generation of $CaCO_3$ was independent of the temperature.

The D_{total} values for the MEA solutions obtained at 25 °C with and without $CaCl_2$ added and treated with ultrasound irradiation or stirring for 5 min are shown in Fig. 5.5. It can be seen that the D_{total} found using ultrasound irradiation reached 78.8% when the $CaCl_2$ solution was added to the MEA solution but was only 16.2% when the $CaCl_2$ solution was not added. The D_{total} found when the solution was stirred reached 72.2% when the $CaCl_2$ was added but was only 10.1% when $CaCl_2$ was not added. The D_{CO_2} was 16.2% when the solution was treated with ultrasound irradiation but it increased to 40.4% when $CaCl_2$ was also added. Similarly, the D_{CO_2} was 10.1% when the solution was stirred but increased to 39.4% when $CaCl_2$ was also added. The increases in the D_{total} values were presumably caused by the displacement of an equilibrium reaction in the solution, caused by the addition of the $CaCl_2$ solution. $CaCO_3$ was generated through the reaction between Ca^{2+} (from the $CaCl_2$) and HCO_3^- [from the CO_2 desorbed from the MEA, as shown in Eq. (43)]. The amount of HCO_3^- in the solution would have decreased because of $CaCO_3$ being formed. This would then have caused CO_2 desorbed by the MEA to be released and to form HCO_3^- because the equilibrium reaction shown in Eq. (44) would have been displaced.

$$RNHCOO^- + H_2O \rightarrow RNH_2 + HCO_3^-. \quad (44)$$

We therefore concluded that the proportion of CO_2 that was degasified was increased to a large extent by the efficiency with which applying ultrasound irradiation or stirring caused CO_2 to be released from the solution.

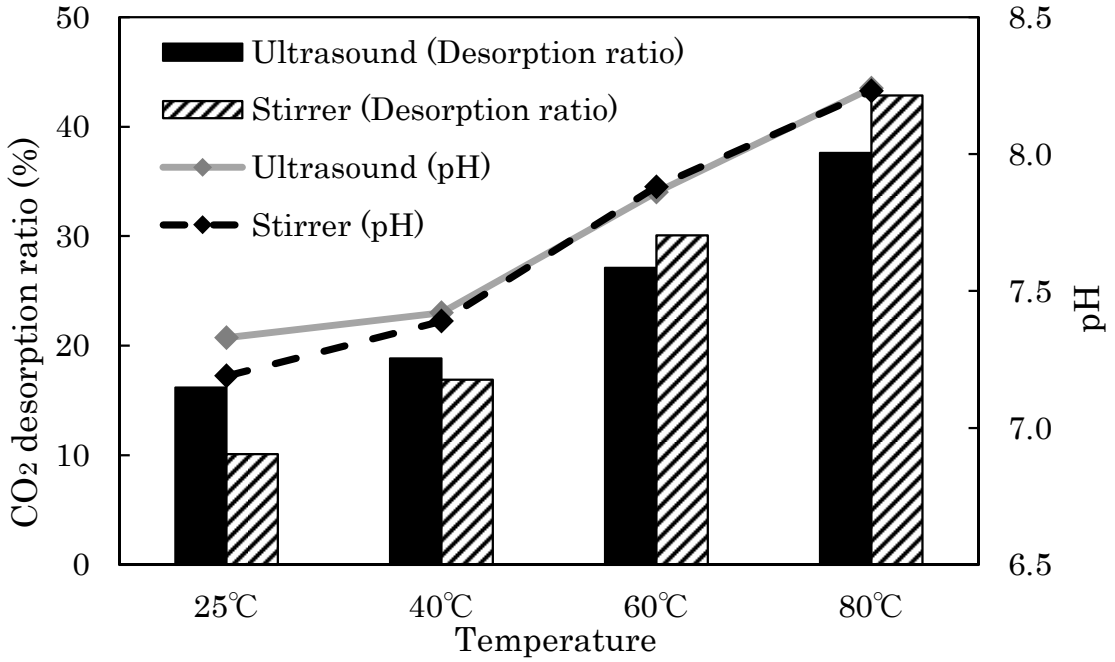

Fig. 5.3 CO_2 desorption ratios for MEA solutions without $CaCl_2$ added and the pH of the solutions in experiments performed with ultrasound irradiation (at 28 kHz) treatment or with stirring (at 1,500 rpm) for 5 min at 25, 40, 60, and 80 °C.

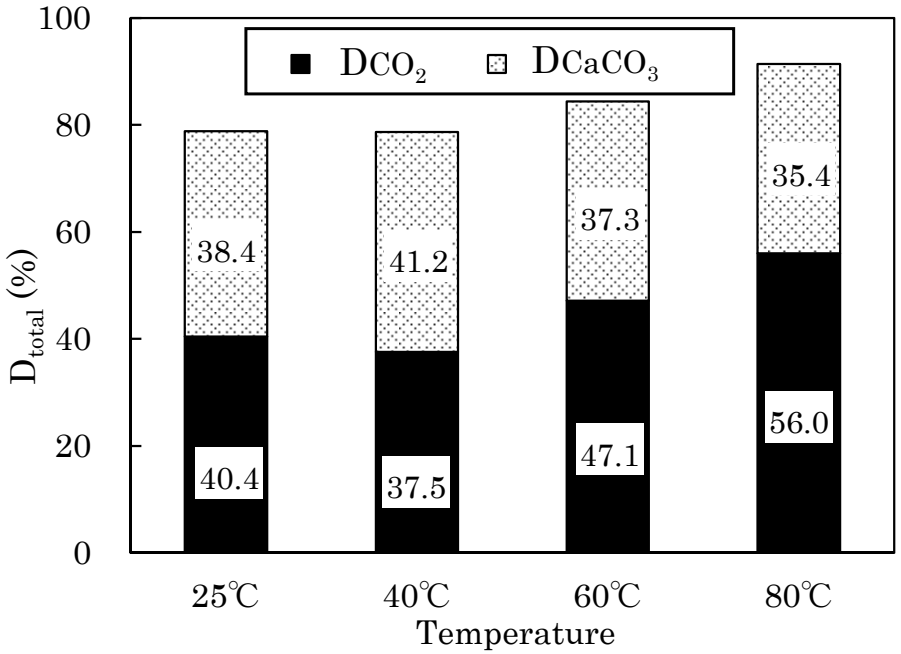

Fig. 5.4 CO_2 desorption ratios for MEA solutions with $CaCl_2$ (0.1 mol/l) added and treated with ultrasound irradiation (at 28 kHz) for 5 min at 25, 40, 60, and 80 °C.

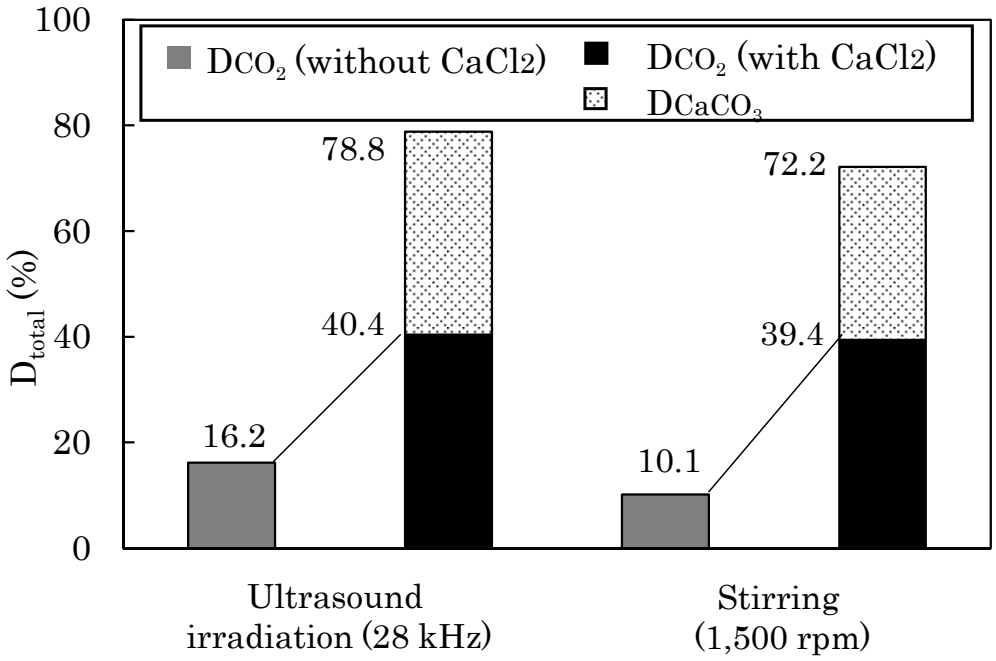

Fig. 5.5 Total CO_2 desorption ratios for MEA solutions with and without $CaCl_2$ (0.1 mol/l) added and with ultrasound irradiation (at 28 kHz) treatment or with stirring (at 1,500 rpm) for 5 min at 25 °C.

We confirmed that adding $CaCl_2$ increased the proportion of CO_2 that was degasified from the MEA solution when the solution was treated with ultrasound irradiation or stirred. However, the $CaCO_3$ yield was 70% when $CaCl_2$ (0.1 mol/l) was added. Therefore, we investigated the effect of the $CaCl_2$ concentration on the proportion of CO_2 that was degasified from the MEA solution so that we could decrease the amount of $CaCO_3$ that was generated. The D_{CO_2} and D_{CaCO_3} values found when three different $CaCl_2$ concentrations were used are shown in Fig. 5.6. The $CaCl_2$ concentrations were chosen so that the ratios of the $CaCl_2$ concentrations (0.1, 0.05, and 0.01 mol/l) to the MEA concentration (0.2 mol/l) were 0.5, 0.25, and 0.05, respectively. The results confirmed that the D_{CaCO_3} had a proportional relationship with the $CaCl_2$ concentration. The D_{CO_2} was 16.2% for the solution treated with ultrasound irradiation when the $[CaCl_2]/[MEA]$ ratio was 0, but adding a small amount of $CaCl_2$ to bring the $[CaCl_2]/[MEA]$ ratio to 0.05 caused the D_{CO_2} to increase to 29.3%. The D_{CO_2} was 10.1% for the solution that was stirred when the $[CaCl_2]/[MEA]$ ratio was 0, but bringing the $[CaCl_2]/[MEA]$ ratio to 0.05 caused the D_{CO_2} to increase to 21.9%. The mechanisms that we concluded to cause the D_{CO_2} to increase when $CaCl_2$ was added and the D_{CO_2} to be higher when the solution was treated with ultrasound irradiation than when it was stirred are given next. $CaCO_3$ is slightly soluble because it has a solubility product K_{sp} of 3.6×10^{-9} in water at 25 °C. However, there was an excess (~ 25.8 times) of CO_2 absorbed by MEA compared with the amount of $CaCO_3$ generated by the reaction between the $CaCl_2$ and CO_2 absorbed by the MEA, so some of the $CaCO_3$ would have changed into $Ca(HCO_3)_2$ in the solution. The $Ca(HCO_3)_2$ in the solution would have become ionized. These reactions are shown as

$$CaCO_3 + H_2O + CO_2 \rightarrow Ca(HCO_3)_2, \quad (45)$$

$$Ca(HCO_3)_2 \rightarrow Ca^{2+} + 2HCO_3^-. \quad (46)$$

The CO_2 would then have finally been degassed from the HCO_3^- because of the efficiency with which ultrasound irradiation causes degasification, following the reaction.

$$HCO_3^- \xrightarrow{U.S} CO_2\uparrow + OH^-. \quad (47)$$

The D_{CO_2} increased because of the processes described above, and applying ultrasound irradiation caused more CO_2 degasification to occur than did stirring. The D_{CaCO_3} and D_{CO_2} values for the solutions treated with ultrasound irradiation and stirring for 60 min at 25 °C when the $[CaCl_2]/[MEA]$ ratio was 0.05 are shown in Fig. 5.7. The D_{CO_2} increased rapidly until 5 min had elapsed and then increased gradually until 60 min had elapsed. However, the D_{CaCO_3} increased only slightly by the time 5 min had elapsed and was stable by the time 60 min had elapsed. The initial pH of the solution was 7.04 and, after 5 min, the solution had a pH of 7.86 when it had been treated with ultrasound irradiation and a pH of 7.66 when it had been stirred. The pH of the solution increased

because of CO_2 being degassed, as shown in Eq. (42). Therefore, we concluded that applying ultrasound irradiation caused more degasification to occur than did stirring even in as short a time as 5 min.

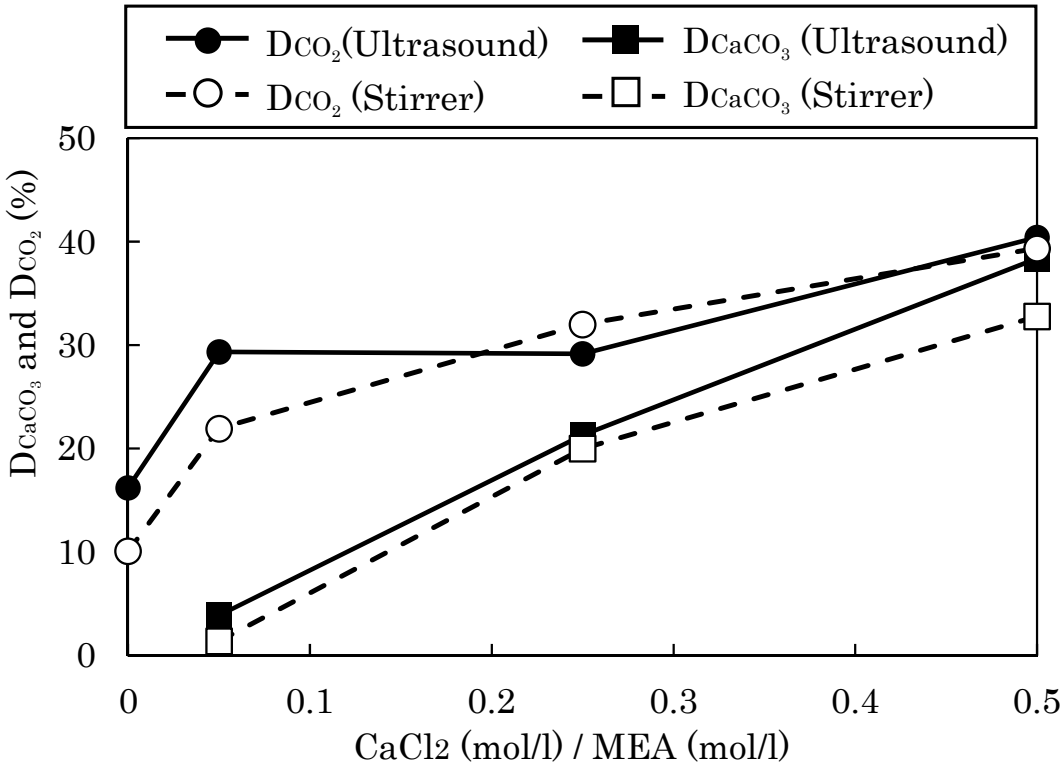

Fig. 5.6 Changes in the ratio of CO_2 desorbed to $CaCO_3$ generated (D_{CaCO_3}) and the degasified CO_2 desorption ratio (D_{CO_2}) at different $CaCl_2$ concentrations with ultrasound irradiation (at 28 kHz) treatment or with stirring (at 1,500 rpm) for 5 min at 25 °C. (The MEA concentration was 0.2 mol/l.)

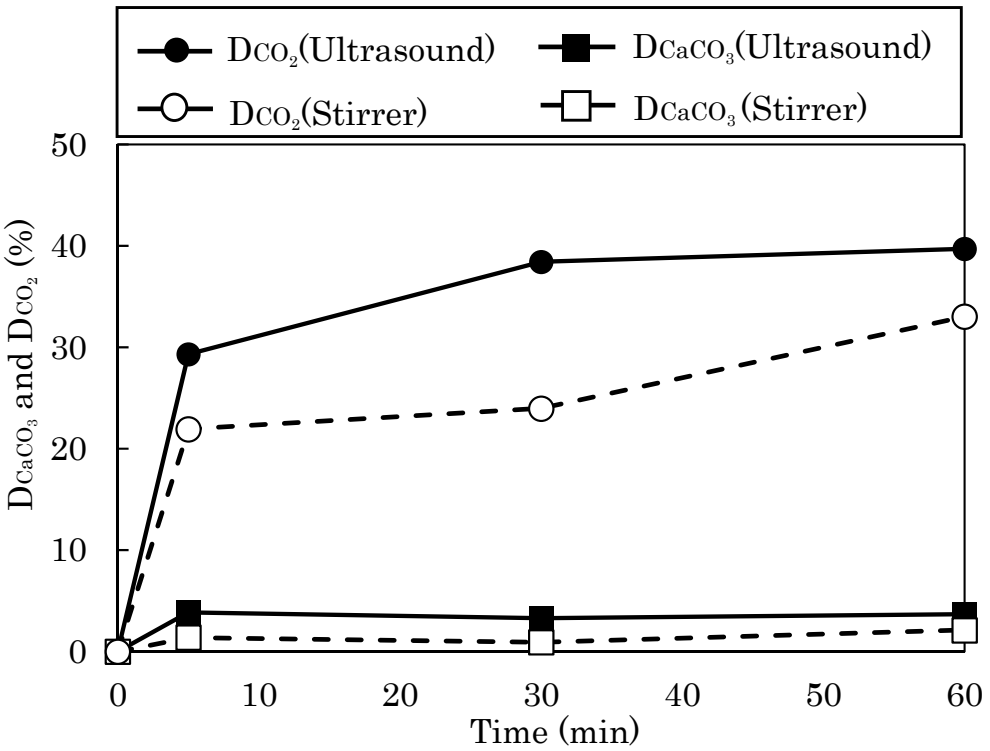

Fig. 5.7 Changes in the ratio of CO_2 desorbed to $CaCO_3$ generated (D_{CaCO_3}) and the degasified CO_2 desorption ratio (D_{CO_2}) when the solution was treated with ultrasound irradiation (at 28 kHz) and when the solution was stirred (at 1,500 rpm) for 60 min at 25 °C when the [$CaCl_2$]/[MEA] ratio was 0.05.

Finally, we determined the properties of the $CaCO_3$ that was generated in the desorption experiments using XRD and SEM. The XRD patterns for the $CaCO_3$ synthesized when 0.1 mol/l $CaCl_2$ was added and the solution was stirred or treated with ultrasound for 5 min at 25 °C are shown in Fig. 5.8. The peaks for the $CaCO_3$ generated when ultrasound irradiation was applied indicated that the $CaCO_3$ was calcite, and the peaks for the $CaCO_3$ generated when the solution was stirred indicated that the $CaCO_3$ was vaterite and calcite. A SEM image of the $CaCO_3$ produced when a solution was treated with ultrasound irradiation is shown in Fig. 5.9(a) and a SEM image of the $CaCO_3$ produced when a solution was stirred is shown in Fig. 5.9(b). Calcite with homogeneous hexahedron particles was found when the desorption experiments were conducted with the application of ultrasound irradiation [Fig. 5.9(a)]. However, inhomogeneous calcite and spherical vaterite particles were found when the desorption experiments were conducted with the solution stirred [Fig. 5.9(b)]. The particle size distributions for the $CaCO_3$ generated after 5 min in the ultrasound-treated and stirred solutions are shown in Fig. 5.10. It can be seen from Fig. 5.10 that the $CaCO_3$ particle sizes were more homogeneous and smaller when the particles were produced in a solution that was treated with ultrasound irradiation than when the particles were produced in a solution that was stirred. It has been reported that ultrasound irradiation can cause $CaCO_3$ to be generated and that ultrasound irradiation can cause smaller particles to be produced than when a solution is stirred [118, 119]. Therefore, we concluded that fine particles of calcite formed when a solution was treated with ultrasound irradiation because of the speed at which the calcite was generated. $CaCO_3$ is used as a slurry in conventional desulfurization processes in fossil fuel-fired-power plants. Calcite is stable in such a slurry, and homogeneous particle sizes are advantageous in terms of the costs involved in sieving the particles [120]. Therefore, it is expected that the $CaCO_3$ by-product generated by extracting captured CO_2 by treating a CO_2 solution with $CaCl_2$ and ultrasound irradiation could be used in desulfurization processes in the future.

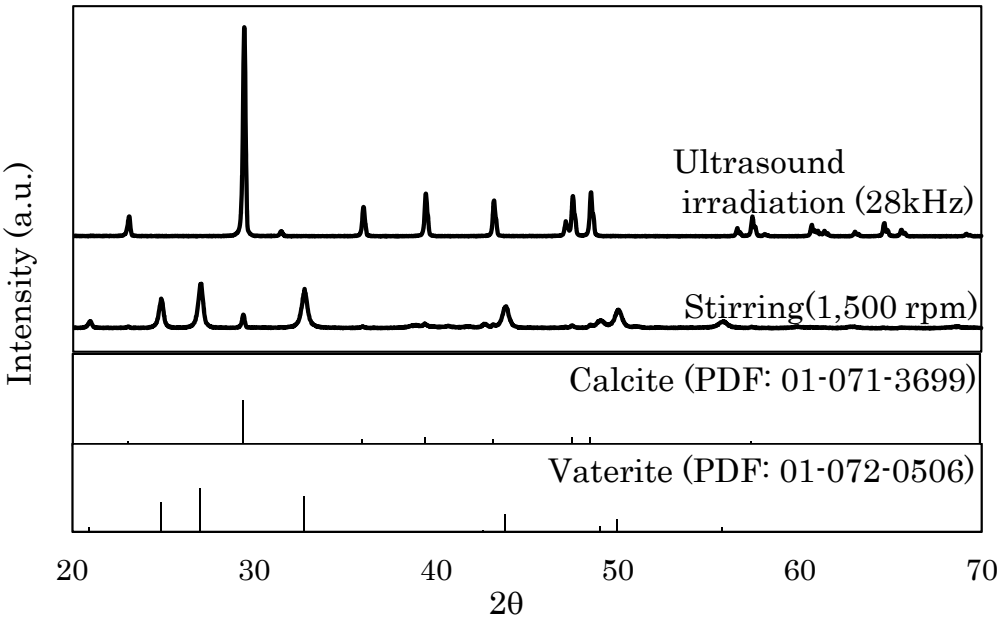

Fig. 5.8 XRD patterns for the $CaCO_3$ produced at 25 °C when 0.1 mol/l $CaCl_2$ was added to a solution and the solution was treated with ultrasound irradiation (at 28 kHz) and when the solution was stirred (at 1,500 rpm).

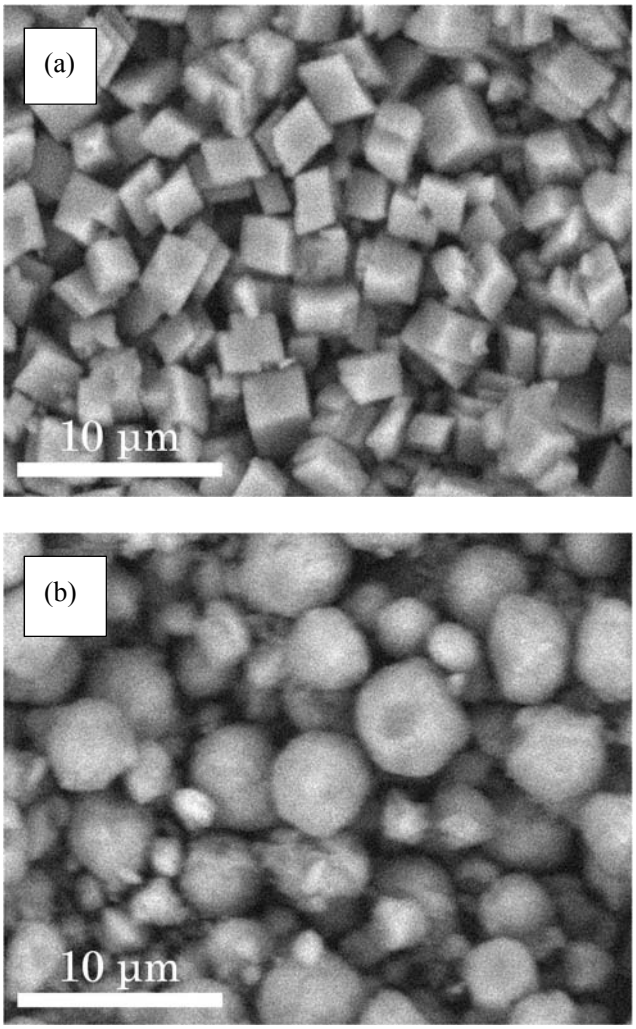

Fig. 5.9 SEM images of the $CaCO_3$ produced at 25 °C when 0.1 mol/l $CaCl_2$ was added to a solution and (a) the solution was treated with ultrasound irradiation (at 28 kHz) and (b) the solution was stirred (at 1,500 rpm).

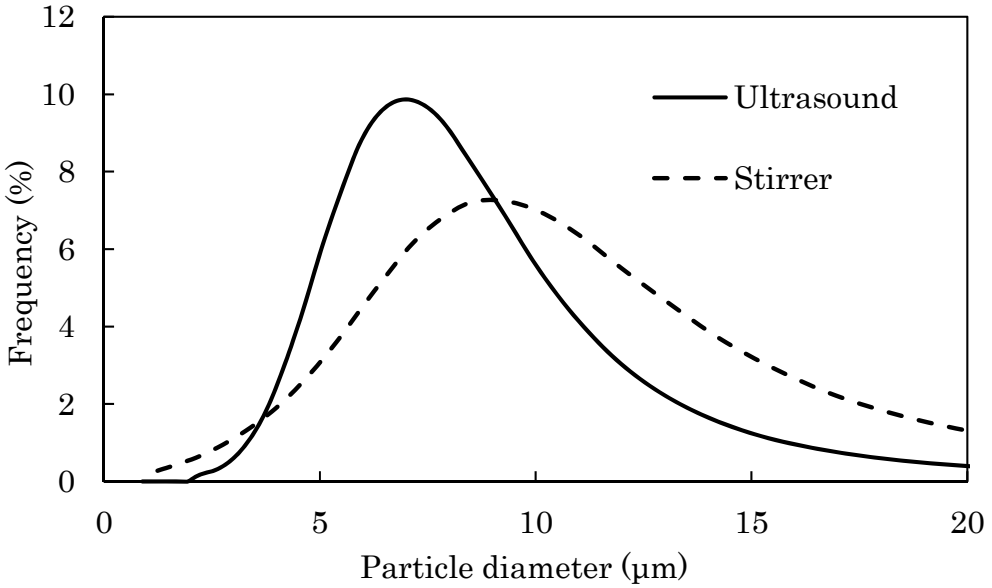

Fig. 5.10 Particle size distributions of the $CaCO_3$ produced at 25 °C when 0.1 mol/l $CaCl_2$ was added to a solution and the solution was treated with ultrasound irradiation or stirred for 5 min.

5.4 Conclusions

We conducted experiments to investigate the desorption of CO_2 from a solution containing a low MEA concentration by applying $CaCl_2$ and either stirring the solution or treating it with ultrasound irradiation. We also characterized the $CaCO_3$ that was generated through the reaction between the CO_2 released and the $CaCl_2$ in the solution during the desorption experiments.

We found that the D_{CO_2} when the solution was treated with ultrasound irradiation was 16.2% and that adding $CaCl_2$ (0.1 mol/l) increased the D_{CO_2} to 40.4%. Similarly, the D_{CO_2} was 10.1% when the solution was stirred, and adding $CaCl_2$ (0.1 mol/l) increased the D_{CO_2} to 39.4%. We concluded that $CaCO_3$ was generated through the reaction between the Ca^{2+} from the $CaCl_2$ and the HCO_3^- produced from the CO_2 desorbed from the MEA. More HCO_3^- was then produced because more CO_2 was released from the MEA, and CO_2 was finally released from the HCO_3^- because the degasification efficiency of the ultrasound irradiation treatment increased the amount of CO_2 that was degasified. It is clear that applying ultrasound irradiation gave higher D_{CO_2} values than did stirring the solution, and adding a low concentration of $CaCl_2$ (0.01 mol/l) increased the D_{CO_2} further. These conclusions were drawn because more CO_2 was associated with the MEA than was used to produce the amount of $CaCO_3$ that was generated by the reaction between the $CaCl_2$ and the CO_2 released from the MEA, meaning that some of the $CaCO_3$ in the solution had been changed into $Ca(HCO_3)_2$. The $Ca(HCO_3)_2$ would have been ionized to form Ca^{2+} and HCO_3^- in the solution, and CO_2 would have degassed from the HCO_3^- because of the degasification efficiency of the ultrasound irradiation treatment.

We characterized the $CaCO_3$ that was generated through the reaction between CO_2 and $CaCl_2$ when a solution was treated with ultrasound irradiation and when a solution was stirred. From XRD patterns, SEM images, and the results of grain size distribution analysis, we concluded that calcite was formed when the ultrasound irradiation treatment was used and that calcite and vaterite were formed when a solution was stirred. The $CaCO_3$ produced when a solution was treated with ultrasound irradiation was homogeneous and the particles were fine (5–10 μm). Therefore, the addition of a small amount of $CaCl_2$ and treating the solution with ultrasound irradiation could not only increase the proportion of CO_2 that could be degasified from an MEA solution but could also cause a homogeneous calcite by-product to be produced that we expect to be suitable for desulfurization processes in coal-fired power plants.

Chapter 6

Conclusion

In this paper, I investigated the fundamental study of CO_2 geological storage and a new method of CO_2 recovery in CCS technology. I clarified the effect of CO_2 from oxyfuel combustion process that is one of the Clean Coal Technology (CCT) on a cap rock and CO_2 injection Ill materials existed near an underground aquifer. It was found that the decrease of pH and further dissolution of cap rock Ire reduced due to the reaction between NO_2 and Fe in a formation water even if the concentration of NO_2 contained in oxyfuel combustion CO_2 gas was high level (about 300 ppmv). Moreover, SO_2 contained in oxyfuel combustion CO_2 gas did not remarkable effect on CO_2 resistant cement and promoted to deposit the corrosion film by enhancing the corrosion of casing steel. I investigated the application of ultrasound for a new method of effective CO_2 desorption from chemical absorbent. It was cleared that the effective CO_2 desorption from low concentration MEA solution could be accomplished in short time with combination of ultrasound irradiation and additional of $CaCl_2$. Below, I will provide the summary of conclusions of chapter 2-5. I hope to contribute a basic database construction of the geological evaluation for injection CO_2 exhausted from coal-fired power plant in the future by clarifying the reaction behavior of CO_2 gas from oxyfuel combustion process in an underground aquifer in this paper. Also, I hope to improve the energy-saving technology for CO_2 recovery in air-combustion process by studying the utilization of ultrasound as one new efficient method for CO_2 recovery in this paper.

In Chapter 2,

a laboratory geochemical study was conducted using a drill core sample of cap rock from the Surat Basin, Australia, to investigate the effect of NO_2 contained in the CO_2 gas exhausted from the oxyfuel combustion process (oxyfuel combustion CO_2) on the cap rock. A gas (CO_2 containing NO_2) was prepared to simulate the exhaust gas produced from the oxyfuel combustion process. Two types of gases (pure CO_2 and CO_2 containing SO_2) were also prepared as reference gases. The effect of NO_2 on cap rock was studied experimentally using these gases. No differences in the amounts of leached ions and pH changes for CO_2 containing NO_2 (36 ppmv), pure CO_2, and CO_2 containing SO_2 (35 ppmv) existed. The pH values decreased immediately after CO_2 gas injection but increased with time as a result of mineral buffering. Leaching of Fe, Mg, Ca, and K was suggested to have occurred as the result of dissolution of Fe-chlorite, prehnite and illite-smectite mixed layer in the shale sample. The amounts of Ca, Fe, and Mg leached with CO_2 containing NO_2 (318 ppmv) were higher than those for pure CO_2. For the mixture containing 318 ppmv NO_2, the pH increased more than that for the other gas conditions immediately after the pH fall at the start of the experiment, because oxidation-reduction reactions occurred between Fe^{2+} and

NO_3^-. Moreover, the results indicated that some of the leached Ca and Fe were deposited on the shale sample because of the pH increase. Therefore, we concluded that the effects of NO_2 on mineral dissolution and pH changes of formation water are negligible when oxyfuel combustion CO_2 containing about 30 ppmv of NO_2 is injected into an underground aquifer. In addition, even if about 300 ppmv NO_2 is accidentally injected into the underground aquifer, mineral dissolution is suppressed due to the rapid pH increase after gas injection.

In Chapter 3,

the effect of a small amount of SO_2 contained in exhaust CO_2 from the oxyfuel combustion process on CO_2 injection materials was investigated when supercritical CO_2 was injected into an underground aquifer. CO_2-resistant cement and casing steel were used as the CO_2 injection well materials in this study and general Portland cement was used to assese the results of the reaction. This experiment was conducted with three types of gases and Na-HCO_3-Cl solution as the formation water at 8.5 MPa and 60 °C in a vessel to simuate the geochemical reaction in the CO_2 injection reservoir. The change in composition of the samples after the experiment was determined by X-ray diffraction and SEM analysis. In the area under 2 mm depth from the surface of the Portland cement, calcium carbonate was generated under CO_2 containing SO_2 and pure CO_2 gas conditions. On the other hand, the changed area of CO_2-resistant cement due to calcium carbonation was narrow. There was no remarkable difference in the change of solution pH and carbonation between CO_2 containing SO_2 and pure CO_2 gas conditions in CO_2-resistant cement and thus we suggest the effect of SO_2 contained in oxyfuel combustion CO_2 on the CO_2-resistant cement could be ignored. In the experiment using casing steel, the dissolution of Fe^{2+} was promoted, increasing the concentration of Fe^{2+} in the solution, but siderite precipitated on the surface under the CO_2 containing SO_2 gas condition.

In Chapter 4,

we investigated the use of ultrasound irradiation to remove CO_2 gas from aqueous solutions of monoethanolamine (MEA). Desorption rates of CO_2 were measured while MEA solutions were exposed to 28 kHz ultrasound irradiation at 25°C. The results showed that the CO_2 desorption rate from low-concentration MEA (0.2 mol/l) is significantly enhanced by ultrasound irradiation as compared with desorption by stirring at low temperature (25°C). It was also found that decreasing the concentration of MEA solutions increased the rate of CO_2 desorption. In addition, we considered the process of desorption of CO_2 from MEA solutions according to experimental results.

In Chapter 5,

we developed an effective method for desorbing CO_2 from low-concentration (0.2 mol/l) monoethanolamine (MEA) solutions using calcium chloride ($CaCl_2$) and ultrasound irradiation at 25 °C. The proportion of CO_2 desorbed from the MEA solution was calculated from the amount of $CaCO_3$ generated and the amount of CO_2 emitted. The proportion of CO_2 desorbed from the MEA solution was much higher when $CaCl_2$ was added than when $CaCl_2$ was not added. We also characterized the $CaCO_3$ that was generated when the solution was treated with ultrasound irradiation and when the solution was stirred. The $CaCO_3$ particles produced were more homogeneous and smaller when ultrasound irradiation was applied than when the solution was stirred.

References

1) International Energy Agency, '*World Energy Outlook 2015*' Chap. 7 (2015).
2) International Energy Agency, '*Coal Information 2015*' Part IV and V (2015).
3) World Coal Association, '*Coal – Energy for Sustainable Development*' (2012).
4) Agency for Natural Resources and Energy, Strategic Energy Plan in Japan, (2014).
5) International Energy Agency, '*Energy Technology Perspectives 2014'* Chap. 2 (2014).
6) The Institute of Energy Economics, Japan, ' *Asia/ World Energy Outlook 2015*' (2015) p.105.
7) Global CCS Institute, *'The Global Status of CCS'* Chap. 2 and 3 (2014).
8) Y. Tanaka, M. Abe, Y. Sawada, D. Tanase, T. Ito, and T. Kasukawa, Energy Proc. 63 (2014) 6111.
9) T. Wall, Y. Liu, C. Spero, L. Elliott. S. Khare, R. Rathnam, F. Zeenathal, B. Moghtaderi, B. Buhre, C. Sheng, R. Gupta, T. Yamada, K. Makino, and J. Yu, Chem. Eng. Research Design 87 (2009) 1003.
10) A. Komaki, T. Goto, T. Uchida, T. Yamada, T. Kiga, and C. Spero, Energy Proc. 63 (2014) 490.
11) S. Azuma, H. Kato, Y. Yamashiata, K. Miyashiro, and S. Saito, Energy Proc. 37 (2013) 5793.
12) C. Spero, T. Yamada, G. Rees, and P. Court, Overview of Commissioning Experience (2013).
13) G. P. Hammond, S. S. O. Akwe, and S. Williams, Energy 36 (2011) 975.
14) M. C. Payan, Bram Verbinnen, B. Galan, A. Coz, C. Vandecasteele, and J. R. Viguri, Environmental Pollution 162 (2012) 29.
15) B. L. Alemu, P. Aagaard, I. A. Munz, and E. Skurtveit, Applied Geochem. 26 (2011) 1975.
16) S. Bachu and T. L. Watson, Energy Proc. 1 (2009) 3531.
17) P. Cao, Z. T. Karpyn, and L. Li, Water Res. Reser. 49 (2013) 1.
18) J. G. J. Olivier, G. J. Maenhout, M. Muntean, and J. A. H. W. Peters, *Trends in Global CO_2 Emissions*, (2013) p. 1.
19) International Energy Agency, *Electricity Information Part 3*, (2014).
20) U. Singh, Current Sci. 105 (2013) 914.
21) C. Chopping and J. P. Kaszuba, Chem. Geology 322-323 (2012) 223.
22) S. Uemura, R. Kataoka, D. Fukabori, S. Tsushima, and S. Hirai, Energy Proc. 4 (2011) 5102.
23) L. Jia, Y. Tan, and E. J. Anthony, Energy and Fuels 24 (2010) 910.
24) H. Liu, S. Katagiri, U. Kaneko, and K. Okazaki, Fuel 79 (2000) 945.
25) H. Liu, S. Katagiri, and K. Okazaki, Energy and Fuels 15 (2001) 403.
26) H. Liu and K. Okazaki, Fuel 82 (2003) 1427.
27) S. Renard, J. Sterpenich, J. Pironon, P. Chiquet, and A. Randi, Chem. Geology 382 (2014) 140.
28) J. K. Pearce, D. M. Kirste, G. K. W. Dawson, S. M. Farquhar, D. Biddle, S. D. Gold, and V. Rudolph, Chem. Geology 399 (2015) 65.
29) Q. Li, X. Li, N. Wei, and Z. Fang, Energy Proc. 4 (2011) 6015.
30) B. R. Ellis, L. E. Crandell, and C. A. Peters, Int. J. Greenhouse Gas Cont. 4 (2010) 575.

31) W. A. Deer, R. A. Howie, and J. Zussman, *The Rock Forming Minerals Second edition*, (1992) p.336.
32) Z. Duan and R. Sun, Chem. Geology 193 (2003) 257.
33) S. Mito, Z. Xue, and T. Ohsumi, Int. J. Greenhouse Gas Cont. 2 (2008) 309.
34) J. Lu, Y. K. Kharaka, J. Thordsen, J. Horita, A. Karamalidis, C. Griffith, J. A. Hakala, G. Ambats, D. R. Cole, T. J. Phelps, M. A. Manning, P. J. Cook, and S. D. Hovorka, Chem. Geology 291 (2012) 269.
35) K. Y. Sung, S. T. Yun, M. E. Park, Y. K. Koh, B. Y. Choi, I. Hutcheon, and K. H. Kim, South Korea. J. Geochem. Exploration 118 (2012) 90.
36) S. Zhang, L. Yang, D. J. DePaolo, and C. I. Steefel, Chem. Geology 396 (2015) 208.
37) F. Brandt, D. Bosbach, E. Krawczyk-Bärsch, T. Arnold, and G. Bernhard, Geochimica et Cosmochimica Acta 67 (2003) 1451.
38) J. R. Black and R. R. Haese, Geochimica et Cosmochimica Acta 125 (2014) 225.
39) I. Bibi, B. Singh, and E. Silvester, Geochimica et Cosmochimica Acta 75 (2011) 3237.
40) A. L. Reesman, Clays and Clay Minerals 22 (1974) 443.
41) J. K. Pearce, A. C. K. Law, G. K. W. Dawson, and S. D. Golding, Chem. Geology 411 (2015) 112.
42) E. B. Ray, and L. T. George, *CRC Handbook of tables for Applied Engineering Science*, (1973) p. 343.
43) Environmental Protection Agency, *Ecological Soil Screening Level for Iron*, (2003).
44) B. Zerai, B. Z. Saylor, and G. Matisoff, Ohio. Appl. Geochem. 21 (2006) 223.
45) S. M. Amin, D. J. Weiss, and M. J. Blunt, Chem. Geology 367 (2014) 39.
46) H. Zheng, X. T. Feng, and P. Z. Pan, Int. J. Greenhouse Gas Control 37 (2015) 451.
47) I. J. Duncan, J. P. Nicot, and J. W. Choi, GCCC Digital Publication Series #08-03i (2008).
48) N. G. Medimurec, and B. Pasic, Rud. Geol. Naft. Zb, 23 (2011).
49) M. Kunieda, D. Tanaka, Y. Yamada, S. Murata, A. Ueda, T. Matsuoka, and N. Yamada, Butsuri-Tanssa, 62 (2009) 447.
50) H. Tamura, J. Chiba, M. Ito, T. Takeda, S. Kikkawa, Y. Mawatari, and M. Tabata, J. Colloid and Interface Sci. 300(2) (2006) 648.
51) N. Setter, K. Scrivener, G. Renaudin, T. Matschei, and P. Bowen, École Polytechnique Federale De Lausanne (2011).
52) T. Morozumi, Bulletin of the Faculty of Engineering, Hokkaido University, 42 (1967) 123.
53) K. Kobayashi, I. Izumi, K. Syuto, and H. Mutsuyoshi, *Zukai Concrete jiten* (2003).
54) A. Raoof, H. M. Nick, T. K. T. Wolterbeek, and C. J. Spiers, Int. J. Greenhouse Gas Cont. 115 (2012) 567.
55) B. Kutchko, B. Strazisar, N. Huerta, and G. Guthrie, Natural CO_2 Sequestration Analogs in

Wellbore Cement Integrity Assessment (2009).
56) Environmental Protection Agency, *Ecological Soil Screening Level for Iron*, (Washington, 2003).
57) A. S. Ruhl, and A. Kranzmann, Energy Proc. 37 (2013) 3131.
58) J. E. Bistline, and V. Rai, Publ. Eng. Policy. 38 (2010) 1177.
59) I. S. Cole, P. Corrigan, S. Sim, and N. Birbilis, Int. J. Greenhouse Gas Control 5 (2011) 749.
60) V. Romerio, and V. Parente, Low Carbon Economy 3 (2012) 130.
61) R. T. Dahowski, C. L. Davidson, X. C. Li, and N. Wei, Int. J. Greenhouse Gas Control 11 (2012) 73.
62) G. P. Hammond, S. S. O. Akwe, and S. Williams, Energy 36 (2011) 975.
63) S. A. Bedell, Energy. Proc. 1 (2009) 771.
64) A. H. Berger, and A. S. Bhown, Energy. Proc. 4 (2011) 562.
65) S. Licht, B. Cui, and B. Wang, J. CO_2 util. 2 (2013) 58.
66) J. R. Li, Y. Ma, M. C. McCarthy, J. Sculley, J. Yu, H. K. Jeong, P. B. Balbuena, and H. C. Zhou, Coodi. Chem.Rev. 255 (2011) 1791.
67) C. H. Yu, C. H. Huang, and C. S. Tan, Aerosol. Air. Qual. Res. 12 (2012) 745.
68) S. Posch, and M. Haider, Chem. Eng. Res. Des. 91 (2013) 977.
69) Y. Chunbo, C. Guangwen, and Y. Quan, Chinese J. Chem. Eng. 20 (2012) 111.
70) Y. E. Kim, J. A. Lim, S. K. Jeong, Y. Yoon, S. T. Bae, and S. C. Nam, Bull. Korean Chem. Soc. 34 (2013) 783.
71) K. Maneeintr, R. O. Idem, P. Tontiwachwuthikul, and A. G. H. Wee, Energy Proc. 1 (2009) 1327.
72) A. Schäffer, K. Brechtel, and G. Scheffknecht, Fuel. 101 (2012) 148.
73) S. Baj, A. Siewniak, A. Chrobok, T. Krawczyk, and A. Sobolewski, J. Chem. Technol. Biotechnol. 88 (2013) 1220.
74) C. Ye, M. Dang, C. Yao, G. Chen, and Q. Yuan, Chem. Eng. J. 225 (2013) 120.
75) H. R. Mortaheb, A. A. Nozaeim, M. Mafi, and B. Mokhtarani, Chem. Eng. Sci. 82 (2012) 44.
76) M. Ghadiri, A. Marjani, and S. Shirazian, Int. J. Greenhouse Gas Control 13 (2013) 1.
77) S. Murai, and Y. Fujioka, IEEJ Trans. 3 (2008) 37.
78) S. Brems, M. Hauptmann, E. Camerotto, A. Pacco, H. Struyf, P. Mertens, C. Gottschalk, and S. D. Gendt, Jpn. J. Appl. Phys. 52 (2013) 066602.
79) N. A. Baena, and D. Eskin, Miner. Met. Mater. Soc. (2013) 957.
80) X. Xu, C. Song, R. Wincek, J. M. Andresen, B. G. Miller, and A. W. Scaroni, Fuel Chem. Division Preprints. 48 (2003) 162.
81) R. Ogawa, T. Kondo, H. Honda, Q. L. Zhao, S. Fukuda, and P. Riesz, Ultrasonics Sonochem. 9 (2002) 197.
82) H. Okawa, T. Saito, R. Hosokawa, T. Nakamura, Y. Kawamura, and K. Sugawara, Jpn. J. Appl. Phys. 49 (2010) 07HE12.

83) H. Okawa, T. Saito, R. Hosokawa, T. Nakamura, Y. Kawamura, and S. Koda, Jpn. J. Appl. Phys. 50 (2011) 07HE12.
84) T. Nakamura, H.Okawa, Y. Kawamura, and K. Sugawara, Jpn. J. Appl. Phys. 50 (2011) 07HE16.
85) T. Nakamura, H. Okawa, R. Hosokawa, T. Saito, Y. Kawamura, and K. Sugawara, Jpn. J. Appl. Phys. 49 (2010) 07HE11.
86) S. Koda, T. Kimura, T. Kondo, and H. Mitome, Ultrasonic Sonochem. 10 (2003) 149.
87) T. Uchida, and T. Kikuchi, Jpn. J. Appl. Phys. 52 (2013) 07HC01.
88) K. V. B. Tran, Y. Asakura, and S. Koda, Jpn. J. Appl. Phys. 52 (2013) 07HE07.
89) C. Honma, D. Kobayashi, H. Matsumoto, and T. Takahashi, Jpn. J. Appl. Phys. 52 (2013) 07HE11.
90) M. Vucak, J. Peric, A. Zmikic, and M. N. Pons, Chem. Eng. J. 87 (2002) 171.
91) J. M. Plaza, D. V. Wagener, and G. T. Rochelle, Int. J. Greenhouse Gas Control 4 (2010) 161.
92) W. J. Choi, J. B. Seo, S. Y. Jang, J. H. Jung, and K. J. Oh, J. Environ. Sci. 21 (2009) 907.
93) H. Selim, A. K. Gupta, and A. A. Shoaibi, Appl. Energy 98 (2012) 53.
94) The Dow Chemical Company, *Ethanolamines* (Midland, Michigan, 2003)
95) J. C. Stephens, Fall, 2 (2006) 4.
96) B. Zhao, Y. Sun, Y. Yuan, J. Gao, S. Wang, Y. Zhuo, and C. Chen, Energy Proc. 4 (2011) 93.
97) M. Mahdavian, H. Atashi, M. Zivdar, and M. Mousavi, Adv. Chem. Eng. Sci. 2 (2012) 50.
98) A. V. Rayer, A. Henni, and P. Tontiwachwuthikul, J. Chem. Eng. 9999 (2011) 1.
99) Y. Zhang, J. Sunarso, S. Liu, and R. Wang, Int. J. Greenhouse Gas Control 12 (2013) 84.
100) H. Z. Aliabad and S. Mirzaei, World Acad. Sci. Eng. Technol. 3 (2009) 1.
101) M. S. Islam, R. Yusoff, and B. S. Ali, Eng. e-Transaction 5 (2010) 97.
102) M. Vucak, J. Peric, A. Zmikic, and M. N. Pons, Chem. Eng. J. 87 (2002) 171.
103) A. Aboudheir, P. Tontiwachwuthikul, A. Chakma, and R. Idem, Chem. Eng. Sci. 58 (2003) 5195.
104) S. W. Park, B. S. Choi, S. S. Kim, and J. W. Lee, J. Ind. Eng. Chem. 13 (2007) 133.
105) B. R. Strazisar, R. R. Anderson, and C. M. White, Fuel Chem. Division Preprints 47 (2002) 55.
106) J. Zhang, D. W. Agar, X. Zhang, and F. Geuzebroek, Energy Proc. 4 (2011) 67.
107) Y. Lu, A. Liao, Z. Yun, Y. Liang, and Q. Yao, Asian J. Chem. 26 (2014) 39.
108) A. Adeosun, N. E. Hadri, E. Goetheer, and M. R. M. A. Zahra, Int. J. Eng. Sci. 3 (2013) 12.
109) T. Supap, R. Idem, P. Tontiwachwuthikul, and C. Saiwan, Int. J. Greenhouse. Gas Cont. 3 (2009) 133.
110) K. Tanaka, T. Fujiwara, H. Okawa, T. Kato, and K. Sugawara, Jpn. J. Appl. Phys. 53 (2014) 07KE14.
111) Y. Kojima, K. Yoshitake, T. Umegaki, and N. Nishimiya, J. Soc. Inorg. Mater. 19 (2012) 104 [in Japanese].
112) W. Hong, X. Hui-bi, Z. Chu-guang, and Q. Jian-rong, J. Cent. South Univ. Technol. 16 (2009) 0845.

113) K. Yasuda, Y. Takahashi, and Y. Asakura, Jpn. J. Appl. Phys. 53 (2014) 07KE08.
114) H. Harada, Y. Ono, and M. Oda, Jpn. J. Appl. Phys. 53 (2014) 07KE10.
115) A. Jamal, A. Meisen, and C. J. Lim, Chem. Eng. Sci. 61 (2006) 6571.
116) A. Shanableh, Jordan J. Civil Eng. 1 (2007) 109.
117) J. Choi, S. M. Hulseapple, M. H. Conklin, and J. W. Harvey, J. Hydrology 209 (1998) 297.
118) R. M. Wagterveld, H. Miedema, and G. J. Witkamp, Cryst. Growth Des. 12 (2012) 4403.
119) Y. Kojima, K. Yamaguchi, and N. Nishimiya, Ultrasonic Sonochem. 17 (2010) 617.
120) A. Szep, and M. Harja, Sci. Study Res. 7 (2006) 369.

Acknowledgment

I am deeply grateful to Professor Dr. Katsuyasu Sugawara of Akita University for his insightful advices. And I would like to thank Professor Dr. Atsushi Shibayama, Dr. Professor Kenji Murakami, and Dr. Professor Shigeo Hayashi of Akita University for their careful checks of my study and helpful advices for my papers.

I appreciate heartfelt leading that Associate Professor Dr. Hirokazu Okawa of Akita University provides me. In addition, I really thank Professor Dr. Akira Imai and Associate Professor Dr. Ryohei Takahashi of Akita University for their helpful advices and comment for my study.

I thank Cris Spero (CS Energy) of project director, Electric Power Development Co., Ltd. (J-POWER), IHI Co., and Mitsui & Co., Ltd for providing a lot of cooperation for Callide Oxyfuel Project. Carbon Transport and Storage Corporation Pty Ltd (CTSCo) are thanked for providing the core sample.

I am grateful to all staff involved in this work in Akita University, Mr. Yuya Kitamura, Mr. Tatsuo Fujiwara and Mr. Takahiro Osawa.

I deeply thank Dr. Keiichiro Hashimoto and Dr. Takashi Nakamura of Japan Coal Energy Center for helpful comments on this paper.